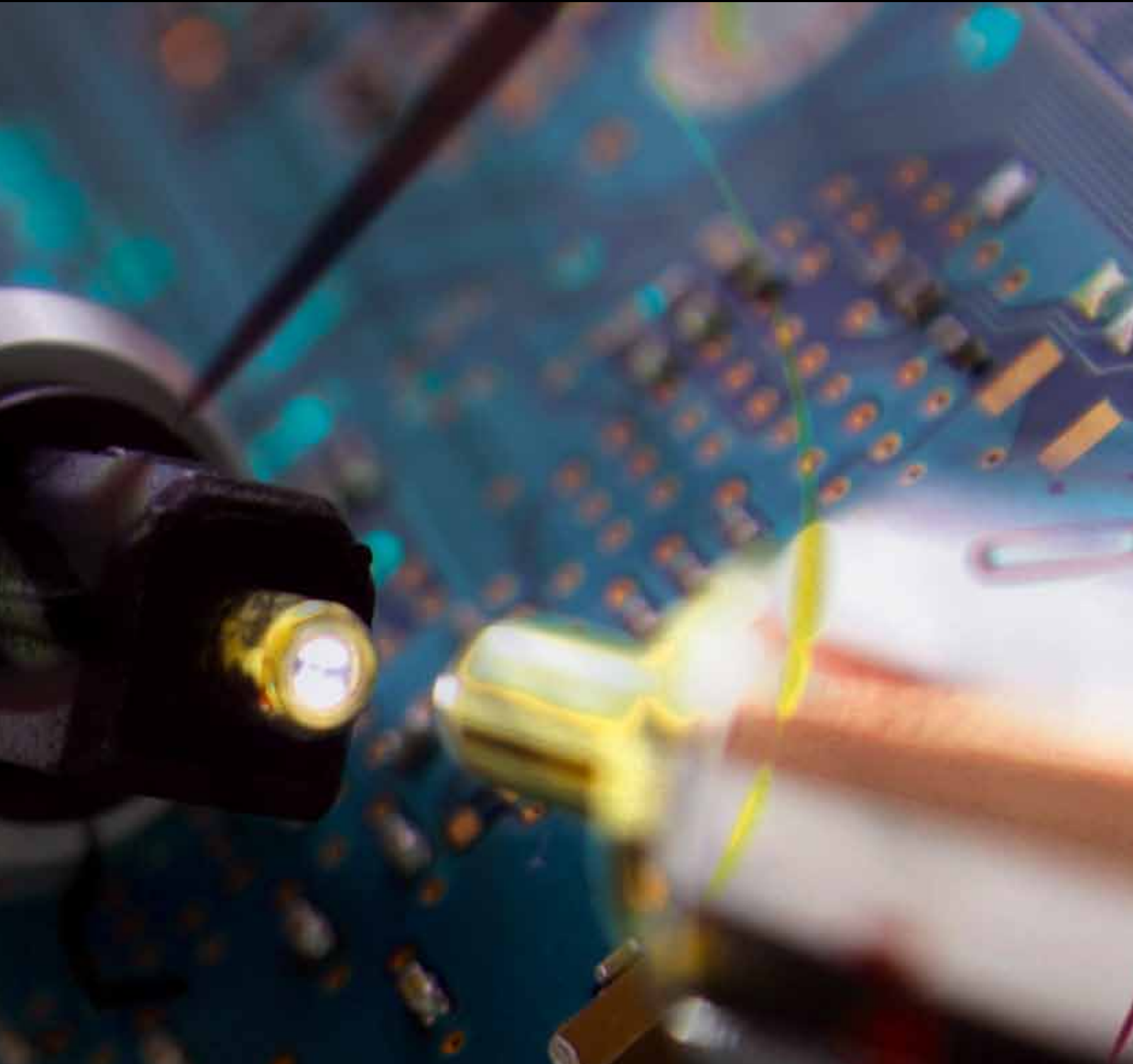


Journal of Sensors

Fiber Optic Sensors

Guest Editors: Wolfgang Ecke, Kevin Chen, and Jinsong Leng





Fiber Optic Sensors

Journal of Sensors

Fiber Optic Sensors

Guest Editors: Wolfgang Ecke, Kevin Chen, and Jinsong Leng



Copyright © 2012 Hindawi Publishing Corporation. All rights reserved.

This is a special issue published in "Journal of Sensors." All articles are open access articles distributed under the Creative Commons Attribution License, which permits unrestricted use, distribution, and reproduction in any medium, provided the original work is properly cited.

Editorial Board

Francisco J. Arregui, Spain
Francesco Baldini, Italy
Benachir Bouchikhi, Morocco
Hubert Braendle, Switzerland
Stefania Campopiano, Italy
Mehmet Can Vuran, USA
Christophe Caucheteur, Belgium
Shoushun Chen, Singapore
Marco Consales, Italy
Jesus Corres, Spain
Geoffrey A. Cranch, USA
Andrea Cusano, Italy
Dzung V. Dao, Japan
Cristina E. Davis, USA
Utkan Demirci, USA
Xinyong Dong, China
Denis Donlagic, Slovenia
Csaba Dücső, Hungary
Isabelle Dufour, France
Luca Francioso, Italy

Laurent Francis, Belgium
Wei Gao, Japan
Tuan Guo, China
Jiri Homola, Czech Republic
Bernhard Jakoby, Austria
Wieslaw Jakubik, Poland
K. Kalantar-Zadeh, Australia
Challa S. S. R. Kumar, USA
Hiroki Kuwano, Japan
Yongxiang Li, China
Yanbiao Liao, China
Kazusuke Maenaka, Japan
Eugenio Martinelli, Italy
Yasuko Y. Maruo, Japan
Ignacio R. Matias, Spain
Mike McShane, USA
Igor L. Medintz, USA
J. R. Morante, Spain
Lucia Mosiello, Italy
Masayuki Nakamura, Japan
K. S. Narayan, India

Masahiro Ohka, Japan
Matteo Pardo, Italy
Michele Penza, Italy
Christos Riziotis, Greece
Giorgio Sberveglieri, Italy
Mikhail G. Shlyagin, Mexico
P. Siciliano, Italy
Mana Sriyudthsak, Thailand
David Stoppa, Italy
Weilian Su, USA
Hidekuni Takao, Japan
Isao Takayanagi, Japan
Maria Tenje, Sweden
Athanasios V. Vasilakos, Greece
Alexander Vergara, USA
Stanley E. Woodard, USA
Hai Xiao, USA
Guangzhong Xie, China

Contents

Fiber Optic Sensors, Wolfgang Ecke, Kevin Chen, and Jinsong Leng
Volume 2012, Article ID 735982, 1 page

Development of Miniaturized Fiber-Optic Laser Doppler Velocimetry Sensor for Measuring Local Blood Velocity: Measurement of Whole Blood Velocity in Model Blood Vessel Using a Fiber-Optic Sensor with a Convex Lens-Like Tip, Tsutomu Tajikawa, Wataru Ishihara, Shimpei Kohri, and Kenkichi Ohba
Volume 2012, Article ID 426476, 11 pages

All-Fiber DBR-Based Sensor Interrogation System for Measuring Acoustic Waves, Maria Iulia Comanici, Lv Zhang, Lawrence R. Chen, Xijia Gu, Lutang Wang, and Peter Kung
Volume 2012, Article ID 862078, 7 pages

Photonic Crystal Fibers for Sensing Applications, Ana M. R. Pinto and Manuel Lopez-Amo
Volume 2012, Article ID 598178, 21 pages

Plastic Optical Fibre Sensing of Fuel Leakage in Soil, Masayuki Morisawa and Shinzo Muto
Volume 2012, Article ID 247851, 6 pages

Plastic Optical Fiber Sensing of Alcohol Concentration in Liquors, Masayuki Morisawa and Shinzo Muto
Volume 2012, Article ID 709849, 5 pages

Editorial

Fiber Optic Sensors

Wolfgang Ecke,¹ Kevin Chen,² and Jinsong Leng³

¹ *Department of Fiber Optics, Institute of Photonic Technology, 07745 Jena, Germany*

² *Department of Electrical and Computer Engineering, Swanson School of Engineering, Pittsburgh University, Pittsburgh, PA 15261, USA*

³ *Center of Composite Materials and Structures, Harbin Institute of Technology, Harbin 150080, China*

Correspondence should be addressed to Wolfgang Ecke, ecke@ipht-jena.de

Received 12 June 2012; Accepted 12 June 2012

Copyright © 2012 Wolfgang Ecke et al. This is an open access article distributed under the Creative Commons Attribution License, which permits unrestricted use, distribution, and reproduction in any medium, provided the original work is properly cited.

Optical fiber sensors find increasing applications in areas ranging from structural health monitoring to biophotonic sensing. The unique properties of optical fibers and sensor structures support such progress: complete immunity to electromagnetic fields, high voltage, lightning; operation in explosive or chemically aggressive and corrosive media (energy, oil, gas); light weight, miniaturized, flexible; low thermal conductivity, temperature-resistant material (high-end and low-end temperatures); low-loss, noninterfering signal transmission, ability to operate over long distances (remote sensing), multiplexing capability (sensor networks), and structure monitoring by embedding in composite materials (smart structures).

New optical wave-guide materials and systems like plastic optical fibers, sapphire optical fiber, photonic crystal fibers, and other nanostructures stimulate corresponding new sensor developments making use of the specific material advantages.

In this issue you will find some examples of actual research, scientific technological development, and application of optical fiber sensors: a review on the status of photonic crystal fibers for sensing applications; fiber Bragg grating resonator structures resulting in an all-fiber DBR-based sensor interrogation system for measuring acoustic waves; the application of plastic optical fibers for sensing of fuel leakage in soil as well as of alcohol concentration in liquors; application of laser Doppler velocimetry for measurement of local blood velocity profiles.

*Wolfgang Ecke
Kevin Chen
Jinsong Leng*

Research Article

Development of Miniaturized Fiber-Optic Laser Doppler Velocimetry Sensor for Measuring Local Blood Velocity: Measurement of Whole Blood Velocity in Model Blood Vessel Using a Fiber-Optic Sensor with a Convex Lens-Like Tip

Tsutomu Tajikawa,¹ Wataru Ishihara,² Shimpei Kohri,³ and Kenkichi Ohba¹

¹ Department of Mechanical Engineering, Kansai University, Osaka 564-8680, Japan

² Boston Scientific, Tokyo 160-0023, Japan

³ Department of Medical Engineering, Aino University Osaka 564-8680, Japan

Correspondence should be addressed to Tsutomu Tajikawa, tajikawa@kansai-u.ac.jp

Received 2 December 2011; Accepted 13 April 2012

Academic Editor: Jinsong Leng

Copyright © 2012 Tsutomu Tajikawa et al. This is an open access article distributed under the Creative Commons Attribution License, which permits unrestricted use, distribution, and reproduction in any medium, provided the original work is properly cited.

A miniaturized fiber-optic laser Doppler velocimetry sensor has been developed to measure the local blood velocity *in vivo*. The laser beam emitted from the sensor tip can be focused at any distance between 0.1 and 0.5 mm from the tip. Consequently, the sensor has a sufficiently high signal-to-noise ratio to measure the local velocity in almost any opaque fluid, including blood. The sensor head is inserted in an injection needle or a catheter tube. In the former case, it is inserted at an angle to the wall of a vessel and is scanned across the vessel to measure the velocity distribution. In the latter case, it is aligned parallel with the flow in a vessel. For all flows of whole human blood, whole caprine blood, and 69% hematocrit of bovine blood, the velocity distribution across the vessel could be measured very accurately. The insertion angle of the fiber into the flow significantly affects the measurement accuracy; an angle of about 50° is suitable when an injection needle is used. When a catheter is employed, an insertion direction opposite to the flow direction is better than parallel to the flow due to the generation of a wake behind the fiber.

1. Introduction

Tanaka and Benedek [1] first developed a fiber-optic laser Doppler velocimetry (LDV) sensor. Kajiya et al. improved it and used it to measure the local blood flow velocity in animal testing [2]. However, the fiber tip transmitted and received light inefficiently, and a dead flow region was observed in front of the fiber tip. Furthermore, it was difficult to observe the dominant frequency in the spectrum of the signal as a function of the Doppler frequency shift. Consequently, this technique has yet to be applied in diagnosis devices.

One of the authors has developed several fiber-optic LDV probes including a probe with an optical dual-fiber pickup that separates the transmission and receiving optical components by using two optical fibers placed alongside each other [3] and a probe with a truncated cone-shaped

distributed index lens (diameter: 1 mm) [4, 5]. However, the flow field is disturbed when the sensor head is directly inserted into the working fluid and the signal-to-noise ratio of the Doppler signal is low due to strong reflection at the interface between the fiber tip and the distributed index lens. Consequently, it was very difficult to measure the flow velocity accurately. To reduce the flow disturbance caused by the probe and to improve the quality of the Doppler signal obtained by heterodyne interferometry, we have been developing a minimized fiber-optic LDV probe with a convex lens at the fiber tip fabricated by microelectromechanical systems technology [6].

This paper reports the development of a fiber-optic LDV system by using an etched fiber with a convex lens-like tip and evaluates the performance of the system by measuring local blood flow velocity.

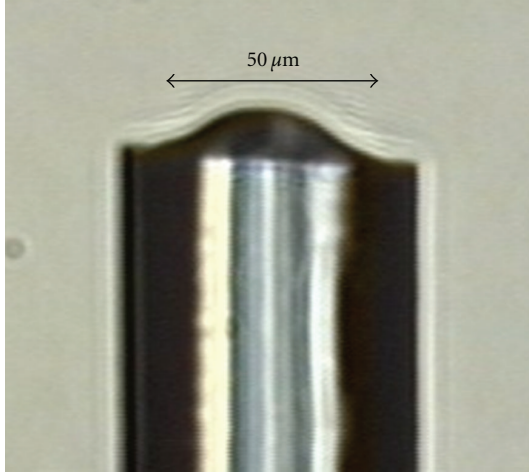


FIGURE 1: Chemically etched quartz fiber probe. (HF : NH₄F : H₂O = 1 : 7 : 5, T = 5.0 h).

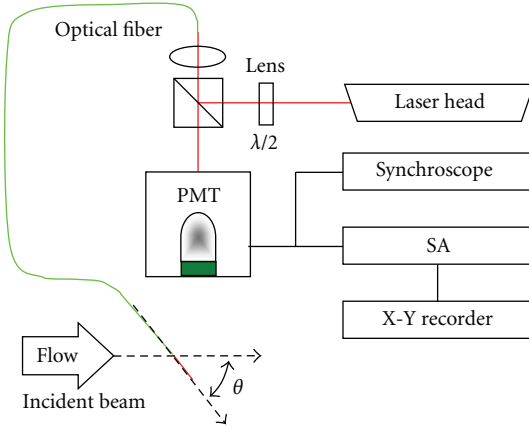


FIGURE 2: Schematic diagram of fiber-optic LDV system.

2. Experimental Setup and Methods

2.1. Fiber-Optic LDV System [6]. Convex lens-like fiber tips were fabricated by chemical etching. Specifically, multimode quartz fibers with a graded refractive index were etched in aqueous solutions of hydrogen fluoride and ammonium fluoride. The solution concentration, etching time, and etching temperature were controlled to obtain the desired radius of curvature for the lens-like surface of the fiber tip (see Figure 1). An optical fiber etched under optimal conditions was used to produce a fiber-optic LDV system for measuring the local blood velocity (see Figure 2).

This system employs a reference beam. A monochromatic beam from a helium-neon laser ($\lambda = 632.8$ nm; power: 25 mW) that is perpendicularly polarized (S polarized) after passing through a half wave plate is reflected by a polarized beam splitter (PBS). The reflected beam is focused by a lens on the tip of the optical fiber (Sumitomo Electric Industries, Ltd., EG-5; core diameter: $50 \mu\text{m}$; cladding diameter: $125 \mu\text{m}$, $NA = 0.21$). The laser beam passes through the optical fiber and is emitted from the convex

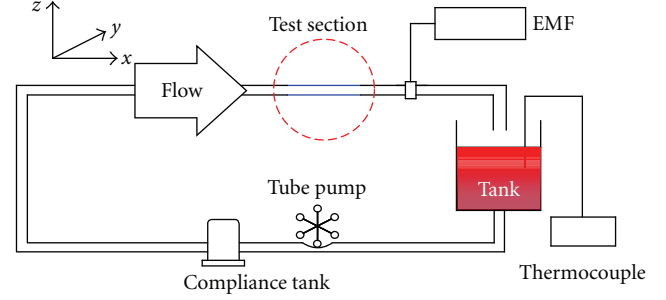


FIGURE 3: Schematic diagram of model flow system.

lens-like fiber end. It converges at the focal point where the measurement volume is formed, because the intensity is maximized at that point. Ray optics calculations based on a microscopy image of the fiber tip surface predict that the laser beam in the optical fiber will converge at a distance of about $L = 220 \mu\text{m}$ from the fiber tip. Therefore, the measurement volume (beam waist, $d_0 : 3.3 \mu\text{m}$; focal depth, $l_0 : 37 \mu\text{m}$) is formed. The light intensity at the focal point is about 160 times higher than that of the incident light on the fiber. When scattering particles, such as, erythrocytes pass through the focal point, they scatter the incident light and shift its frequency by the Doppler effect. Back-scattered light is collected by the same fiber, whereas parallel polarized (P-polarized) light consisting of scattered light and light partially reflected at the fiber end, which functions as a local oscillator, pass through the PBS. Superimposing the scattered and local oscillator light generates heterodyne interference. The light is detected by a photomultiplier tube (PMT; Hamamatsu Photonics K.K., R1477-06). The Doppler signal detected by heterodyne interferometry is processed by a commercial spectrum analyzer (SA) and recorded by an X-Y recorder. The peak in each spectrum is taken to be the Doppler frequency. When a clear peak is not observed in a spectrum, the velocity is either not measured or set to zero. The sensor probe is inserted obliquely into the fluid at an angle θ between the fiber axis and the flow direction. The relationship between the Doppler frequency and the flow velocity is given by

$$u = \frac{f_D \cdot \lambda}{2n \cos \theta}, \quad (1)$$

n is the refractive index of working fluid.

2.2. In-Vitro Circulation Flow Circuit. Figure 3 shows a schematic diagram of the experimental setup for an in-vitro circulation flow circuit. This circuit consists of a closed loop and has a reservoir, a tube pump, a compliance tank for removing flow pulsations, and a silicone rubber tube (inner diameter: 6 mm; outer diameter: 8 mm, length: 1 m) to produce a well-developed flow field. This system was used as a model cardiovascular system. The volumetric flow rate and working fluid temperature were measured by an electromagnetic flowmeter (EMF) and a thermocouple, respectively.

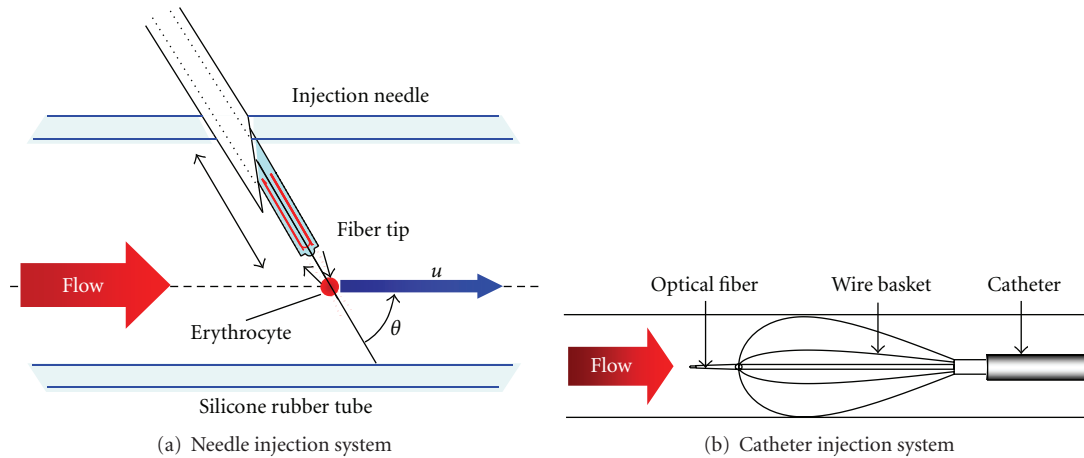


FIGURE 4: Schematic diagram of LDV probe injection system.

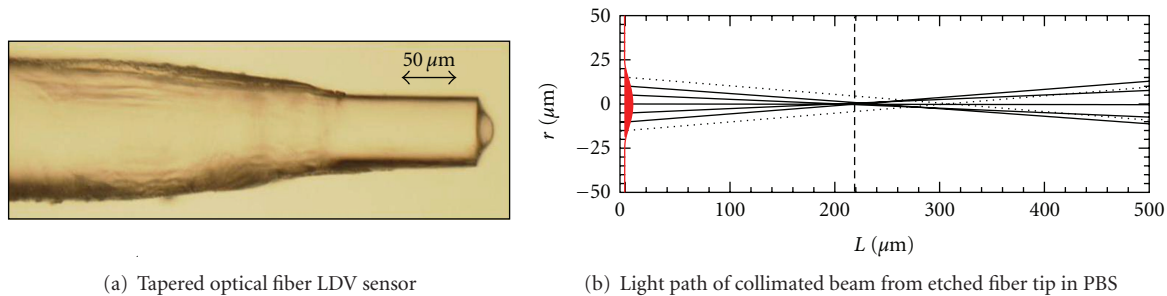


FIGURE 5: Chemically etched quartz fiber tip as LDV sensor.

2.3. Fiber-Optic LDV Probe Insertion Method. Two insertion methods were employed to introduce the fiber-optic LDV probe to the measurement point (see Figure 4).

The first method used an insertion needle with an outer diameter of 0.5 mm. The fiber-optic sensor probe was obliquely inserted into the test section, and it was moved along the needle using a micromotion slide stage to measure the velocity profile in the tube. Prior to the measurement, the Doppler frequency was measured at the center of the tube to evaluate the measurement capability, and the sensor probe was moved along the tube diameter to find a place on the tube wall where there was no clear peak in the spectral waveform. After detecting the sensor position, the velocity distribution in the tube was measured.

A second method to enable the sensor probe to be used in clinical applications, such as, interventional devices. In this method, the fiber-optic sensor was incorporated into a catheter. A catheter for cardiovascular interventional treatment was used to introduce the fiber tip to the measurement point. This catheter (Wilson-Cook Medical Inc., 3.5-Fr; outer diameter: 1.17 mm), which is designed to remove foreign bodies in clinical applications, was inserted either upstream ($\theta = 180^\circ$) or downstream ($\theta = 0^\circ$) of the test section. The fiber tip with a folding Ni-Ti wire frame was pushed down the catheter tube to the measurement point, and the frame was extended to fix the probe at the center of the tube.

3. Experimental Results and Discussion

3.1. Measurement of Velocity Profile in Human Blood Flow.

The flow velocity profiles of whole human blood and a white pigment suspension, which was used as a semiopaque and opaque fluid in previous studies [4–6], were measured in the model blood vessel using the etched fiber probe. An optical fiber with a convex lens-like tip (etched using a volumetric concentration ratio of the buffer solutions with $\text{HF}:\text{NH}_4\text{F}:\text{H}_2\text{O} = 1:7:5$ for 4 h [6]) was used (see Figure 5). A red cell concentrate in a mannitol-adenine-phosphate solution (provided by the Japanese Red Cross Osaka Blood Center) was diluted with phosphate-buffered saline (PBS) to give $H_{ct} = 45\%$, which is the same as that of human whole blood. The insertion angle was set to $\theta = 80^\circ$ and flow rates through the model vessel of 0.2, 0.4, and 0.6 L/min were used. Because blood plasma mostly consists of water (about 93% by volume), plasma is considered to have a similar refractive index to PBS. Therefore, the refractive index of saline was used to estimate the measurement volume. Ray optics calculations using a microscopy image of the fiber tip surface predict that the laser beam from the lens-like fiber tip will converge at a distance of $220\ \mu\text{m}$ from the tip in PBS with a refractive index of 1.333 and for a focal length at a $220\ \mu\text{m}$ [6].

To prevent reductions to the fiber diameter and fiber strength during chemical etching when fabricating the

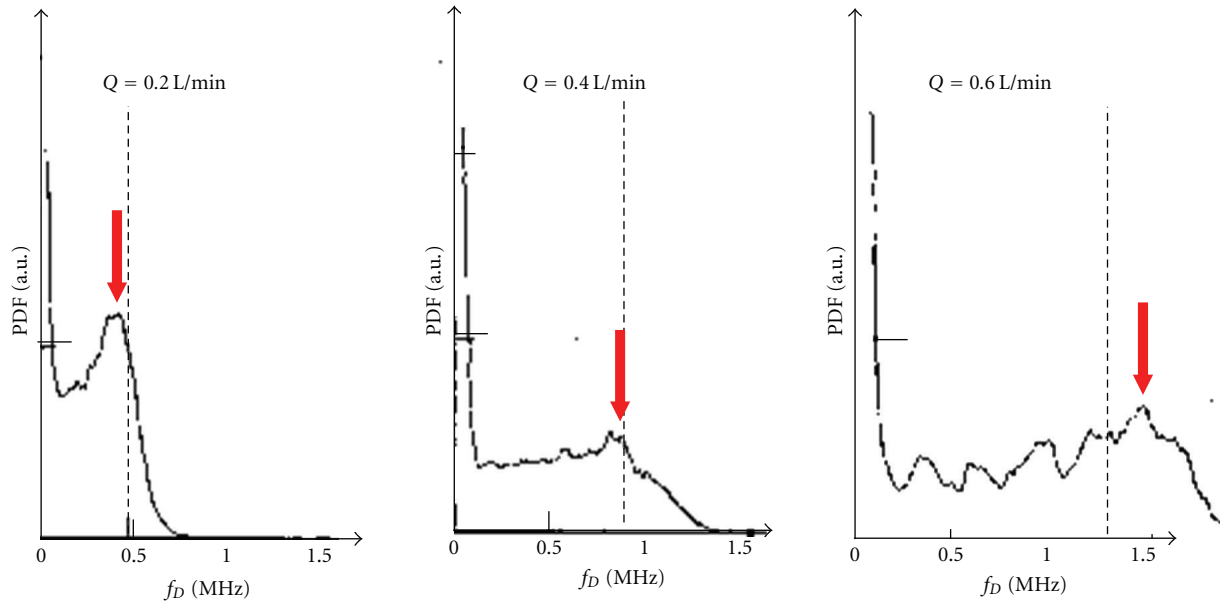


FIGURE 6: PDFs of Doppler signal for various flow rates.

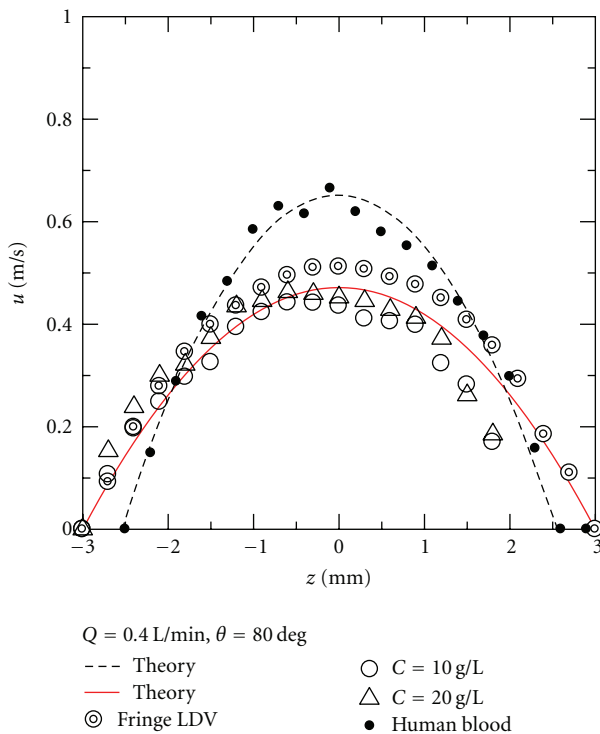


FIGURE 7: Velocity profiles in model blood vessel.

convex lens-like fiber tip, the fiber sidewall was coated with a photoresist (Tokyo Ohka Kogyo Co. Ltd., OFPR800). Figure 6 shows examples of the frequency spectrum of the time-averaged Doppler signal, and Figure 7 shows velocity profiles measured in model vessels at a volumetric flow rate of $Q = 0.4 \text{ L/min}$. The vertical axis in Figure 6 shows the probability density function (PDF) of the time-averaged

Doppler signal while the horizontal axis shows the frequency. The vertical broken lines in Figure 6 indicate the Doppler frequency corresponding to the axial flow velocity, which is calculated from the relationship between the volumetric flow rate and the parabolic velocity profile of laminar Poiseuille flow. The parabolic curves in Figure 7 show the velocity profiles for Poiseuille flow calculated from the volumetric flow rate. The solid and dashed lines are the theoretical velocity profiles in tubes with diameters of 6.0 and 5.1 mm, respectively, and the double circle points indicate the water flow velocity profiles measured using the dual beam mode (fringe-type) LDV system.

These results clearly show that the signal-to-noise ratio of the Doppler signal decreases with increasing volumetric flow rate. This reduction is considered to be caused by a change in the flow pattern as the flow changes from being laminar to being turbulent. Despite this reduction in the signal-to-noise ratio, the dominant frequency corresponding to the Doppler shift was observed as a peak in all the frequency spectra obtained in this experiment.

Because the injection needle used to insert the fiber optic LDV probe locally disturbed the flow field, the local flow velocity at $z = 3 \text{ mm}$ (i.e., on the surface of the upper wall) could not be measured accurately. By assuming Poiseuille flow and a tube diameter of 5.1 mm which is suitable for measuring the velocity profile by this sensor, the measured velocity profile agrees well with the theoretical velocity profile, as indicated by the broken line in Figure 7. Because the model vessel was elliptically deformed by its own weight or by the high pressure drop in the tube caused by high viscous blood flow, the distance that the probe was translated was 0.9 mm shorter than the tube inner diameter. Therefore, the theoretical flow velocity profile was calculated by assuming that the tube diameter was 5.1 mm and that the flow was Poiseuille flow. The measured velocity profile of

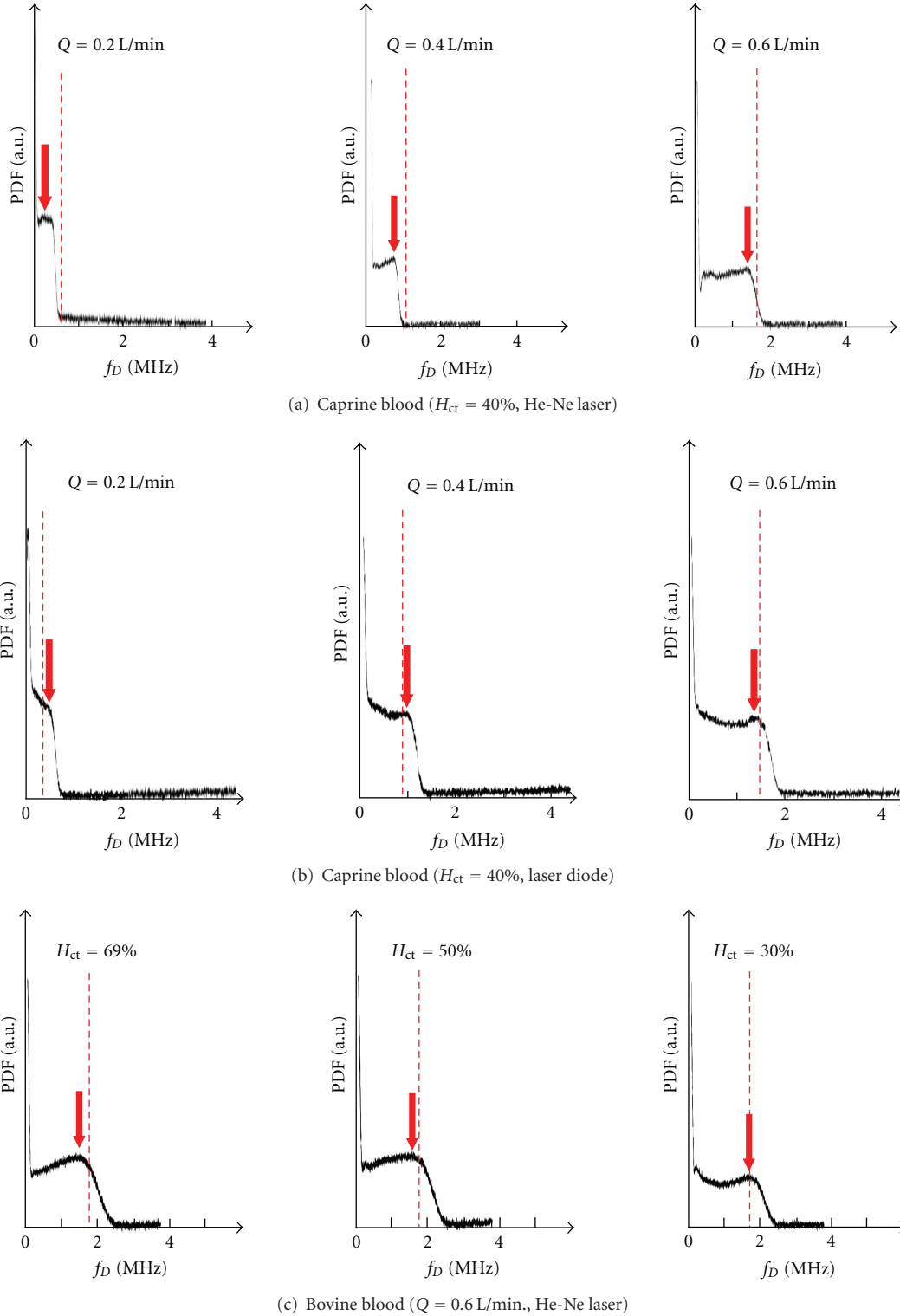


FIGURE 8: PDFs of Doppler signals using needle LDV system.

human whole blood flow was slightly rounded at the center of the tube, but the influence of a partial plug flow was not observed. These results demonstrate that this fiber-optic LDV system is able to accurately measure the local velocity of human whole blood flow.

3.2. Influence of Laser Wavelength and Blood Concentration on Measurement Accuracy. This study used a helium-neon laser as a monochromatic light source for the LDV system. However, light with a wavelength in the range 700–1200 nm can easily penetrate living tissue [7]. In a previous study

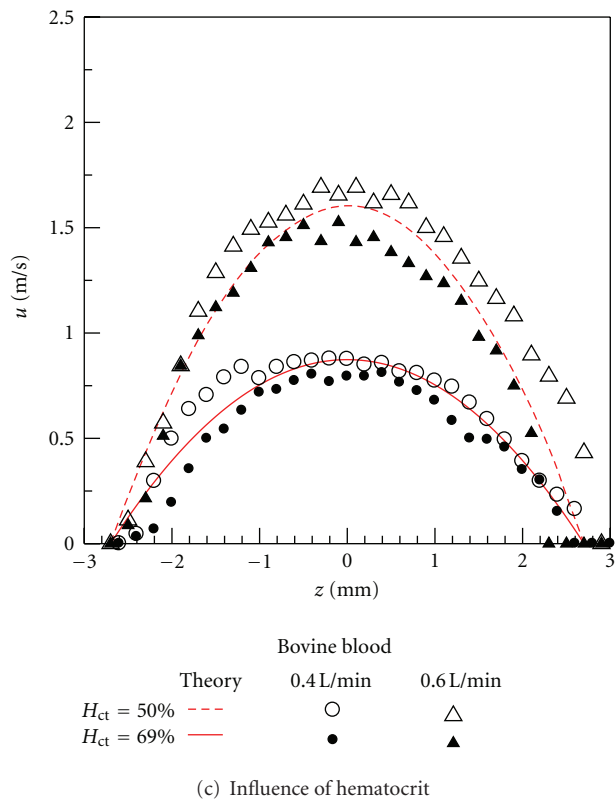
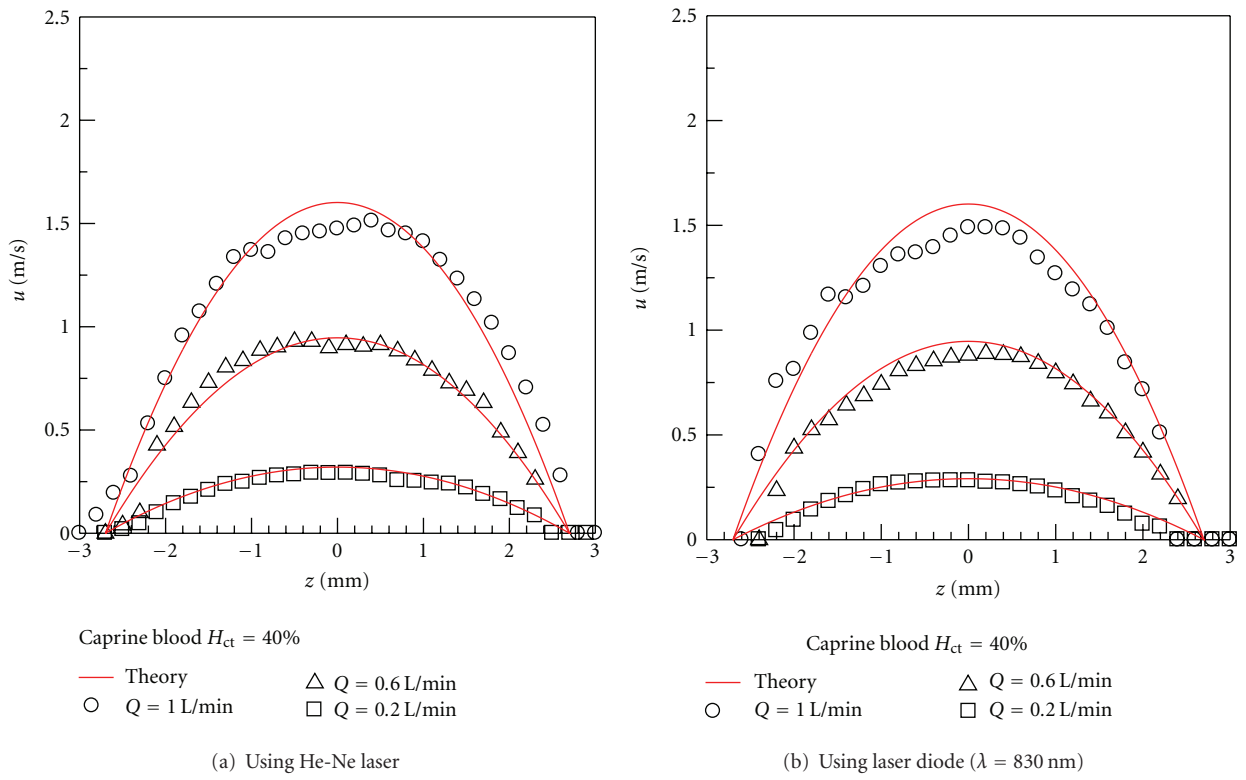


FIGURE 9: Blood flow velocity profiles in model vessel.

in which we measured the optical transmittance of whole bovine blood, we found that light with wavelengths of 830 and 632.8 nm from a normal-cut fiber tip decayed in intensity to 13.5 and 2.5%, respectively, at a distance of $L = 220$ nm from the fiber tip [8]. Because this fiber-optic probe has both transmission and receiving optical components and the light scattered from particles (e.g., red blood cells) is collected by the same fiber-optic probe, the maximum intensities of the light collected by the fiber are expected to be, respectively, 1.8% (LD: $\lambda = 830$ nm) and 0.06% (He-Ne: $\lambda = 632.8$ nm) of the light from the fiber tip. This will affect the results of velocity measurements. Therefore, the effects of the blood concentration and wavelength dependence of the LDV system were studied.

Whole caprine blood consisting of 40% hematocrit and concentrated bovine blood consisting of 69% hematocrit were used in this experiment. A helium-neon laser ($\lambda = 632.8$ nm; power: 25 mW) and a laser diode ($\lambda = 830$ nm; power: 30 mW) were used as light sources for the LDV system. The wavelength dependencies of the half wave plate and the polarized beam splitter in the fiber-optic LDV system were corrected. However, the wavelength dependence of the photomultiplier tube was not corrected.

Figure 8 shows an example of a Doppler frequency spectrum obtained at the center of the test tube. The vertical axis shows the PDF of the time-averaged Doppler signal, while the horizontal axis shows the frequency. The vertical broken lines in each spectrum indicate the Doppler frequency corresponding to the real velocity calculated from the volumetric flow rate under the assumption of Poiseuille flow. The arrows in the graphs indicate the reading frequencies. Figure 9 shows the results of the velocity profile measurements.

These results show that the pedestal noise component in the frequency spectrum was slightly lower for the helium-neon laser than for the laser diode. However, the wavelength difference did not appear to affect the results. This is ascribed to differences between the blood samples and to the helium-neon laser beam being more coherent than the laser diode beam. At both wavelengths, a peak was observed in each spectrum obtained. In addition, this fiber-optic LDV system could measure the flow velocity of high concentrated blood (69% hematocrit). The measured velocity profiles of each blood flow were slightly more rounded in the center of the tube than a parabolic velocity profile. This flow in the center of the tube is known as partial plug flow and is observed in for non-Newtonian flow [9]. The above results demonstrate that this fiber-optic LDV sensor can measure blood flow velocities of blood samples with higher concentrations than whole blood.

3.3. Influence of Insertion Angle on Measurement Accuracy. To determine the frequency shift produced the Doppler effect, the flow velocity vector must have a component parallel to the incident laser beam. Therefore, in a previous study [6], we inserted the sensor probe diagonally into the working fluid. However, the effect of the insertion angle on the measurement accuracy of the catheter LDV system has not

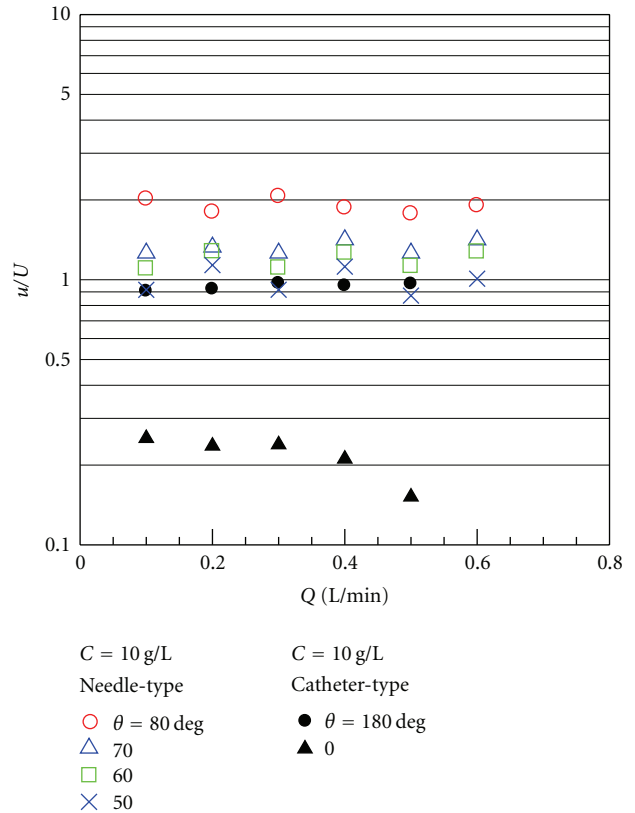


FIGURE 10: Relationship between injection angle and error ratio of measured velocity.

been determined. Therefore, the influence of the insertion angle on the measurement accuracy was investigated in the present study. The axial flow velocity was measured using catheter and needle LDV systems for various insertion angles in a white pigment suspension, which was a model blood.

Figure 10 shows the relationship between the volumetric flow rate and the error ratio (defined as the ratio of the measured velocity in the center of the tube to theoretical velocity obtained from volumetric flow rate) for various insertion angles when the white pigment concentration was $C = 10$ g/L. Figure 11 shows examples of spectra obtained of the Doppler signal using the catheter LDV system. The vertical broken lines and the arrows in each spectrum indicate the same parameters as above. When the white pigment concentration was lower than $C = 24$ g/L, a clear peak was observed in spectra obtained using the catheter LDV system when $\theta = 180^\circ$; it was almost same as the theoretical velocity calculated from the flow rate.

In contrast, when the insertion angle was $\theta = 0^\circ$, the frequency peaks in the spectra disappeared when $C = 10$ g/L and the obtained Doppler frequencies were much lower than the estimated frequencies corresponding to axial velocity in the tube. This is considered to be because the measurement point was located in the wake flow generated by the boundary layer flow in the fiber. The measurement accuracy of the needle LDV system was reduced when the insertion angle was close to 90° . This result indicates that the

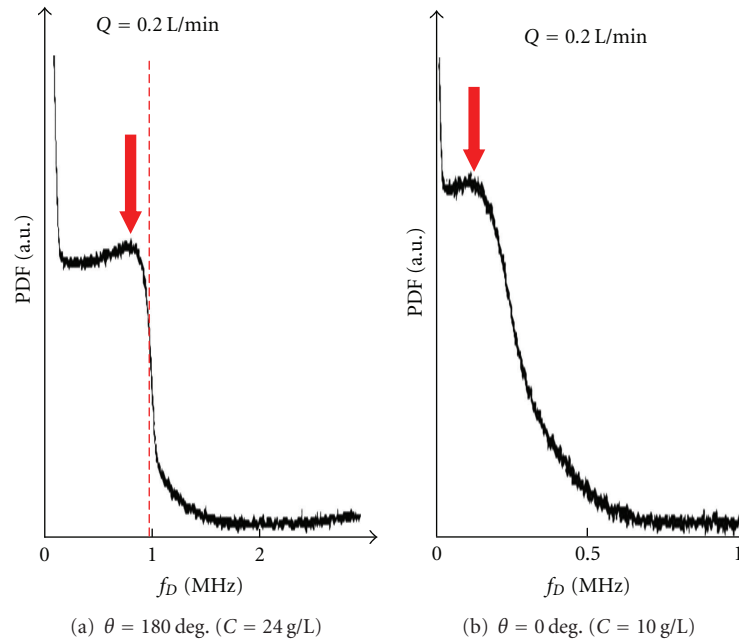


FIGURE 11: PDFs of Doppler signals obtained using catheter LDV.

setting error of the insertion angle affects the frequency-to-velocity conversion using (1). The optimal insertion angles are considered to be $\theta = 50^\circ$ and 180° for the needle and catheter LDV systems, respectively. The catheter LDV system is the preferred insertion method when using this sensor in clinical applications. We next performed blood flow measurements using the catheter LDV sensor.

3.4. Measurement of Blood Flow Velocity by Catheter LDV System. The sensor tip of the catheter LDV system was aligned upstream, and working fluids of bovine whole blood and caprine blood ($H_{ct} = 40\%$) were used. In this experiment, the bovine blood concentration was varied between 30 and 69% by adding PBS. The working fluid was pumped through the circuit (see Figure 3). A helium-neon laser and a laser diode were used as the oscillators in this experiment.

Figure 12 shows examples of frequency spectra obtained in blood flow measurements using the catheter LDV system. No clear peak of the Doppler frequency corresponding to the flow velocity was observed in any of the spectra. In addition, the signal-to-noise ratio was significantly lower than for the needle LDV system; the peak becomes broader with increasing blood concentration. This result indicates that multiple scattering occurred between the fiber tip and the focal point of the fiber. Thus, we modified the definition of the measurement frequency: the Doppler frequency was taken to be the frequency at which the spectral profile increased steeply. The measurement frequencies are indicated by arrows with dotted lines in Figure 12. Figures 13 and 14 show the results of converting this frequency to velocity using (1). Figure 13 shows the effect of using different light sources and the error ratio of the measurement velocity

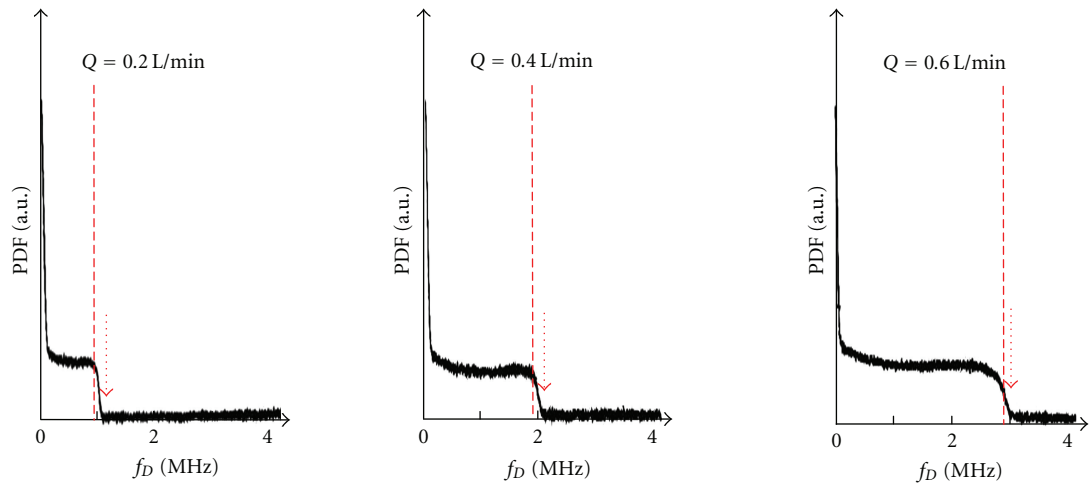
for the catheter LDV system, while Figure 14 shows the relationship between hematocrit of bovine blood and the error ratio for velocities measured using a catheter LDV system.

Most velocities measured in this experiment were within several percent of the theoretical values along the tube axis. However, the measured velocities for caprine blood flow (40% hematocrit) using the laser diode were about 3–15% lower than the theoretical values along the tube axis. Since the pedestal noise component in each spectrum is higher for the laser diode than for the helium-neon laser, this result suggests that the coherence of the laser light affects the signal intensity. It indicates that light coherence is an important factor when measuring blood flow velocity using light transmission. Consequently, the measurement accuracy was higher for the helium-neon laser than for the laser diode.

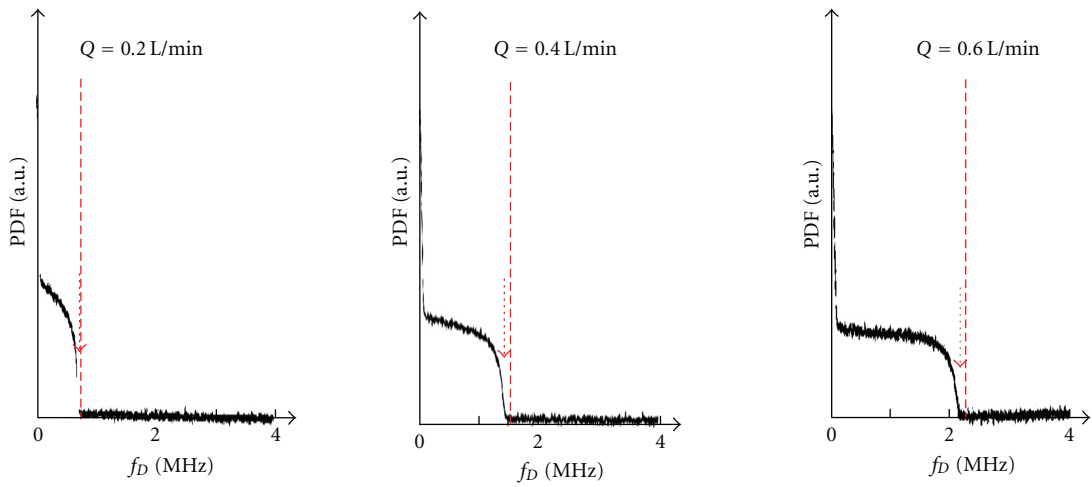
4. Conclusions

A fiber-optic laser Doppler velocimeter system was developed using a chemically etched optical fiber with a convex lens-like tip as the light transmitting and receiving probe. The fiber-optic LDV system was used to measure the local flow velocity in opaque and semiopaque fluids, including a white pigment suspension, whole human blood, whole bovine blood, and whole caprine blood. The performance of this system was evaluated and the following results were obtained.

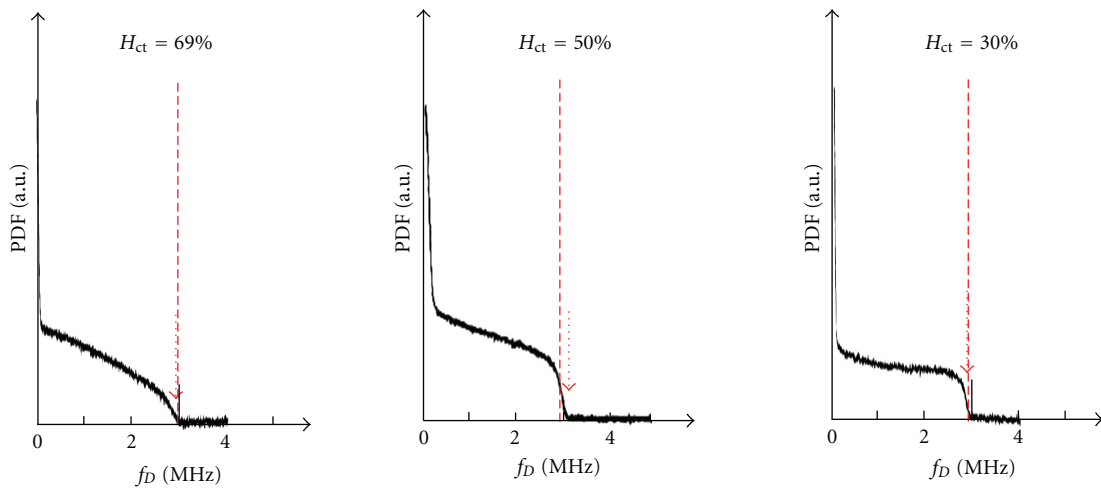
- (1) The velocity distribution across the vessel could be very accurately measured for flows of whole human blood, whole caprine blood, and concentrated bovine blood (hematocrit 69%).
- (2) The light source (a He-Ne laser and a laser diode) had little effect on the measurement accuracy.



(a) Caprine blood ($H_{ct} = 40\%$), He-Ne laser



(b) Caprine blood ($H_{ct} = 40\%$), laser diode



(c) Bovine blood, $Q = 0.6$ L/min., He-Ne laser

FIGURE 12: PDFs of Doppler signal using catheter LDV system.

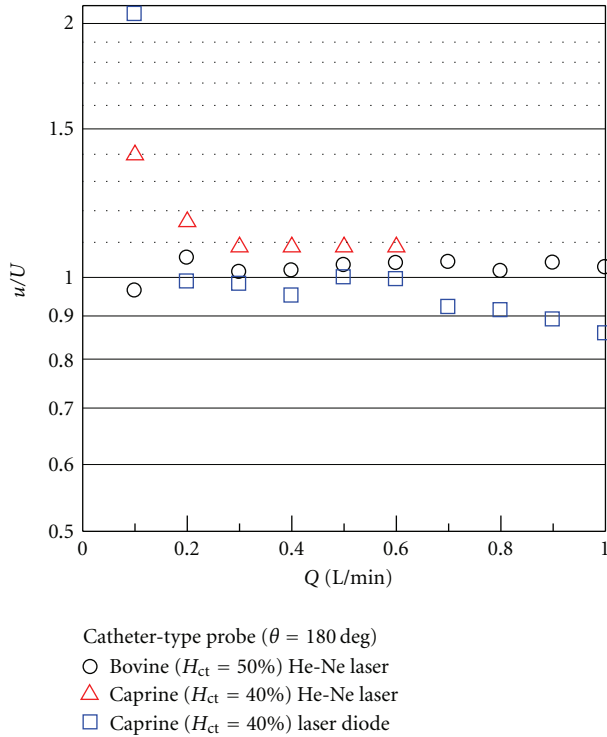


FIGURE 13: Effect of different light sources and error ratio of measured velocity for catheter LDV system.

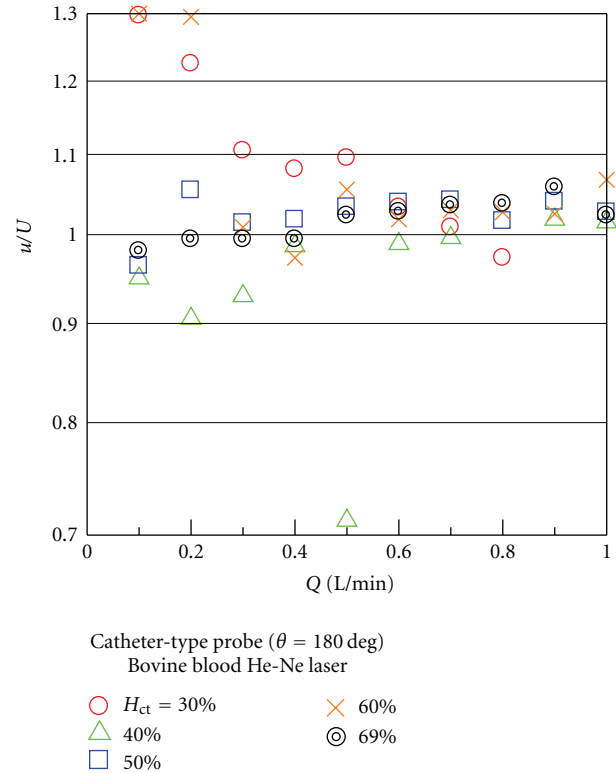


FIGURE 14: Relationship between hematocrit of bovine blood and error ratio of measured velocities using catheter LDV system.

- (3) The insertion angle of the fiber into the flow significantly affects the measurement accuracy; an insertion angle of about 50° is optimal for the injection needle LDV system.
- (4) For the catheter LDV system, an insertion direction against the flow is better than one with the flow due to the effect of the wake behind the fiber tip.

Nomenclature

- T : Etching time (h)
- r : Radial position relative to fiber axis (μm)
- L : Distance from fiber tip (μm)
- z : Distance from center of the tube to upper vertical (mm)
- Q : Volumetric flow rate (L/min)
- u : Local flow velocity (m/s)
- U : Axial flow velocity calculated from volumetric flow rate (m/s)
- C : Mass concentration of white pigment suspension (g/L)
- H_{ct} : Hematocrit (volumetric concentration of erythrocyte in blood) (%)
- f_D : Doppler shift frequency (MHz)
- θ : Fiber insertion angle relative to flow direction ($^\circ$)
- λ : Laser wavelength (nm).

Acknowledgments

A part of this study was supported by the Ministry of Education, Culture, Sport, Science and Technology (MEXT), Japan, through the “Academic Frontier” Project at Kansai University on “Creation of Realistic Models of Human Tissues, Organs using Nano/Sub-micro Technology and their Development to Artificial Tissues/Organs”, 2003–2007. The authors express their appreciation to the Japanese Red Cross Osaka Blood Center and the Department of Artificial Organs of the National Cardiovascular Center for providing blood samples.

References

- [1] T. Tanaka and G. B. Benedek, “Measurement of the velocity of blood flow (in vivo) using a fiber optic catheter and optical mixing spectroscopy,” *Applied Optics*, vol. 14, no. 1, pp. 189–196, 1975.
- [2] F. Kajiyama, N. Hoki, G. Tomonaga, and H. Nishihara, “A laser-Doppler-velocimeter using an optical fiber and its application to local velocity measurement in the coronary artery,” *Experientia*, vol. 37, no. 11, pp. 1171–1173, 1981.
- [3] K. Ohba and T. Matsuno, “Local velocity measurement of opaque fluid flow using laser Doppler velocimeter with optical dual fiber pickup,” *Transactions of the Japan Society of Mechanical Engineers, Series B*, vol. 49, no. 447, pp. 2380–2389, 1983.
- [4] K. Ohba and N. Fujiwara, “Development of fiber optic laser Doppler velocimeter for measurement of local blood velocity,”

- in *Proceedings of the 5th International Conference on Laser Anemometry*, vol. 2052 of *Proceedings of SPIE*, pp. 195–201, Koningshof, The Netherlands, August 1993.
- [5] K. Ohba and M. Nishiyama, “Development of small fiber optic laser Doppler velocimeter sensor for measurement of local blood velocity,” *Japanese Journal of Medical Electronics and Biological Engineering*, vol. 36, supplement 1, p. 307, 1998 (Japanese).
- [6] T. Tajikawa, M. Takeshige, W. Ishihara, S. Kohri, and K. Ohba, “Development of miniaturized fiber-optic laser Doppler velocimetry sensor for measurement of local blood velocity (fabrication of convex or concave lens-like fiber tip and the characteristics of sensor optical system),” *Journal of Fluid Science and Technology*, vol. 4, no. 1, pp. 62–74, 2009.
- [7] K. Shimizu and K. Yamamoto, “Biomedical imaging by optical computer tomography-Status of basic research and CT Imaging with CW laser,” *BME*, vol. 8, no. 8, pp. 4–13, 1994 (Japanese).
- [8] K. Ohba and T. Matsuno, “Development of fiber optic laser Doppler velocimeter sensor for measurement of local blood velocity,” *Journal of Flow Measurements*, vol. 8, pp. 43–46, 1995 (Japanese).
- [9] Y. C. Fung, *Biomechanics: Mechanical Properties of Living Tissues*, Springer, 1981.

Research Article

All-Fiber DBR-Based Sensor Interrogation System for Measuring Acoustic Waves

Maria Iulia Comanici,¹ Lv Zhang,¹ Lawrence R. Chen,¹ Xijia Gu,² Lutang Wang,³ and Peter Kung³

¹Department of Electrical and Computer Engineering, McGill University, Montreal, QC, Canada H3A 2A7

²Department of Electrical and Computer Engineering, Ryerson University, Toronto, ON, Canada M5B 2K3

³QPS Photonics, Pointe Claire, QC, Canada H9R 5L7

Correspondence should be addressed to Lawrence R. Chen, lawrence.chen@mcgill.ca

Received 2 December 2011; Accepted 17 February 2012

Academic Editor: Wolfgang Ecke

Copyright © 2012 Maria Iulia Comanici et al. This is an open access article distributed under the Creative Commons Attribution License, which permits unrestricted use, distribution, and reproduction in any medium, provided the original work is properly cited.

We investigate the use of all-fiber distributed Bragg reflector (DBR) lasers for fiber optic sensing. We measure the steady-state strain response and show that it is very similar to that for a simple fiber Bragg grating (FBG). The lasers can be wavelength multiplexed and support multisensor operation without crosstalk. We also verify the principle of wavelength-to-power mapping, which can simplify sensor interrogation. Finally, we demonstrate that all-fiber DBR lasers can be used to detect acoustic waves.

1. Introduction

The fiber optic nature of fiber Bragg gratings (FBGs) makes them useful as sensing elements because they are compact, low cost, and immune to electromagnetic interference. Environmental and mechanical factors affect the response of FBGs: in particular, their reflection spectra shift to different wavelengths in response to changes in temperature, applied strain, or pressure [1, 2].

The wavelength-encoded nature of the information associated with FBG sensors associated with FBG sensors allows them to be wavelength multiplexed, that is, WDM configurations. Sensor interrogation and information recovery requires the use of an optical spectrum analyzer (OSA) to measure accurately the changes in wavelength [3]. On the other hand, the ability to map wavelength-encoded information to power measurements can simplify system design and reduce cost; indeed, various implementations of wavelength-to-power mapping for FBG sensors have been demonstrated using interrogation filters such as edge filters and arrayed-waveguide gratings (AWGs) [4–10]. This interrogation method allows using power meters or photodetectors to monitor the detected signal from the sensor.

However, such systems suffer from low power efficiency, that is, the signal reflected by an FBG sensor is typically low in power due to the spectral slicing process, thereby resulting in a limited dynamic range and decreased sensitivity. While it has been shown that the resolution of the wavelength-to-power mapping can be improved with FBGs having narrow bandwidth [10], this exacerbates the problem of power efficiency as even less power is reflected by the sensor.

Recently, we proposed a simple change to improve the overall performance of the conventional FBG-interrogation filter system: we use optical feedback to create a linear cavity laser [11]. With this laser configuration, there is increased output power at the FBG sensor wavelengths due to lasing, which results in a greater dynamic range and higher sensitivity as it is easier to distinguish the lasing peak from the noise floor. Moreover, the bandwidth of the signal reflected by the FBG sensor is reduced (since the lasing linewidth is narrower than the FBG reflection bandwidth), which improves the system resolution. Although the laser system works well for steady-state strain/temperature measurements, crosstalk in the laser gain medium, either a semiconductor optical amplifier or an Erbium-doped fiber amplifier (EDFA), prohibits its use for dynamic measurements [12].

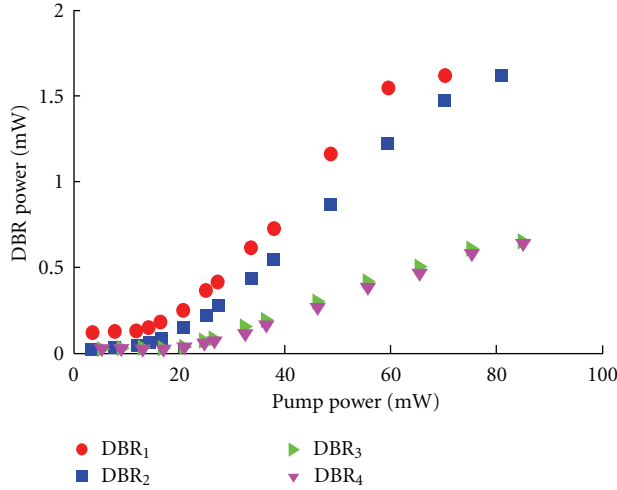


FIGURE 1: Output power from DBR lasers as a function of pump power.

TABLE 1: Threshold pump power for the DBRs used in the experiment.

	Threshold pump power (mW)
DBR ₁	13.13
DBR ₂	15.21
DBR ₃	16.88
DBR ₄	19.49

In this paper, we investigate all-fiber distributed Bragg reflector (DBR) lasers for fiber optic sensing. We show that the lasing wavelengths shift with applied strain with sensitivities similar to conventional FBG sensors. Since the lasers are spatially separate and each has its own gain medium, gain competition and the resulting deleterious effects of crosstalk can be minimized, if not avoided. Finally, we demonstrate that the DBR sensors can be used to detect and locate acoustic waves.

2. Experimental Setup and All-Fiber DBR Sensor Characterization

Each DBR laser used in our experiment comprises two FBGs at the same wavelength (~ 1533 nm) and separated by approximately 8 mm of Er:Yb codoped fiber (with an absorption of 2 dB/cm at 980 nm). The FBGs are written using UV exposure, and the Er:Yb codoped fiber is hydrogen loaded to increase its photosensitive response. One FBG has high reflectivity ($\sim 99\%$) and is broadband, covering several longitudinal modes, while the second FBG has lower reflectivity (but $> 90\%$) and spans only one or two longitudinal modes. Asymmetry in the gain profile typically causes the oscillation of only one longitudinal mode. Figure 1 shows the measured output power versus pump power for the four DBR lasers used; the threshold powers are given in Table 1.

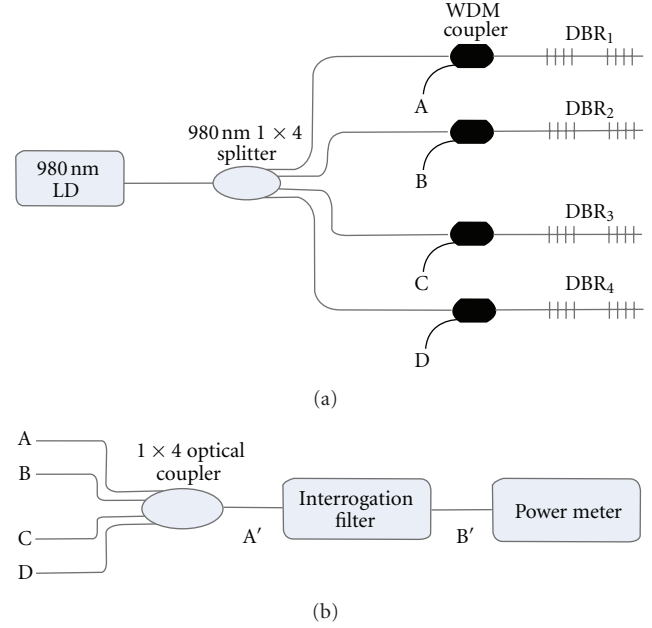


FIGURE 2: (a) Experimental setup of 4 DBR sensor system and (b) demodulation system used to measure the response of each sensor. LD: laser diode.

The experimental setup for a four DBR sensor system is shown in Figure 2. The output from the 980 nm pump laser (maximum output of 360 mW) is distributed equally among 4 branches and launched to the DBR sensors using 980/1550 WDM couplers. The output signals from each DBR sensor are coupled and then an arrayed waveguide grating (AWG) or tunable bandpass filter is used for wavelength-to-power mapping. Figure 3(a) shows the optical spectrum of the combined signals at port A'; nearly equal power is available from the four DBR sensors. Note that since the four DBRs operate nominally at the same wavelength, we placed them on separate translation stages to shift their wavelength for easier identification. Figure 3(b) shows the typical optical spectrum for a single DBR laser (DBR₄); the optical signal to noise ratio is 58 dB.

We first characterize the strain response of each DBR sensor. Figure 4(a) shows the measured wavelength shift as a function of applied strain. We obtain strain sensitivities of 0.85 nm/mstrain, 0.88 nm/mstrain, 0.86 nm/mstrain, and 0.84 nm/mstrain for DBR₁, DBR₂, DBR₃, and DBR₄, respectively. These values are similar to the typical FBG strain sensitivity of 1 nm/mstrain [13]. Next, the DBR signals are coupled and sent to an AWG for wavelength-to-power mapping. The output from each AWG channel is detected using a 125 MHz photodetector followed by a 2 MHz electrical low pass filter. The wavelength of each DBR was tuned over the wavelength span of the corresponding AWG channel and the detected voltage as a function of applied strain was obtained; the result for DBR₄ is illustrated in Figure 4(b). The detected voltage follows the shape of the AWG channel spectral response, thereby verifying successful wavelength-to-power mapping.

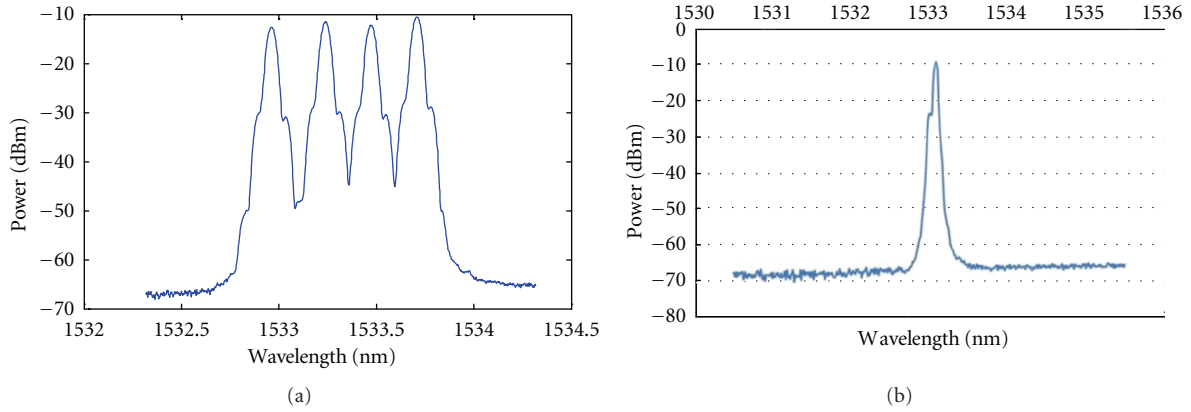


FIGURE 3: (a) Optical spectrum measured at point A' showing equal power from the 4 DBR sensors. (b) Output spectrum from DBR₄.

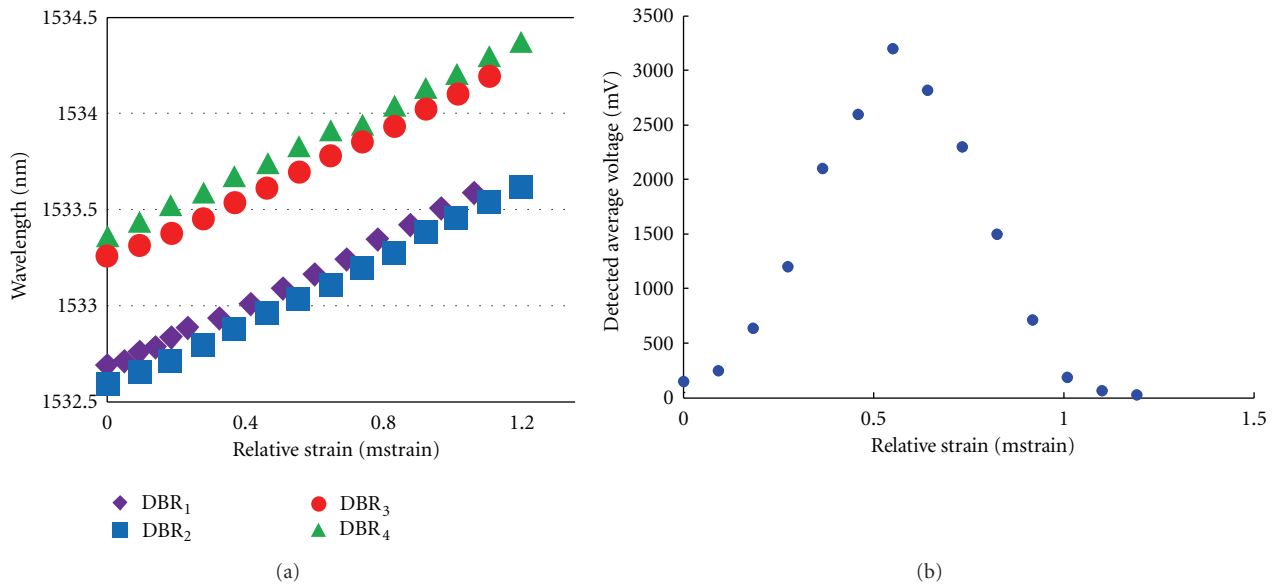


FIGURE 4: (a) Measured strain response for the four DBR sensors and (b) change in detected voltage as a function of applied strain for DBR₄.

3. Detection of Acoustic Waves

Acoustic waves are generated when cracks, deformations, and surface degradations are formed and their detection can be used for structural monitoring [14, 15]. Several groups have investigated the use of all-fiber DBR lasers to detect acoustic waves; these implementations focus on exploiting the polarization dependence of refractive index changes related to acoustic pressure [16, 17]. Acoustic waves are also associated with partial discharges (PDs), which occur in high-voltage systems when the insulation starts to degrade. It is extremely important to be able to detect the presence of PDs as early detection can help prevent critical degradation, which may lead to fires and hazards to neighboring equipment [18–21]. In this paper, we consider a simple approach based on detecting the time-varying changes in output power from a DBR laser that is subject to acoustic waves. Moreover, we show that since the DBR lasers are spatially independent, the effects of gain competition are minimized thereby eliminating crosstalk for multisensor operation.

To assess the capability of the DBR sensor to detect acoustic waves, we use a spark/electric arc discharge generator that produces acoustic waves that accompany the sparks, see Figure 5. The acoustic waves are then transmitted through a plastic or metallic surface/plate onto which the DBR is glued; the plate is located at a distance H above the spark. The principle of operation is similar to the FBG hydrophone. Acoustic pressure arising from the acoustic waves can modulate the reflection spectrum of the FBG via the photoelastic effect and possible induced birefringence. However, the wavelength shifts are typically very small; on the other hand, when a pair of FBGs are incorporated into a laser cavity (e.g., the DBR laser), the small modulation on the reflection spectrum is enhanced owing to the feedback (lasing) process. Thus, the acoustic pressure modulates the output power and significantly narrower linewidth of the lasing signal (the linewidth is narrower than the FBG reflection bandwidth), resulting in a greater detection sensitivity [16].

The sparks are induced between two electrodes separated by a distance L (typically less than 1 cm). The acoustic waves

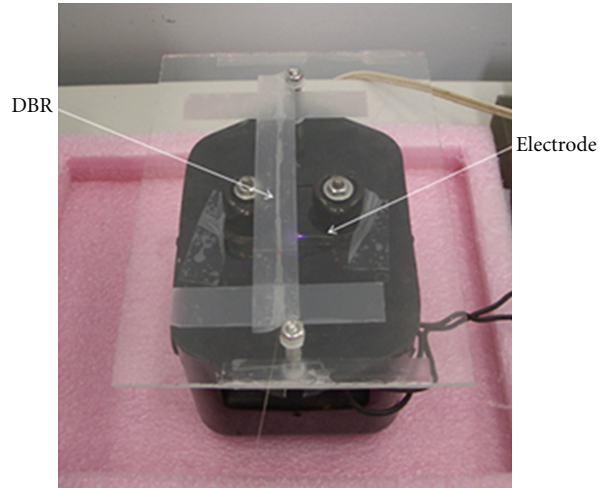


FIGURE 5: Photograph of setup for testing the all-fiber DBR sensor for detecting acoustic waves.

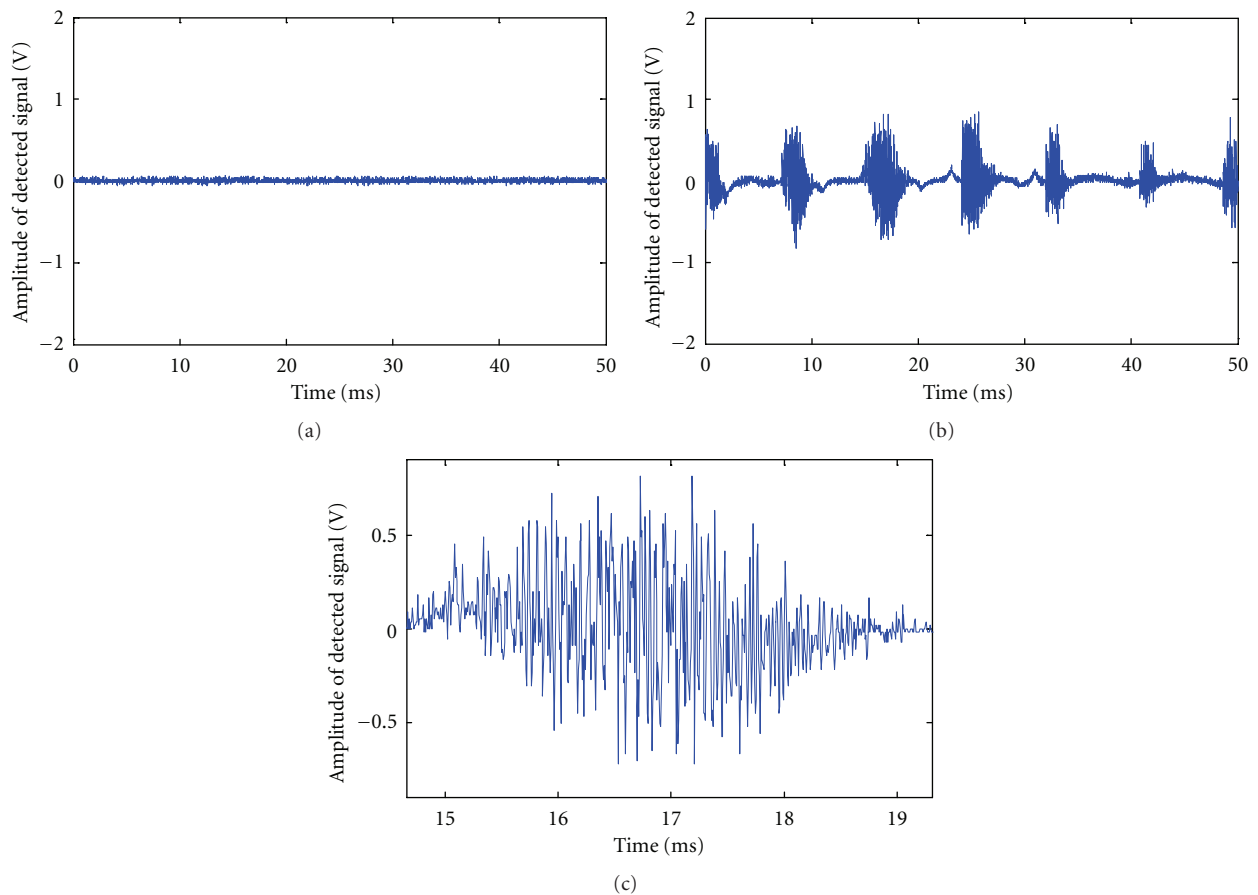


FIGURE 6: Detected signal from the DBR sensor (placed on the plastic plate) when (a) there is no spark and (b) a spark is generated. (c) Zoom of the third period over which the signal reflected from the DBR changes with time for the signal in (b).

distort the entire laser cavity and cause a fluctuation in the output power. We use a 200 kHz photodetector to convert the optical signal from the DBR sensor to an electrical signal measured in time with an oscilloscope. Note that for a single sensor, there is no need to use wavelength-to-power mapping

to detect the changes in power. However, the setup illustrated in Figure 2 can be used to detect the individual response of wavelength-multiplexed DBR sensors.

Figure 6 shows the detected signal when (a) no spark is generated and (b) a periodic spark is generated continuously

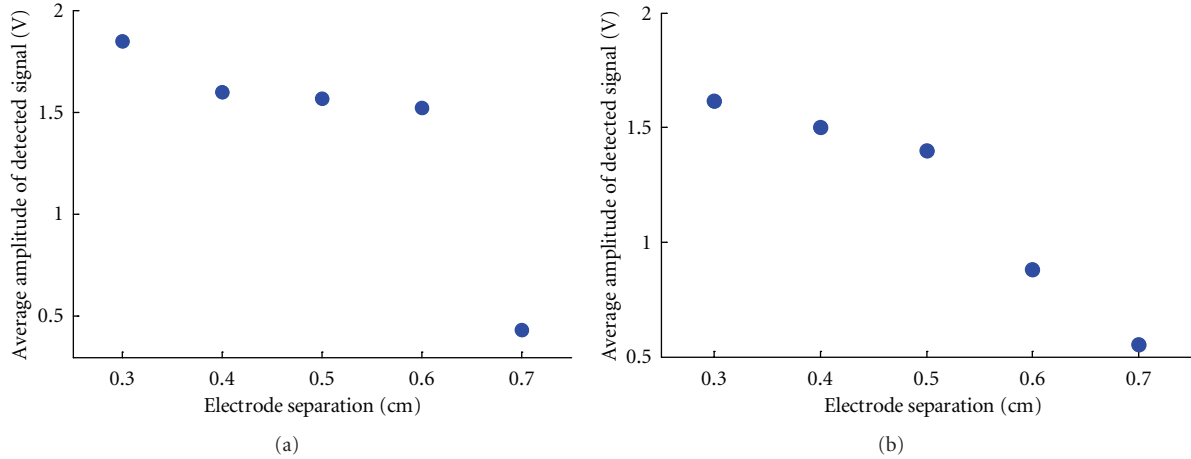


FIGURE 7: (a) Effect of increasing the electrode separation L on the detected signal when the DBR is placed on (a) a plastic plate and (b) a metal plate. H is fixed at 3.5 cm.

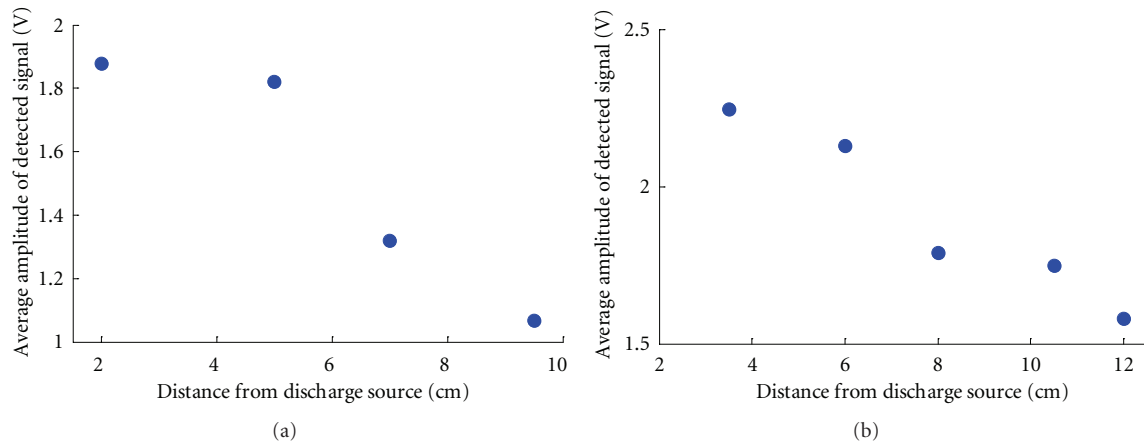


FIGURE 8: Effect of changing the distance H between the spark and detection surface on the detected signal when the DBR is placed on (a) a plastic plate and (b) a metal plate. L is fixed at 0.3 cm.

beneath the plate. As observed, the latter experiences a periodic change in amplitude, showing that the DBR sensor is capable of capturing the acoustic wave emitted by the spark. Figure 6(c) illustrates a zoom of the time-varying signal associated with the acoustic wave.

We then characterize further the performance of the DBR sensor for detecting acoustic waves. First, we keep the distance H of the metal or plastic plate above the location of the spark constant ($H = 3.5$ cm) and vary the electrode separation L . The results are summarized in Figure 7: since increasing L causes a decrease in the strength of the spark, the average maximum peak-to-peak amplitude of the detected signal also decreases. Second, we keep the electrode separation constant ($L = 0.3$ cm) while varying H . As the plates are moved farther from the spark, we expect the detected signal to become weaker, and indeed, this is the case as shown in Figure 8.

Next, we investigate a wavelength multiplexed configuration (see Figure 9) to assess the crosstalk performance. We use two separate DBR sensors, one of which is subject to the acoustic waves arising from the sparks (DBR₁) and the other is isolated from the acoustic waves (DBR₂). As observed in Figure 9(a), when DBR₁ is subject to the acoustic waves generated by the spark, the corresponding detected signal exhibits a periodic voltage variation. On the other hand, as shown in Figure 9(b), there is no variation in detected signal from DBR₂. Figure 10 shows the RF spectra corresponding to the detected signals for DBR₁ and DBR₂. As illustrated, the spectral components of the signal corresponding to DBR₁ are about 50 dB higher than those for DBR₂. These measurements show that DBR₂ is not affected by the changes imposed on DBR₁; this demonstrates that crosstalk is negligible and that the sensors can be used in a wavelength-multiplexed configuration. Note that the use

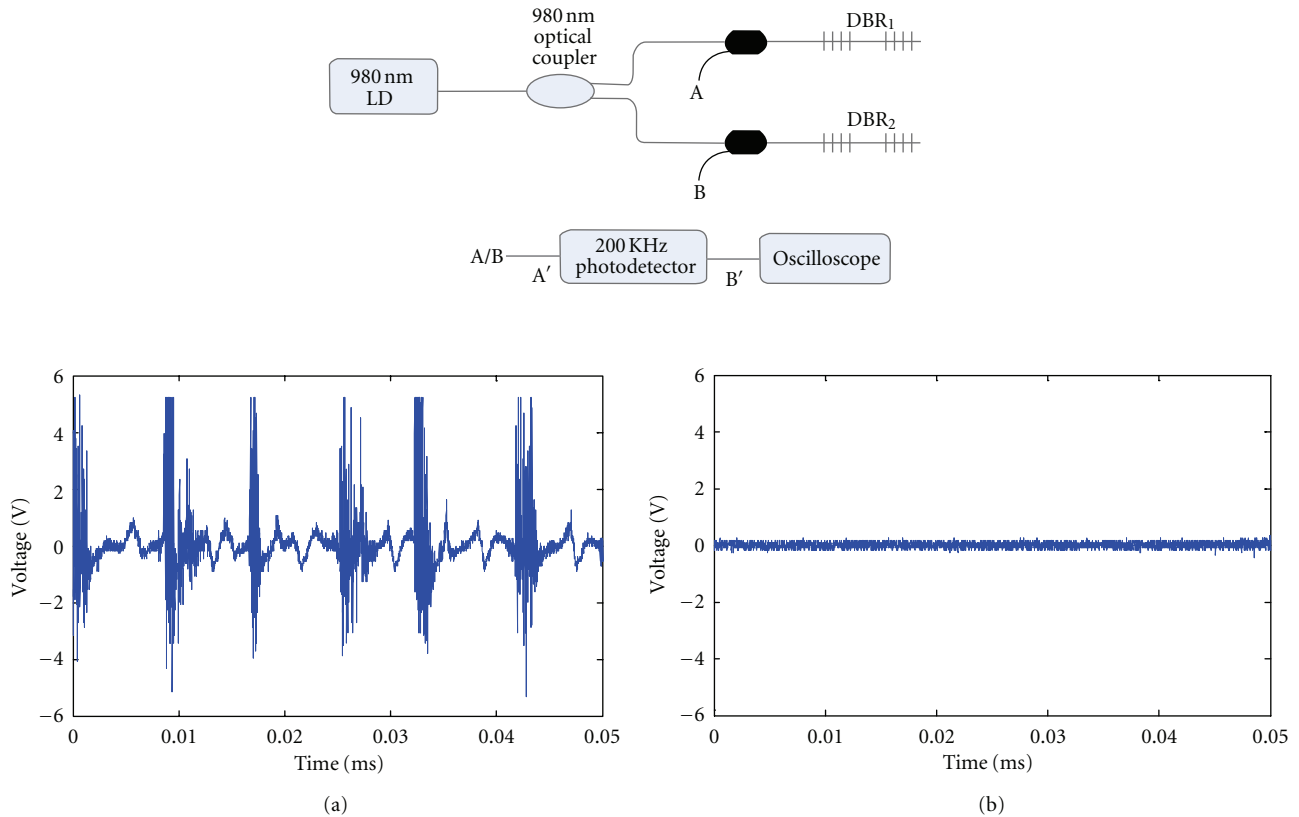


FIGURE 9: Experimental setup used to investigate crosstalk in a multi-DBR system (top). Detected signals from (a) DBR₁ and (b) DBR₂ when DBR₁ is subject to an acoustic wave arising from a spark.

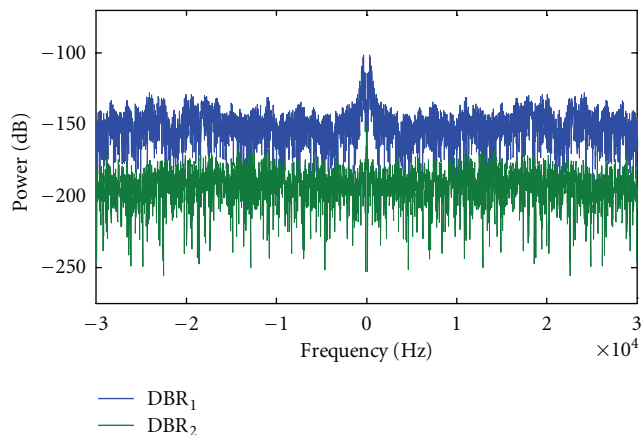


FIGURE 10: RF spectra for the detected signals from DBR₁ and DBR₂.

of different wavelengths allows for locating separate acoustic emissions if the DBR sensors are distributed spatially.

4. Summary

We have characterized the strain response of a DBR laser sensor system incorporating wavelength-to-power mapping. The system is demonstrated with 4 sensors; further scaling is possible, and the number of sensors that can be supported depends in large part on the available pump

power. The measured strain sensitivities of the DBRs range from 0.84 nm/mstrain to 0.88 nm/mstrain and are similar to the typical values of FBGs (1 nm/mstrain). Moreover, we have demonstrated the possibility of using the DBR lasers for detecting acoustic waves transmitted through surfaces. Multiple sensors can be wavelength and spatially multiplexed to locate the spatial distribution of the acoustic waves. We showed that the response from each DBR sensor can be detected independently of the responses of the other sensors in the system, that is, the system is free from crosstalk. We believe that all-fiber DBR lasers can be used for a wide variety of fiber optic sensing applications.

Acknowledgment

This paper was supported in part by the Natural Sciences and Engineering Research Council of Canada via a collaborative research and development grant.

References

- [1] M. Song, S. B. Lee, S. S. Choi, and B. Lee, "Simultaneous measurement of temperature and strain using two fiber Bragg gratings embedded in a glass tube," *Optical Fiber Technology*, vol. 3, no. 2, pp. 194–196, 1997.
- [2] G. Chen, L. Liu, H. Jia, J. Yu, L. Xu, and W. Wang, "Simultaneous pressure and temperature measurement using Hi-Bi fiber Bragg gratings," *Optics Communications*, vol. 228, no. 1–3, pp. 99–105, 2003.

- [3] B. Lee and Y. Jeong, "Interrogation techniques for fiber grating sensors and the theory of fiber gratings," in *Fiber Optic Sensors*, F. T. S. Yu and S. Yin, Eds., pp. 295–382, Marcel Dekker, New York, NY, USA, 2002.
- [4] R. W. Fallon, L. Zhang, A. Gloag, and I. Bennion, "Identical broadband chirped grating interrogation technique for temperature and strain sensing," *Electronics Letters*, vol. 33, no. 8, pp. 705–707, 1997.
- [5] R. Huang, Y. Zhou, H. Cai, R. Qu, and Z. Fang, "A fiber Bragg grating with triangular spectrum as wavelength readout in sensor systems," *Optics Communications*, vol. 229, no. 1–6, pp. 197–201, 2004.
- [6] Y. Sano and T. Yoshino, "Fast optical wavelength interrogator employing arrayed waveguide grating for distributed fiber Bragg grating sensors," *Journal of Lightwave Technology*, vol. 21, no. 1, pp. 132–139, 2003.
- [7] G. Z. Xiao, P. Zhao, F. Sun, Z. Lu, and Z. Zhang, "Arrayed-waveguide-grating-based interrogator for wavelength-modulated multi-fiber-optic sensor applications," *IEEE Photonics Technology Letters*, vol. 17, no. 8, pp. 1710–1712, 2005.
- [8] P. Niewczas, A. J. Willshire, L. Dziuda, and J. R. McDonald, "Performance analysis of the fiber Bragg grating interrogation system based on an arrayed waveguide grating," *IEEE Transactions on Instrumentation and Measurement*, vol. 53, no. 4, pp. 1192–1196, 2004.
- [9] H. Su and X. G. Huang, "A novel fiber Bragg grating interrogating sensor system based on AWG demultiplexing," *Optics Communications*, vol. 275, no. 1, pp. 196–200, 2007.
- [10] F. G. Sun, G. Z. Xiao, Z. Y. Zhang, and Z. G. Lu, "Modeling of arrayed waveguide grating for wavelength interrogation application," *Optics Communications*, vol. 271, no. 1, pp. 105–108, 2007.
- [11] M. I. Comanici and L. R. Chen, "Improved arrayed waveguide grating-based interrogation system for fiber bragg grating sensors," in *Proceedings of the 14th OptoElectronics and Communications Conference (OECC '09)*, Hong Kong, July 2009, Paper Q3.
- [12] M.-I. Comanici, L. R. Chen, and P. Kung, "Measurement of dynamic strain using fiber Bragg grating-based laser sensor system," in *Proceedings of the ICO International Conference on Information Photonics (IP '11)*, pp. 1–2, Ottawa, Ontario, Canada, May 2011.
- [13] Y. Zhao and Y. Liao, "Discrimination methods and demodulation techniques for fiber Bragg grating sensors," *Optics and Lasers in Engineering*, vol. 41, no. 1, pp. 1–18, 2004.
- [14] G. Wild and S. Hinckley, "Acousto-ultrasonic optical fiber sensors: overview and state-of-the-art," *IEEE Sensors Journal*, vol. 8, no. 7, pp. 1184–1193, 2008.
- [15] C. B. Scruby, "An introduction to acoustic emission," *Journal of Physics E*, vol. 20, no. 8, pp. 946–953, 1987.
- [16] B. O. Guan, H. Y. Tam, S. T. Lau, and H. L. W. Chan, "Ultrasonic hydrophone based on distributed Bragg reflector fiber laser," *IEEE Photonics Technology Letters*, vol. 17, no. 1, pp. 169–171, 2005.
- [17] L. Y. Shao, S. T. Lau, X. Dong et al., "High-frequency ultrasonic hydrophone based on a cladding-etched DBR fiber laser," *IEEE Photonics Technology Letters*, vol. 20, no. 8, pp. 548–550, 2008.
- [18] J. Deng, H. Xiao, W. Huo et al., "Optical fiber sensor-based detection of partial discharges in power transformers," *Optics and Laser Technology*, vol. 33, no. 5, pp. 305–311, 2001.
- [19] G. C. Stone, V. Warren, H. G. Sedding, and W. McDermid, "Advances in interpreting partial discharge test results from motor and generator stator windings," in *Proceedings of the International Council of Large Electric Systems (CIGRE '02)*, 2002.
- [20] G. C. Stone, E. A. Boulter, I. Culbert, and H. Dhirani, *Electrical Insulation for Rotating Machines*, Wiley Inter-Science, Danvers, Mass, USA, 2004.
- [21] S. E. U. Lima, O. Frazão, R. G. Farias et al., "Mandrel-based fiber-optic sensors for acoustic detection of partial discharges—a proof of concept," *IEEE Transactions on Power Delivery*, vol. 25, no. 4, pp. 2526–2534, 2010.

Review Article

Photonic Crystal Fibers for Sensing Applications

Ana M. R. Pinto and Manuel Lopez-Amo

Departamento de Ingeniería Eléctrica y Electrónica, Universidad Pública de Navarra, Campus de Arrosadía, Navarra 31006 Pamplona, Spain

Correspondence should be addressed to Ana M. R. Pinto, anamargarida.rodriguez@unavarra.es

Received 5 December 2011; Accepted 2 February 2012

Academic Editor: Wolfgang Ecke

Copyright © 2012 A. M. R. Pinto and M. Lopez-Amo. This is an open access article distributed under the Creative Commons Attribution License, which permits unrestricted use, distribution, and reproduction in any medium, provided the original work is properly cited.

Photonic crystal fibers are a kind of fiber optics that present a diversity of new and improved features beyond what conventional optical fibers can offer. Due to their unique geometric structure, photonic crystal fibers present special properties and capabilities that lead to an outstanding potential for sensing applications. A review of photonic crystal fiber sensors is presented. Two different groups of sensors are detailed separately: physical and biochemical sensors, based on the sensor measured parameter. Several sensors have been reported until the date, and more are expected to be developed due to the remarkable characteristics such fibers can offer.

1. Introduction

Optical fibers (OFs) development in 1966 revolutionized fields such as telecommunications and sensing, leading to the creation of high sensitivity and controlled systems based on light guidance. The remarkable characteristics of fiber optics such as geometric versatility, increased sensitivity over existing techniques, and inherent compatibility with fiber optic telecommunications technology make them stand out for sensing applications. Optical-fibers-based sensors are low cost and efficient solutions for several industries due to their high sensitivity, small size, robustness, flexibility, and ability for remote monitoring as well as multiplexing. Other advantages entail their aptitude to be used even in the presence of unfavorable environmental conditions such as noise, strong electromagnetic fields, high voltages, nuclear radiation, in explosive or chemically corrosive media, at high temperatures, among others. Even though standard optical fibers present an excellent performance in fiber telecommunications, the intrinsic properties of silica have imposed restrictions in the evolution of this technology. The first evident restriction is the material selection for the core and cladding, in order to have matching thermal, chemical, and optical properties. Other limitations are related to its geometry and refractive index profile, which does not allow for freely engineering optical fiber characteristics such as

inherent losses, dispersion, nonlinearity, and birefringence in order to progress in applications such as high power lasers or fiber sensors, among others. These limitations and restrictions have been refined during 30 years of exhaustive research, taking fiber optic technology nearly as far as it could go [1, 2].

The appearance of photonic crystal fibers (PCFs) in 1996 was a breakthrough in fiber optic technology given that these fibers not only had unprecedented properties as they could overcome many limitations intrinsic to standard optical fibers. Photonic crystal fiber geometry is characterized by a periodic arrangement of air holes running along the entire length of the fiber, centered on a solid or hollow core. The major difference between both kinds of fibers relies on the fact that the waveguide properties of photonic crystal fibers are not from spatially varying glass composition, as in conventional optical fiber, but from an arrangement of very tiny and closely spaced air holes which go through the whole length of fiber. In contrast with standard optical fibers, photonic crystal fibers can be made of a single material and have several geometric parameters which can be manipulated offering large flexibility of design. Even more, these fibers offer also the possibility of light guiding in a hollow core, opening new perspectives in fields such as nonlinear fiber optics, fiber lasers, supercontinuum generation, particle

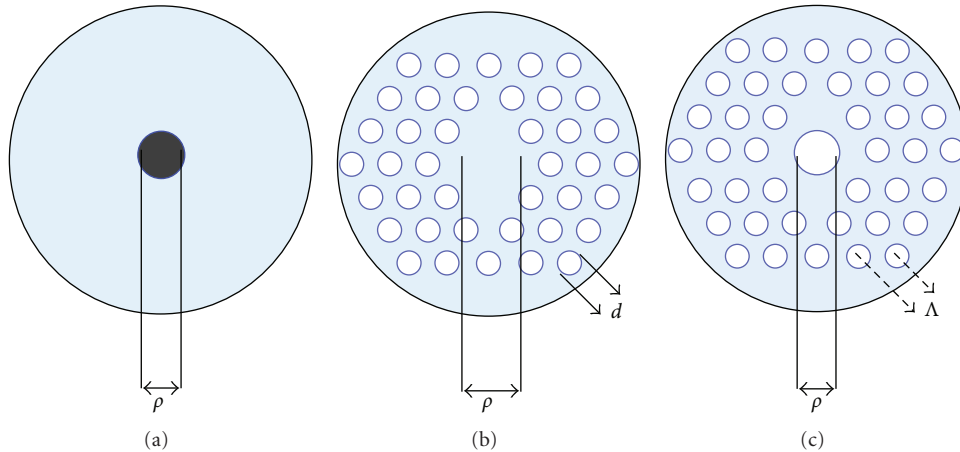


FIGURE 1: Drawing of the cross-section of (a) SMF, (b) solid core PCF, and (c) hollow-core PCF. Colors: blue: silica, grey: doped silica, white: air.

guidance, and fiber sensors [3, 4]. Therefore, there is a high interest of the scientific community in employing photonic crystal fibers in all kind of fields.

This paper provides a qualitative overview of the different fiber sensors based in PCFs. It is structured in five sections. Section 2 explains the geometry-based definition, light guidance and foremost properties in PCFs that make them unique. In Section 3, the applications of PCFs in sensing applications will be detailed. This section is divided in three subsections: physical, chemical, and biosensors. Within Section 4 the technology development opportunities are presented through an overview of the patents of photonic crystal fiber sensors. Conclusions and final remarks are considered in Section 5.

2. Geometry, Guidance Mechanisms, and Properties

Conventional single-mode fibers (SMFs) geometry entails a doped core surrounded by a pure silica cladding (Figure 1(a)), ensuring that the core refractive index is higher than the cladding. Photonic crystal fiber's geometry is characterized by a microstructured air hole cladding running along the entire length of the fiber, which surrounds the core that can be solid or hollow. As so, PCFs can be divided in two families based on their geometry: solid core and hollow-core PCFs. Solid core PCFs, as can be deduced from the name, present a solid core surrounded by a periodic array of microscopic air holes, running along its entire length (Figure 1(b)). Hollow-core photonic crystal fibers (HC-PCFs) present an air hole as core, surrounded by a microstructured air-hole cladding (Figure 1 (c)).

During the modeling as well as the manufacturing process there are different physical parameters to be controlled depending on the kind of fiber to be produced: in an SMF the only parameter to take into account is the diameter of the core, while in a PCF there are three physical parameters to be controlled: the core diameter ρ (which for solid core PCF is defined as the diameter of the ring formed by the innermost

air holes), the diameter of the air holes of the cladding- d and the pitch Λ (distance between the centre of two consecutive air holes). These three physical parameters in combination with the choice of the refractive index of the material and the type of lattice make the fabrication of PCFs very flexible and open up the possibility to manage its properties, leading to a freedom of design not possible with common fibers. Different geometry and different materials will imply different structural design such as to enable different guidance mechanisms through the PCFs: modified total internal reflection (TIR) and/or photonic bandgap guidance (FBG). There are four different guidance mechanisms depending on the PCFs geometry and core/cladding materials [4]:

- (i) index-guiding PCF—guides in a solid core through modified TIR;
- (ii) PBG-guiding PCF—guides through PBG effect in a hollow-core;
- (iii) all-solid PBG PCF—guidance through PBG antiresonant effect in a solid core;
- (iv) hybrid PCF—guidance through simultaneous propagation of FBG and modified TIR.

In the following subchapters, single material solid core PCFs and hollow-core PCFs are simply explained, in order to better understand its geometry and the basic guidance mechanisms of PCFs: modified TIR and FBG. For further reading on the guiding mechanisms in different PCFs we encourage the reader to take a look at [4].

2.1. Solid Core PCFs. Solid core PCFs cross-section presents a periodic array of air holes surrounding a solid core, which are extended invariantly along the fiber length. When using a single material in the fiber manufacturing, this cross-sectional configuration leads to a lowering of the cladding's effective refractive index given that the solid core is made of the same material. An illustration of a solid core PCF cross-section structure is presented in Figure 2(a), based in the first PCF presented in 1996 [5], as well as its refractive index

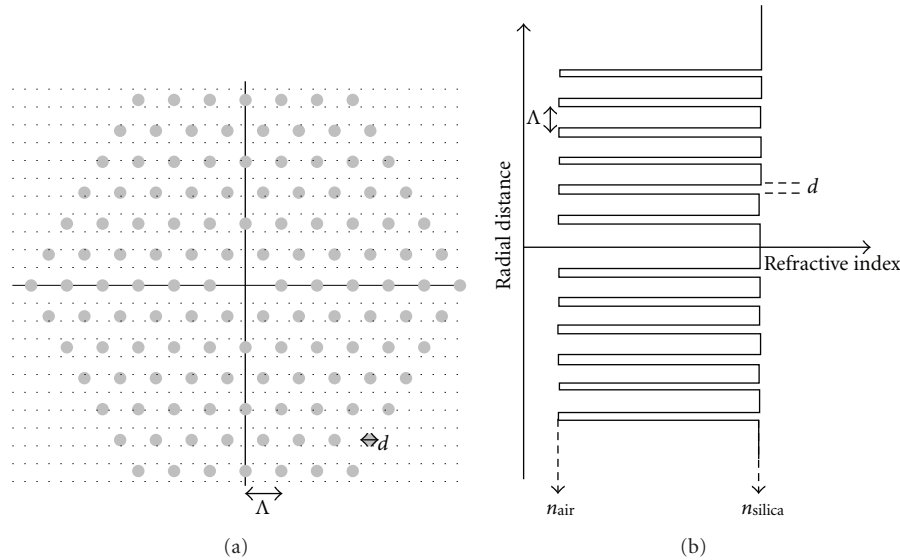


FIGURE 2: Illustration of (a) solid core PCF cross-section and (b) respective refractive index profile; colors: grey: air, white: silica.

variation with the radial distance in Figure 2(b). In solid core PCFs the refractive index in the cladding will vary with the radial distance, depending on its geometry and material.

The effective cladding refractive index will be lowered when compared with the core's refractive index, allowing the guidance mechanism to be total internal reflection, without the need to dope the core, allowing the solid core PCFs to be made with a single material. Since the light guiding properties of solid core PCFs are not a consequence of spatially varying glass composition, as in standard OFs, but from an arrangement of very tiny and closely spaced air holes, the guidance mechanism is known as modified TIR.

Solid-core PCFs flexibility of design can be explored to achieve endlessly single-mode guidance, even when presenting large-mode areas or high birefringence. These features will lead to outstanding opportunities for applications in ever-widening areas of science and technology, like high power handling [6, 7], fiber laser multiwavelength generation [8, 9], long-period gratings inscribed in the solid core [10], supercontinuum generation [11] applied to optical coherence tomography [12] and to spectroscopy [13], and fiber sensor [14], among others. The last application will be developed in detail in the next section.

2.2. Hollow-Core PCFs. PCFs who present a negative core-cladding refractive index difference cannot operate via TIR (Figure 3). However, an appropriately designed holey photonic crystal cladding, running along the entire length of the fiber, can prevent the escape of light from a hollow core, thus becoming possible to break away from the straitjacket of TIR and trap light in a hollow core surrounded by glass. Under these circumstances, light guiding is only possible if a photonic bandgap exists. Light guidance is then an analogue of a mechanism known in solid state physics as the electron conduction mechanism in materials with an energy-band structure. Periodically distributed air holes can form a 2D

photonic crystal structure with lattice constant similar to the wavelength of light. In 2D crystal structures photonic bandgaps exist which prevent propagation of light within a certain range of frequencies. If the periodicity of the structure is broken with a defect, a special region with different optical properties can be created. The defect region can support modes with frequencies falling inside the photonic bandgap, but since around this defect there is a photonic bandgap, light within the defect will remain confined in the vicinity of the defect. Modes falling outside the defect will be refracted, while modes falling inside the defect region will be strongly confined to the defect and guided along it throughout the entire length of the fiber [15].

This effect is illustrated in Figure 4: suppose a hollow-core PCF is designed to work in the red visible region of the electromagnetic spectrum. When the PCF is illuminated by a blue LED, all light will be refracted and no light will be guided by the fiber; consequently no light will come out at the end of the PCF. On the other hand, if the PCF is illuminated by a broadband source the red component of light will be guided appearing at the fiber end and all other frequency components of light (like green or yellow light, represented in Figure 4 for illustrative purposes) will be refracted.

The first bandgap guiding fiber was reported in 1999 [16], demonstrating light confinement and guidance in an air core PCF only at certain wavelength bands, corresponding to the presence of a full 2D band gap in the photonic crystal cladding. This guidance mechanism allows light guidance in air, not possible with standard OFs (for which positive core-cladding refractive index difference is imperative in order to confine light), and presenting noteworthy advantages like extremely small Fresnel reflections, since the refractive index discontinuity between the outside world and the fiber mode can be very tiny; less interaction between guided light and the material forming the fiber core, allowing transmission power levels not possible with conventional fibers, increasing in

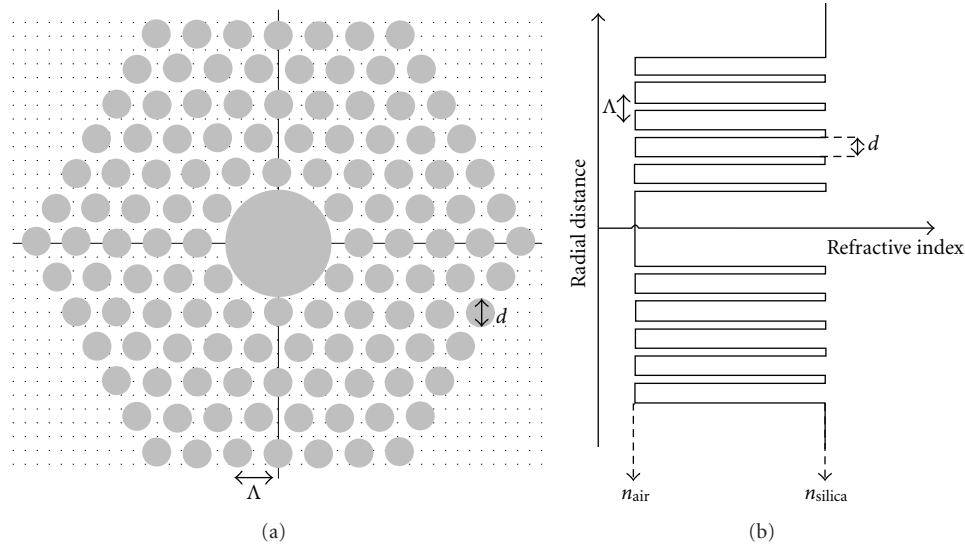


FIGURE 3: Illustration of (a) hollow-core PCF cross-section and (b) respective refractive index profile; colors: grey: air, white: silica.

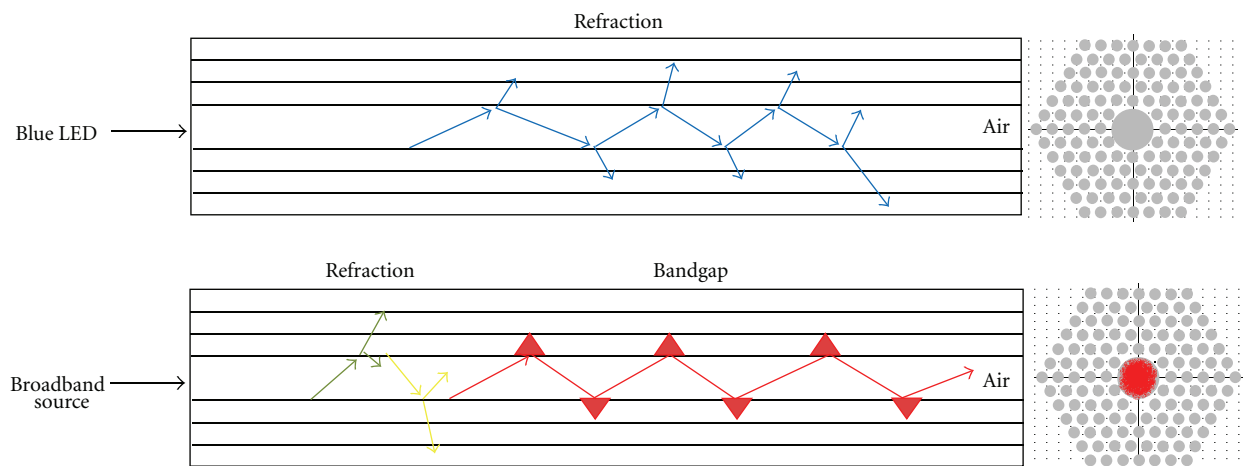


FIGURE 4: Hollow-core PCF guidance of light through PBG.

this way the thresholds powers for lasing based in nonlinear effects; filtering away unwanted wavelengths, since it only works in a range of wavelengths; and the ability to fill the core of the fiber with gases and liquids leading to high light/sample overlapping. These advantages lead to fascinating applications based in HC-PCFs: high power transmission [17], gas-based nonlinear optics [18, 19], optical tweezers propulsion and particle guidance in liquids [20, 21], fiber sensing [22, 23], among others.

3. Sensing Applications

Despite of its youth in the sensing field, PCFs have awakened the interest of many scientific groups due to their promising characteristics. The biggest attraction in PCFs is that by varying the size and location of the cladding holes and/or the core the fiber transmission spectrum, mode shape, non-linearity, dispersion, air filling fraction and birefringence,

among others, can be tuned to reach values that are not achievable with conventional OFs. Additionally, the existence of air holes gives the possibility of light propagation in air, or alternatively provides the ability to insert liquids/gases into the air holes. This enables a well-controlled interaction between light and sample leading to new sensing applications that could not ever be considered with standard OFs. Due to PCFs diversity of features they introduce a large number of new and improved applications in the fiber optic sensing domain [14].

In this section, the applications of PCFs in sensing fields will be detailed, dividing it in two subsections, depending on the parameter that is measured. These two subsections are physical sensors and bio chemical sensors, and each is divided in the several types of sensors.

3.1. Physical Sensors. Physical optic sensors measure physical parameters such as temperature, curvature, displacement,

torsion, pressure, refractive index, electric field, and vibration. The measurement, monitoring, and control of these parameters are of vast interest for several applications. Physical sensors that assess strain/displacement, curvature/bend, transversal load, torsion, and temperature are of immense interest for structural health monitoring. Civil structures like buildings, piles, bridges, pipelines, tunnels, and dams need continuous monitoring with the purpose of controlling and preventing abnormal states or accidents at an early stage, in order to avoid casualties as well as giving maintenance and rehabilitation advice [24]. Physical fiber sensors are perfect for this purpose, since they provide *in situ*, continuous measurement and analysis of key structural and environmental parameters under operating conditions [25, 26]. Other physical sensors like pressure and refractive index find applications in fields such as medicine and biochemistry, while electric and magnetic field fiber sensors are of enormous benefit for sensing at high voltages, since they provide an insulating link to high-voltage areas (not offered by conventional electric sensors) [27].

3.1.1. Curvature/Bend Sensors. Curvature or bend is an important physical parameter due to its multiarea applications. Application fields such as structural health, robot arms, and artificial limbs insure that lot of attention is paid to the development of these sensors. The first PCF-based bend sensor was presented in 2000 [28]. This bend sensor was developed by the use of a three solid core all-silica PCF used as multi-axis bend sensor, presenting high accuracy in laboratory and in trials on a bridge. A year after, a curvature sensor with a sensitivity of 127 rad/rad was obtained with a two-solid core PCF (made entirely of silica) used as the sensing element, acting as a two-beam interferometer in which the phase difference was a function of the curvature applied to it [29]. Interferometric configurations are in general very popular techniques for the measurement of physical parameters. Sagnac interferometers are very popular for PCF-based fiber optic sensors due to their high extinction ratio, short length of fiber needed (when compared with SMF), and high insensitivity to temperature [30]. Using a highly birefringent (Hi-Bi) solid core pure silica PCF with two asymmetric hole regions in a Sagnac interferometer, curvature measurements were made through the group birefringence, with insensitivity to strain and temperature [31]. In contrast, a curvature fiber sensor was also obtained through a low birefringence solid core silica PCF Sagnac interferometer [32]. Another interferometric configuration often used in the development of fiber sensors is the Mach-Zehnder interferometer (MZI). An all-fiber MZI interferometer for curvature measurement was fabricated by collapsing both ends of an endlessly single-mode (ESM) large-mode area (LMA) pure silica PCF connected to a SMF in a ring down loop [33]. Another ESM silica-core PCF-based MZI was performed by splicing a section of this PCF between two SMFs in order to obtain a bend sensor with a sensitivity of 3.046 nm.m [34]. A temperature insensitive curvature sensor (2.826 nm.cm) was also obtained by producing a core-offset induced interferometer, constructed between a SMF and an all silica solid core polarization maintaining PCF [35]. Long

period gratings (LPGs) can also be used as bend sensors. These structures are formed by introducing a periodic perturbation of refractive index or structural geometry along the fiber length, resulting in resonant coupling from the fundamental core mode to copropagating cladding modes which produce a series of attenuation dips in the transmission spectrum. Bending-induced stress to an LPG can be observed by detecting the shift in the resonance wavelength or splitting of the resonance dip. LPGs were inscribed in ESM PCF showing sensitivities of 3.7 nm.m [36] and 27.9 nm.m [37]. A study of bend sensors based in symmetric and asymmetric LPGs inscribed in PCFs was preformed, demonstrating that asymmetric LPGs are spectrally sensitive to bend orientation (showing attenuation bands producing red and blue wavelength shifts) while symmetric LPGs induced bend presented only a unidirectional wavelength shift [38]. Furthermore, a directional bend sensor based in a LPG inscribed in an LMA all-silica PCF was also produced, with a sensitivity of 2.26 nm.m [39].

3.1.2. Displacement/Strain Sensors. There are a number of applications of practical interest in which the monitoring of strain/displacement-induced changes is important. Application areas for which strain/displacement monitoring is important entail experimental mechanics, aeronautics, metallurgy, and health monitoring of complex structures, among others. In order to meet the increasing measurement requirements of modern industry, different types of strain/displacement sensors based on electronic or fiber-optic techniques have been developed. The electrical sensors are the most mature and widely used strain/displacement sensors. The use of the electrical sensor presents several drawbacks such as short lifetime under high temperature, nonlinear distortion, and susceptibility to electromagnetic interference. Compared with the electronic displacement/strain sensors, the fiber-optic-based sensors have the advantages of immunity to electromagnetic interference, light weight, remote sensing ability, and multiplexing capability. The use of PCFs for strain/displacement sensing allows new possibilities and enhanced solutions. To date a number of designs using PCFs have been reported based in polarization and interferometry. A polarimetric strain sensor based in an all-silica Hi-Bi PCF was demonstrated with a sensitivity of 1.3 pm/ $\mu\epsilon$ [40]. Modal interferometers constructed through tapering solid core silica PCFs were also proposed for strain sensing [41, 42]. A high sensitive (~ 2.8 pm/ $\mu\epsilon$) wavelength encoded strain sensor was reported to be able to be interrogated by a battery-operated light-emitting diode and a miniature spectrometer, in which the sensing head was a modal interference obtained by splicing a piece of PCF to an SMF [43]. Another modal interferometer was obtained through the structure composed by SMF-PCF-SMF with a core offset at one of the joints. When embedding this interferometer in a cured carbon fiber composite laminate an intensity-modulated microdisplacement sensor presenting 0.0024 dB/ μm was obtained [44]. Miniature inline Fabry-Perot (FP) interferometers were also accomplished for strain sensing: by splicing a small length of hollow-core photonic bandgap fiber between two SMFs in order to obtain a strain

sensitivity of $1.55 \text{ pm}/\mu\epsilon$ and insensitivity to temperature and bend [45] or even by multiplexing several FP interferometers based in HC-PBFs between two SMFs to obtain a strain sensor system [46]. Other authors approach to strain sensing was through Hi-Bi PCF-based Sagnac interferometers, as the one presented in Figure 5. Strain sensors developed through Hi-Bi PCF Sagnac interferometers were reported showing temperature insensitivity, using wavelength-based measurement ($\sim 1.11 \text{ pm}/\mu\epsilon$) [47] and intensity-based measurement ($\sim 0.0027 \text{ dB}/\mu\epsilon$) [48]. Using a Hi-Bi PCF in a Sagnac interferometer a displacement sensor was reported with a sensitivity of $0.28286 \text{ nm}/\text{mm}$ [49]. Through the use of a three-hole suspended-core fiber (SCF) in a Sagnac configuration a displacement sensor was developed with high precision ($\sim 0.45 \mu\text{m}$) [50]. An MZI was fabricated by splicing a short length of PCF between two SMFs with collapsed air holes over a short region in the two splicing points. This fiber ringdown loop showed a high strain sensitivity $\sim 0.21 \mu\text{s}^{-1}/\text{m}\epsilon$ and a minimum detectable strain of $\sim 3.6 \mu\epsilon$ [51].

3.1.3. Electric and Magnetic Field Sensors. Electric and magnetic field sensing is a very important issue in high- and low-tension structures, such as the ones present in the electric power industry. Conventional sensors usually use antennas, conductive electrodes, or metal connections. Due to their metallic content, conventional sensors are very likely to often perturb the measured parameter. Fiber optic sensors are widely used in these applications because unlike their conventional counterparts, fiber-optic-based sensing techniques minimally disturb the electric or magnetic field, and apart from the sensor head, the connecting fibers are inherently immune to electromagnetic interference. Most importantly, they can provide true dielectric isolation between the sensor and the interrogation system in the presence of very high electromagnetic fields. A wide variety of fiber-optic-based sensing schemes have been proposed and reported to date. However, such schemes have a number of disadvantages such as high coupling losses, limited mechanical reliability, and difficulties in mass production. Ideal fiber-based field sensors should present properties such as small size, simple design, and an all-fiber configuration with high measurement accuracy. A polarimetric sensing scheme with selectively liquid-core-(LC-) infiltrated Hi-Bi PCF (infiltrated section $< 1 \text{ mm}$) was demonstrated for electric field sensing with a sensitivity of $\sim 2 \text{ dB}$ per $\text{kV}_{\text{rms}}/\text{mm}$ [52]. LCs are materials which present external field-dependent optical anisotropy and high birefringence. Infiltration of LC materials makes the PCF susceptible to external field variations, a property which can be utilized to fabricate all-fiber current sensors [53, 54]. The directional electric field sensitivity of the same LC-infiltrated PCF probe was also demonstrated, showing that the sensor probe has higher sensitivity to the electric field component aligned along the Hi-Bi PCF axis [55]. An intensity-measurement-based electric field sensor was reported by infiltrating an LMA PCF with an LC (infiltrated section $< 1 \text{ cm}$), demonstrating a sensitivity of $\sim 10.1 \text{ dB}$ per $\text{kV}_{\text{rms}}/\text{mm}$ in transmission and $\sim 4.55 \text{ dB}$ per $\text{kV}_{\text{rms}}/\text{mm}$ in reflection [56]. The growth of magnetic field PCF-based

sensors is at slow pace. The development of a spun elliptically birefringent PCF with reduced temperature dependence [57] showed the advantages of this PCF over conventional spun stress birefringence fibers, opening the possibility for magnetic sensing with PCFs. The development of a magneto-optic Faraday effect in a miniature coil wound from a six-hole spun PCF [58] provided information about the ability of this PCF to efficiently accumulate Faraday phase shift in a magnetic field even when the fiber is wound into a coil of very small diameter. By using a Hi-Bi PCF injected with a small amount of Fe_3O_4 nanofluid a sensitivity of $242 \text{ pm}/\text{mT}$ was shown [59]. A magnetic field sensor based on the integration of a high birefringence photonic crystal fiber and a composite material made of Terfenol particles and an epoxy resin was demonstrated with a sensitivity of $0.006 \text{ nm}/\text{mT}$ over a range from 0 to 300 mT with a resolution $\pm 1 \text{ mT}$ [60]. Recently, a magnetic field measurement sensitivity of $\sim 33 \text{ pm}/\text{Oe}$ was obtained using an HC-PCF sensor based on the characteristic of magnetic-controlling refractive index [61].

3.1.4. Pressures Sensors. Pressure measurements are required in various industrial applications within extremely harsh environments such as turbine engines, compressors, oil and gas exploitations, power plants and material processing systems. Conventional sensors are often difficult to apply due to the high temperatures, highly corrosive agents or electromagnetic interference that may be present in those harsh environments. Fiber optic pressure sensors have been proved themselves successful in such harsh environments due to their high sensitivity, wide bandwidth, high operation temperature, immunity to electromagnetic interference, lightweight and long life. Using periodically tapered LPGs written in a ESM PCF, measurements of hydrostatic pressure up to 180 bar showing a pressure sensitivity of 11.2 pmbar^{-1} were carried out [62]. A very popular technique for pressure sensing is polarimetric measurement. Several authors reported polarimetric studies and measurements leading to the development and application of pressure sensors based in the commercial Hi-Bi PCF: a study of pressure sensing with this PCF at three different temperatures showed its temperature insensitivity, while simultaneously measuring pressure variations [63]; an intensity measurement of pressure with a sensitivity of $2.34 \times 10^{-6} \text{ MPa}^{-1}$ was later demonstrated [64]; and a wavelength measurement of pressure variation was shown to provide a sensitivity of $3.38 \text{ nm}/\text{MPa}$ with an operating limit of 92 MPa [65], which lead to an practical application, Tsunami sensing, since the high pressure sensitivity join with temperature insensitivity makes this sensor suitable to work in a harsh environment such as the ocean bottom [66]. Other polarimetric sensors were developed based in home-made Hi-Bi PCFs: a polarimetric measurement to a specially designed fiber showed a pressure of $-10 \text{ rad}/(\text{MPa}\cdot\text{m})$ [67]; by using two fibers with a small number of cladding holes with different diameters, in order to induce birefringence, a sensitivity up to $23 \text{ rad}/\text{MPa}\cdot\text{m}$ was obtained [68]; and using two different germanium doped-core Hi-Bi PCFs to measure pressure a sensitivity that exceeds $43 \text{ rad}/\text{MPa}\cdot\text{m}$ and low sensitivity to temperature were reported [69]. As for so many other

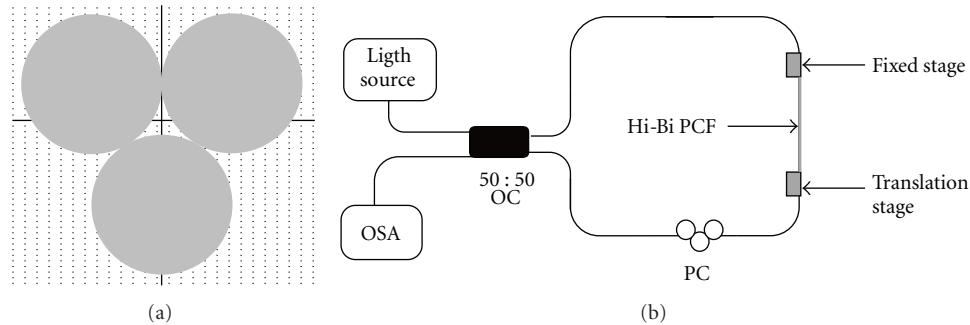


FIGURE 5: Schematic representation of (a) three-hole SCF cross-section [grey-air, white-silica] and (b) Sagnac interferometer set up for strain measurement.

physical sensors, the Sagnac interferometer configuration is also used to sense pressure. Using a commercial Hi-Bi PCF in a Sagnac interferometer a temperature insensitive pressure sensor with 3.42 nm/MPa at 1550 nm was obtained [70]. This sensor sensitivity was later improved by the utilization of the Hi-Bi PCF coiled inside the Sagnac loop, reaching a sensitivity of 4.21 and 3.24 nm/MPa at 1320 nm and 1550 nm, respectively [71]. Through the use of a four-hole SCF, two different interferometric configurations were used for pressure sensing, showing two very different sensitivities to pressure with residual temperature sensitivity [72]. One of the configurations is a FP cavity made by splicing the SCF in between a SMF and a hollow-core fiber, showing sensitivity to pressure variations of 4.68×10^{-5} nm/psi. And the other configuration, showing much higher sensitivity (0.032 nm/psi), is made through a Sagnac interferometer with the SCF.

3.1.5. Temperature Sensors. Fiber optic sensors have proven to be very useful in measuring temperatures in basic metals and glass productions, in critical turbine areas typical in power generation operations, rolling lines in steel, furnaces of all sorts, sintering operations, ovens and automated welding equipment (which often generate large electrical fields, disturbing conventional sensors). Other applications were OFs-based temperature measurement is quite efficient is in high temperature processing operations in cement and chemical industries. Semiconductor industry also takes advantage of FO remarkable characteristics in temperature sensing, especially in fusion, sputtering, and crystal growth processes. Industries such as civil, aerospace, and defense make lot of use of this sensor to monitor and control their structures health. This kind of FO sensor is one of the most required in the commercial market due to the high number of applications in so different areas. Consequently, temperature-based PCFs sensors were quickly developed aiming to produce new sensors with improved characteristics, mainly improved sensibility and stability. Studies to understand the influence of the geometry and the material quality in the Hi-Bi PCF sensitivity to temperature were developed [73]. A polarimetric interrogation to this kind of Hi-Bi PCF showed a sensitivity of 0.136 rad/ $^{\circ}$ C at 1310 nm [74]. Using modal interference other temperature

sensors were reported: by tapering a solid silica-core PCF, a sensitivity of 12 pm/ $^{\circ}$ C was obtained for measurements up to 1000 $^{\circ}$ C [75]; using an LMA PCF spliced to an SMF a three-beam path modal interferometer with a sensitivity of 8.17 pm/ $^{\circ}$ C was reported [76]; a strain-independent modal interferometer for temperature sensing (sensitivity \sim 73 pm/ $^{\circ}$ C) was accomplished by an induced core offset of a nonlinear PCF in-between of a multimode fiber (MMF) and a SMF [77]. MZIs using LPGs in a PCF with a sensitivity of 42.4 pm/ $^{\circ}$ C [78] and an all-solid PBF (doped fiber) with enhanced temperature sensitivity 71.5 pm/ $^{\circ}$ C were demonstrated [79]. Hybrid FP structures were also developed for temperature sensing: been by forming a sensing head by two FP cavities formed by fusion splicing a PCF with a short piece of hollow-core fiber and an SMF in series [80], or by splicing SMF to a short piece of SCF (end cleaved) forming a miniature FP sensor head and interrogating it with a dual-wavelength Raman fiber laser for unambiguous temperature recovery (sensitivity \sim 0.84 deg/ $^{\circ}$ C) [81], or by inserting the FP interferometer in a laser cavity as a mirror for simultaneous sensing and lasing (sensitivity \sim 6 pm/ $^{\circ}$ C) [82]. The inscription of LPGs in a solid core PCF was also tried for temperature sensing showing a sensitivity of 10.9 pm/ $^{\circ}$ C [83]. Sagnac interferometers were built making use of filled PCFs for temperature sensing: using a two-hole birefringent PCF filled with metal indium it was possible to achieve a sensitivity of 6.3 nm/K [84] and by filling a Hi-Bi PCF with alcohol a sensitivity as high as 6.6 nm/ $^{\circ}$ C was reached [85]. Sagnac interferometers do not only use filled PCFs for temperature sensing. In reality, the most common and recent approach for temperature measurement using PCF is filling them with a liquid. By filling the fiber with quantum dots two different temperature sensors were developed: been by depositing quantum dots nanocoatings through the Layer-by-Layer technique in the inner holes of an all-silica LMA ESM PCF with a resultant sensitivity of 0.1636 nm/ $^{\circ}$ C [86] or by inserting them in a hollow core of a PCF obtaining a sensitivity of 70 pm/ $^{\circ}$ C [87]. By filling the air holes of the cladding of a solid core PCF with Fe₃O₄ nanoparticle fluid a temperature sensitivity of 0.045–0.06 dB/ $^{\circ}$ C depending on the length of the fiber (5 cm–10 cm) was accomplished [88]. By filling 10 cm of solid core PCFs with a less expensive liquid like ethanol a sensitivity of

0.315 dB/°C was reported [89]. When selectively infiltrating one of the air holes of a solid core PCF with a 1.46 refractive index liquid the sensitivity to temperature was proved to be ~ 54.3 nm/°C [90]. Distributed Brillouin temperature sensing was also accomplished using PCFs: through the use of a germanium doped-core birefringent PCF with variations of 0.96–1.25 MHz/°C [91] and by using the birefringent effect of a transient Brillouin grating in a polarization-maintaining PCF leading to a sensitivity of 23.5 MHz/°C [92].

3.1.6. Torsion/Twist Sensors. Torsion measurement and control is important in civil engineering applications such as bridges, buildings, and others. A polarimetric torsion sensor based in a Hi-Bi PCF (see Figure 6) was reported to present a sensitivity of ~ 0.014 /° in a linear twist angle ranging from 30° to 70° [93]. Several Sagnac-based structures were reported for torsion sensing: a two-LP-mode operation Hi-Bi PCF was demonstrated to measure the twist angle with a resolution of ~ 2.7 ° and low sensitivity to temperature [94]; a temperature and bend insensitive torsion sensor based in Hi-Bi PCF with enlarged air holes in one axis was achieved, showing a sensitivity of ~ 0.06 nm/° [95]; a sensor able to measure the torsion angles and direction simultaneously was reported though a side-leakage PCF (sensitivity ~ 0.9354 nm/°) [96] and a Sagnac based in an LMA PCF torsion sensor was reported with a sensitivity of 1 nm/° and a resolution of 0.01° [97]. The use of LPGs is also common for this kind of sensor: by mechanically inducing an LPG in an all-silica solid core PCF a torsion sensitivity of 0.73 nm/ 2π was obtained [98] and by inducing LPGs in two different PCFs a dependency on the asymmetry of the cladding structure is noticed to obtain high sensitivity 12.4 nm/(rad/cm) [99].

3.1.7. Transversal Loading Sensors. Transversal load is also a very important parameter to monitor and health of civil structures. A polarimetric transverse load sensor was reported using a Hi-Bi PCF with larger air holes on one axis, presenting a sensitivity of ~ 2.17 nm/(N/cm) [100]. Several authors opted for inscribing fiber Bragg gratings (FBGs) in solid core PCFs. By using an FBG in a two-hole PCF, a sensitivity of 17.6–26 pm/(N/cm) was shown [101]. By embedding an FBG Hi-Bi PCF in a reinforced composite material a sensitivity of 15.3 pm/MPa was achieved [102]. This leads to a study of transversal load characteristics in different PCFs with inscribed FBGs. This study reported that increasing transverse load shifts the Bragg wavelength to longer values and that the FBG PCF sensitivity to transverse load decreased with increasing volume of air-holes around the core, and even more, a dependence on the fiber orientation was observed [103]. A four-hole SCF was inscribed with FBGs and tested for transverse load. It was demonstrated that SCFs experience sensitivities going from 2.19 pm/(N/cm) to 12.23 pm/(N/cm) depending on where the load is applied transversely [104]. Other structures also used in transversal load sensing are Sagnac interferometers. Two Sagnac interferometers were developed based in the same LMA PCF for transverse load measurement: by measuring the transverse

displacement of the PCF coil (sensitivity of 90.4 nm/mm), the sensitivity to load variations is enhanced while the sensitivity to temperature is decreased, when compared with the SMF case [105]; and by direct measurement of the transmission spectrum shift corresponding to the measured mechanical load a sensitivity of 0.519 nmN⁻¹ mm⁻¹ was achieved [106].

3.1.8. Refractive Index Sensors. Refractive index is a fundamental material property. Consequently, its accurate measuring is crucial in many applications. In food or beverage industries, the monitoring of refractive index is part of the quality control, and the development of simple and compact refractometers is key. Optical fiber refractive index sensors are attractive, owing to their small size, flexibility in their design, immunity to electromagnetic interference, network compatibility, and the aptitude for remote and *in situ* measurements. FBGs writing in a three-hole germanium-doped-core SCF were reported with a resolution of 3×10^{-5} and 6×10^{-6} around mean refractive index values of 1.33 and 1.4 [107]. LPG-based devices offer high sensitivity to the refractive index variations of the surrounding medium. Refractive index measurement within a solid core PCF inscribed with LPGs was reported, where the coherent scattering at the cladding lattice is used to optically characterize materials inserted into the fiber holes—liquid water to solid ice transition is characterized through the refractive index determination [108]. A high sensitive refractive index sensor based in LPGs inscribed in an ESM PCF was reported presenting a wavelength-measured sensitivity of 440 nm/RIU and an intensity-measured sensitivity of 2.2 pm/°C [109], presenting suitable characteristics for applications such as label-free bio sensing [110]. By inscribing LPGs in air and water filled solid core PCFs an excellent sensitivity of $\sim 10^{-7}$ RIU within a index range of 1.33 and 1.35 for air-filled was shown [111]. A highly sensitive approach (1500 nm/RIU) was reported based in LPGs inscribed in a LMA PCF (see Figure 7(a)) [112]. Modal interference seems to be a very used technique for refractive index sensing with PCFs. A LMA tapered PCF with collapsed air holes was demonstrated for refractive index sensing with a resolution of 1×10^{-5} RIU [113] and direct application in gas sensing [114]. The core mode couples to multiple modes of the solid taper waist, which can be seen at the output as interference peaks that shift with refractive index variations. Another approach taken was an in-reflection PCF interferometer (see Figure 7(b)), obtained by splicing an SMF to an LMA PCF [115]. In the splice, the voids of the PCF are collapsed allowing coupling of PCF core and cladding modes. An ultrasensitive PCF-based refractive index was reported with a sensitivity of 30100 nm/RIU, by inserting the fluid in one of the adjacent air holes to the core [116]. The core mode can couple with the mode of this microfluidic channel with a strong field overlap. Another two modal interferometer-based refractive index PCF sensors were developed: one based in an LMA spliced between two SMFs presenting a maximum resolution of $\sim 2.9 \times 10^{-4}$ RIU [117] and the other based in two large-core air-clad PCF spliced in between SMFs in series, presenting a resolution

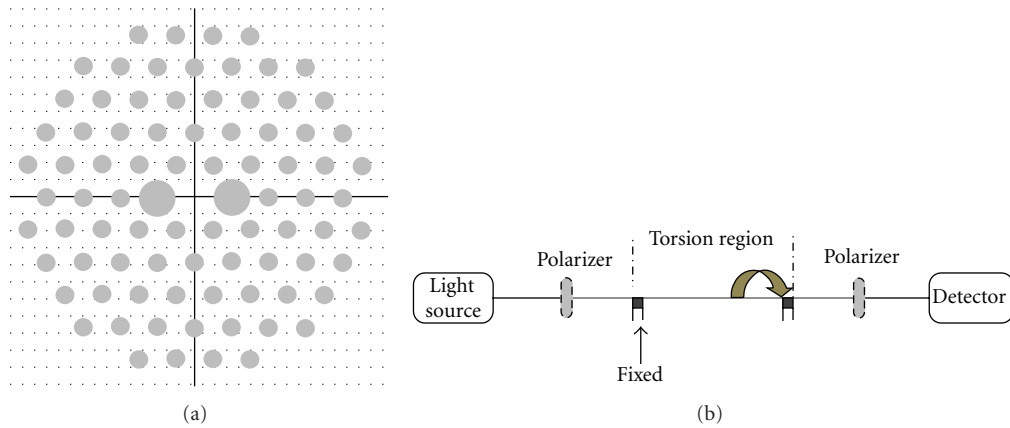


FIGURE 6: Schematic representation of (a) Hi-Bi PCF cross-section (grey: air, white: silica) and (b) polarimetric configuration for torsion measurement.

of $\sim 3.4 \times 10^{-5}$ RIU [118]. The refractive index response of a modal interferometer based on a PCF using a thin plasma deposited silicon nitride overlay with high refractive index was demonstrated, showing improved refractive index sensitivity [119]. An MZI-based refractometer was also developed using a LMA PCF in a cavity ringdown loop, with a resolution of 7.8×10^{-5} RIU [120]. A refractive index sensor based in four-wave mixing (FWM) in a PCF was reported presenting a high sensitivity of $\sim 8.8 \times 10^3$ nm/RIU [121]. Photonic bandgap-based refractive index sensing was as well demonstrated: by a wavelength shift falling inside the PBG due to refractive index variations (resolution of 2×10^{-6} RIU) [122], or by observing the PBG shift in two types of all-solid core PCF with a series of high refractive index infiltrations (resolution of $\sim 10^{-6}$ RIU) [123], or even by using a hollow-core low-refractive index contrast Bragg fiber to infiltrate different aqueous analytes in order to observe high refractive index sensing (sensitivity ~ 1400 nm/RIU) [92].

3.1.9. Vibration Sensors. The dynamic loading of a structure gives rise to induced vibrations, which usually occur at a frequency close to the natural frequency of such structure, potentiating structural or mechanical failure, which results in severe damage to the structure in certain situations. In this context, monitoring and detecting damage caused by vibrations in structures at an early stage is very important. As so controlling constantly, and possibly remotely, parameters such as the vibration amplitude and frequency are extremely important to detect structural damages in rotor blades, aircraft fuselages, and wing structures, and so forth. Fiber optic sensors play a special role in this field due to their small size, immunity to electromagnetic interferences, and, in the case of using single material PCFs, high insensitivity to temperature variations. Only recently, vibration measurements using PCFs were demonstrated: by using a Hi-Bi PCF embedded in a glass-fiber-reinforced polymer for high sensitivity vibration measurements up to 50 Hz [124] and by using a polarization maintaining PCF embedded also in a glass polymer composite material showing reliable frequency and amplitude measurements of vibrations and

with a sensitivity of ~ 0.253 dB/mm [125]. In both fiber sensors, polarization maintaining or Hi-Bi PCFs were chosen due to their negligible level to temperature-vibration cross coupling.

3.1.10. Multiparameter Sensing. Several sensors are able to measure two or more parameters simultaneously. The most common parameters simultaneously measured are strain and temperature. A distributed Brillouin sensing system was developed through the use of a germanium-doped PCF, resulting in a highly precise simultaneous measurement of temperature (sensitivity ~ 0.96 – 1.25 MHz/ $^{\circ}$ C) and strain (sensitivity ~ 0.048 – 0.055 MHz/ $\mu\epsilon$) [126]. By amplifying a Hi-Bi PCF through an erbium-doped fiber, a polarimetric measurement of temperature and strain was made presenting sensitivities of 0.04 dB/ $^{\circ}$ C and 1.3 pm/ $\mu\epsilon$, respectively [127]. An FBG inscribed in a erbium-doped-core PCF showed a sensitivity to strain of 1.2 pm/ $\mu\epsilon$ and a sensitivity to temperature of 20.14 pm/K [128]. Strain and temperature simultaneous measurement was also demonstrated using FP cavities. A hybrid FP cavity was obtained by splicing SCF at the end of an SMF, using three-hole and four-hole SCFs. The hybrid structure characterization was done through wavelength and phase variations: the strain sensitivity was 1.32 pm/ $\mu\epsilon$ and 10.4 rad/m $\cdot\mu\epsilon$ for the three-hole SCF case and for the four-hole SCF 1.16 pm/ $\mu\epsilon$ and 8.5 rad/m $\cdot\mu\epsilon$; the temperature sensitivity for the three-hole SCF was 7.65 pm/ $^{\circ}$ C and 67.8 rad/m \cdot° C and for the four-hole SCF 8.89 pm/ $^{\circ}$ C and 67.6 rad/m \cdot° C [129]. Other FP configuration was developed by splicing an HC-PCF in-between two SMFs, presenting sensitivities to temperature and strain of 1.4 pm/ $^{\circ}$ C and 5.9 nm/ $\mu\epsilon$, respectively [130]. As it is for individual strain and temperature measurements, for the simultaneous measurement of these two parameters the Sagnac interferometer is a very popular approach. A Sagnac interferometer was developed based in a four-hole SCF, resulting in a strain sensitivity of ~ 1.94 pm/ $\mu\epsilon$ and temperature sensitivity of ~ 0.3 pm/ $^{\circ}$ C [131]. By using a Hi-Bi PCF in a Sagnac configuration previously amplified by an erbium-doped fiber, strain and temperature can be

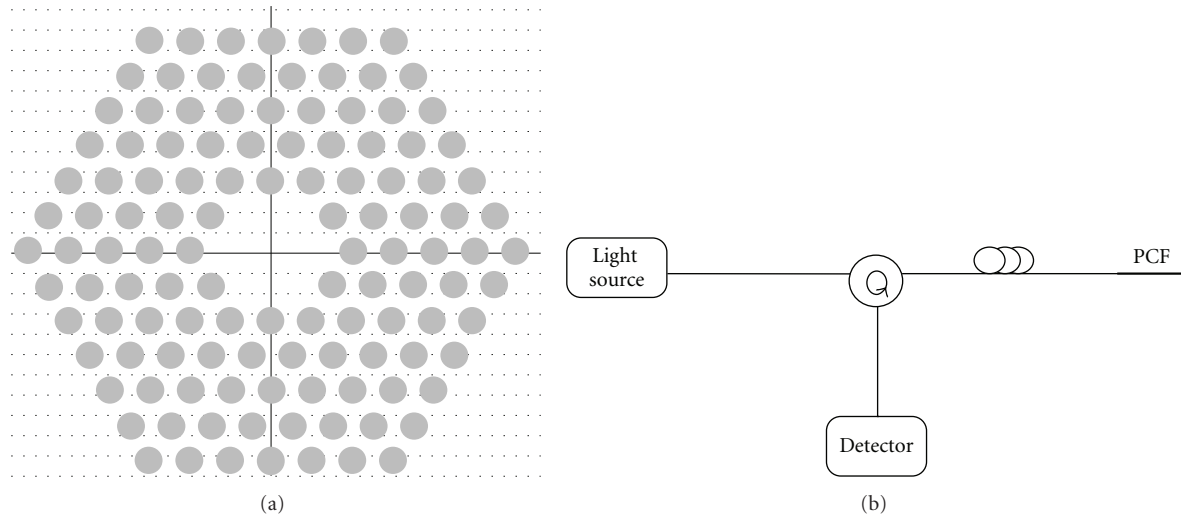


FIGURE 7: Schematic representation of (a) LMA PCF cross-section (grey: air, white: silica) and (b) in-reflection set up for refractive index measurement.

separately discriminated presenting a sensitivity of $1.3 \text{ pm}/\mu\epsilon$ and $0.3 \text{ pm}/^\circ\text{C}$ [132]. With a small-core Hi-Bi PCF-based Sagnac loop, strain and temperature can be measured with resolutions of $\pm 4.7 \mu\epsilon$ and $\pm 1.5^\circ\text{C}$, respectively [133]. A Sagnac loop using an elliptical hollow-core PBF was reported with a sensitivity of $0.81 \text{ pm}/\mu\epsilon$ to strain and of $3.97 \text{ pm}/^\circ\text{C}$ to temperature [134]. Configurations using two concatenated Sagnac interferometers were also used for temperature and strain sensing: by using a Hi-Bi PCF in one and an elliptical cladding fiber on the other Sagnac loop resolutions of $\pm 21 \mu\epsilon$ and $\pm 1.1^\circ\text{C}$ were achieved [135]; using a reference and a sensing interferometer (with a all-solid hybrid PCF) a strain sensitivity of $25.6 \text{ pm}/\mu\epsilon$ and a temperature sensitivity of $9 \text{ pm}/^\circ\text{C}$, with suppressed crosstalk $0.33 \mu\epsilon/^\circ\text{C}$, were achieved [136]. Modal interferometry was also used for temperature and strain simultaneous measurement: by connecting a piece of HC-PCF in both ends to SMFs, an interferometer with resolutions of $\pm 1.4 \mu\epsilon$ and $\pm 0.2^\circ\text{C}$ was achieved for strain and temperature, respectively [137]; another modal interferometer was constructed by making two tapers in a boron-doped Hi-Bi PCF, reaching sensitivities of $2.51 \text{ nm}/\mu\epsilon$ for strain and $16.7 \text{ pm}/^\circ\text{C}$ for temperature [138]; a modal interference-based array of sensors, using short lengths of solid core PCF spliced between SMFs, was reported showing the individual sensors sensitivities to strain and temperature of $2.2 \text{ pm}/\mu\epsilon$ and $7\text{--}9 \text{ pm}/^\circ\text{C}$ [139]. Simultaneous measurements of curvature and strain were also reported: by using a suspended multicore fiber [140] or by forming an MZI in a solid core LMA PCF with sensitivities of $3 \text{ pm}/\mu\epsilon$ to strain and $36 \text{ nm}/\text{m}$ to bending [141]. A fiber sensor was reported that could measure simultaneously pressure and strain based in a Hi-Bi PCF showing a polarimetric sensitivity of $14.8 \text{ rad}/\text{MPa}\cdot\text{m}$ to pressure and $2.8 \text{ rad}/\text{m}\cdot\mu\epsilon$ to strain [142]. Pressure and temperature are parameters that were also reported to be measured simultaneously using a twin-core fiber: by inscribing FBGs in the fiber, a linear relationship between pressure and peak shift is obtained for

2000 psi and a sensitivity to temperature of $14.9 \text{ pm}/^\circ\text{C}$ [143]; using thermally regenerated FBGs in the fiber sensitivities to pressure and temperature of $13.3 \text{ pm}/\text{psi}$ and $15.18 \text{ pm}/^\circ\text{C}$ were obtained, respectively [144]. Simultaneous measurement of load and temperature was accomplished though writing LPGs in the joint of a PCF with an SMF achieving sensitivities of $2.18 \text{ nm}/\text{N}$ and $0.086 \text{ nm}/^\circ\text{C}$, respectively [145]. An inline FP tip sensor was developed by splicing an ESM PCF between two SMFs for refractive index and temperature sensing, presenting sensitivities of $4.59/\text{RIU}$ and $4.16 \text{ nm}/^\circ\text{C}$, respectively [146]. Measurements of three parameters simultaneously have been reported. By using a solid core PCF in a specially developed spectral interferometric method temperature, strain and pressure were measured with precisions of $1.28 \times 10^{-5} \text{ K}^{-1}$, $0.4 \epsilon^{-1}$ and 10^{-5} MPa , respectively [147]. A arc-induced LPG in a PCF showed sensitivity to temperature ($\sim 6 \text{ pm}/^\circ\text{C}$), strain ($2.5 \text{ pm}/\mu\epsilon$) and bending ($12.4 \text{ nm}/\text{m}$) [148]. Using a Sagnac interferometer with a section of polarization maintaining side-hole fiber torsion, strain and temperature were measured with sensitivities of $0.06\text{--}0.08 \text{ nm}/^\circ$, $0.016\text{--}0.21 \text{ nm}/\mu\epsilon$, and $1.44\text{--}1.97 \text{ nm}/^\circ\text{C}$, respectively [149]. Using a suspended twin-core fiber an all-fiber MZI is obtained which is able to measure curvature ($1.35\text{--}1.42 \text{ nm}\cdot\text{m}$), temperature ($18.2\text{--}34.9 \text{ pm}/^\circ\text{C}$), and strain ($5\text{--}5.6 \text{ pm}/\mu\epsilon$) [150].

3.2. Bio Chemical Sensors. Optical fibers can be used for sensing of chemical and biological samples. OF-based sensors are advantageous for chemical and bio sensing due to their miniaturization, small size, flexibility, and remote capability, making fibers suitable for *in vivo* experiments, due to the fact that these waveguides are electrically passive, not representing a risk to patients, since there are no electrical connections to their body, and due to the ability for real-time measurement and the possibility to simultaneously measure several parameters. One approach for chemical/bio sensing is to provide the fiber end with a suitable indicator or a material that

responds to the parameter of interest. Chemically sensitive thin films deposited on selected areas of optical fibers can influence the propagation of light in such fibers depending on the presence or absence of chemical/biological molecules in the surrounding environment. A wide range of optical sensors has been developed for selective biomolecule detection. Most of them have reliability issues as they employ very fragile antibodies as sensing elements [151].

When compared to the conventional OFs, PCFs offer a number of unique advantages in chemical and bio sensing applications. Due to the presence of air holes running along its entire length, these fibers have a unique ability to accommodate biological and chemical samples in gaseous or liquid forms in the immediate vicinity of the fiber core or even inside the core. PCFs can be used simultaneously for light guiding and as a fluidic channel, leading to a strong light/sample overlap. Such channels can be further functionalized with biorecognition layers that can bind and progressively accumulate target biomolecules, thus enhancing sensor sensitivity and specificity. Due to PCFs core and cladding air holes small size and the high overlapping between sample and light, a very small fluid volume is required for sensing. Using PCFs the amount of volume needed is of the order of hundreds of nanoliters to tens of microliters, while in conventional optics measurement techniques the volumes needed are of order of one to ten milliliters. The use of extremely small volume is of huge interest for chemical and biomedical applications, like analytes detection or protein/DNA recognition [152, 153].

3.2.1. Gas Sensors. Many industries produce gaseous emissions as a consequence of the processes they develop. Chemical processing, glass melting, metal casting, transportation, pulp and paper, and energy production industries all produce different amount and types of gaseous emissions. As so, monitoring and control gas has become an increasingly important consideration in an ever-broader global environmental awareness context. For other industries such as chemical, bio chemical, and military ones, gas diffusion is as important parameter to analyze. Therefore, it is of enormous importance to develop gas sensing techniques that are selective, quantitative, fast acting, and not susceptible to external poisoning. To satisfy these requirements PCFs are employed, the air holes running the entire length of the fiber will act as microsized capillaries allowing gas diffusion to take place, and the whole process can be monitored, see Figure 8. PCFs are very attractive for fast, real-time detection and measurement of simple gases. Even more, PCFs technology is compatible with telecommunications systems and can easily exploit remote sensing and multiplexing.

(1) Acetylene Sensors. Different methods were reported to measure acetylene. When using solid core PCFs the most common technique is evanescent wave absorption. Some gas molecules exhibit characteristic vibrational absorption lines in the near-IR region corresponding to the transmission window of silica-based fibers and as so can be detected through the evanescent field of the guided mode. The presence of such molecules is visible in the air holes of the fiber since a loss

appears in the transmission spectrum for the characteristic wavelengths of the particular gas species. The first approach to this technique was through the use of a solid core hexagonal lattice PCF [154] and two years later through a solid core random-hole PCF using *in situ* bubble formation technique [155]; positive results were also reported using a three-hole SCF [156]; more recently, using a solid core PCF with FBGs inscribed in it presenting a sensibility of $\sim 0.017\text{--}0.022$ dB/% to acetylene concentration [157]. Acetylene sensing was also developed using HC-PCFs. Gas diffusion inside of an HC-PCF was successfully monitored by measuring the attenuation of the guided light through the fiber due to absorption of light by the gas sample [158]. Another approach made using saturation absorption spectroscopy inside of a large core HC-PCF (20 μm core) reported narrower transition and cleaner signals than when using smaller-core HC-PCFs [159]. A cell, made through filling an HC-PCF with gas and then splicing it to SMFs, containing an acetylene volume $< 5 \mu\text{L}$, was used to measure its concentration through correlation absorption spectroscopy [160]. This configuration advantage is the reduced hazard even when filled with explosive or harmful gases.

(2) Methane Sensors. Detecting methane is of special relevance in many industrial and safety applications. For gas detection, spectral sensors preferably address the strongest absorption lines. For methane, these are found in the midinfrared spectrum around 3300 nm. Despite the fact that in this wavelength region light sources and detectors are expensive methane sensing has been reported around these wavelengths [161]. Most of the authors, due to these economic inconveniences, try to work in less challenging wavelength regions. A methane sensor working at 1670 nm was developed through absorption spectroscopy for gas concentration inside of a HC-PCF, with a minimum of detection of 10 ppmv [162]. Using an HC-PCF as a gas cell for methane sensing at 1300 nm, a sensitivity of 49 ppmv-m was reported [163]. Methane sensing was also accomplished using an HC-PCF as a gas cell, targeting two different wavelength bands in the near-infrared region [164]. And, a fast response methane sensor with periodic side openings microchannels in a HC-PCF was demonstrated with a sensitivity of ~ 647 ppm [165].

(3) Multigas Sensors. Several other gases sensors have been developed, almost all based in evanescent field absorption spectroscopy. A hydrogen sensor was reported based in a tapered solid-core PCF with collapsed air holes coated with thin layers. The collapse holes allow access to the evanescent field that could be absorbed with gas-permeable thin films [166]. The detection of volatile organic compounds was demonstrated through an in-reflection PCF interferometer, without the need of any permeable material [167]. Through the measurement of gas diffusion coefficient acetylene and air were detected in a solid core PCF [168]. An all-fiber gas sensing system was developed based in an HC-PCF as a gas cell, achieving minimum concentration detectable values of 300 ppm for carbon dioxide and 5 ppm for acetylene [169]. Characterization of the absorption lines of acetylene,

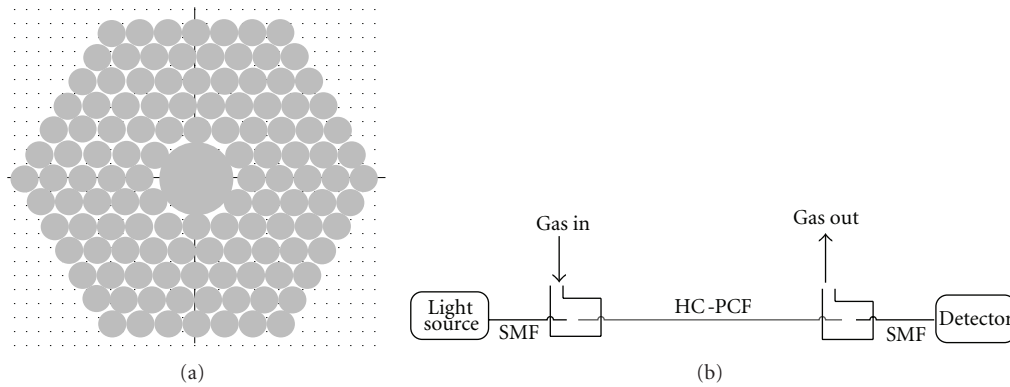


FIGURE 8: Schematic representation of (a) HC-PCF cross-section (grey: air, white: silica) and (b) configuration for gas sensing using PCFs.

hydrogen cyanide, methane, and ammonia was shown to be possible using a PBF spliced to an SMF in one end and filled with gas through the other [170]. Saturated absorption in overtone transitions of acetylene and hydrogen cyanide molecules confined in an HC-PBG was observed using input powers as low as 10 mW [171]. In another approach, spontaneous gas-phase Raman scattering using a HC-PBF as a gas cell was reported to successfully detect methane, ethane, and propane Raman signatures [172]. Even more, oxygen and nitrogen detection was performed using spontaneous Raman backscattering [173]. The implementation of a PBF-based gas sensor designed and built for practical use, occupying a small volume within preexisting equipment, was demonstrated for the detection of methane and acetylene gas [174]. Recently, an inline sensor based in two pieces of an HC-PBF with laser-drilled lateral micro-channels for gas access was reported [175], showing the ability to quantitatively measure gas mixtures. An oxygen gas sensor was also reported by forming fluorophore-doped sensing film in the array microholes of a solid core PCF, with a sensitivity of 10.8 (defined as I_0/I_{100}) and quick response time ~ 50 ms [176].

3.2.2. Molecular Sensors. A molecular sensor is based in a molecule that interacts with an analyte to produce a detectable change. Molecular sensors combine molecular recognition with some form of reporter so the presence of the guest can be observed. This kind of sensors is very important for applications such as biochemistry or biomedicine for which the detection of molecules like DNA, proteins and cancer cells are of huge importance, as it is the use of the lower sample volume possible. PCFs microstructured channels make these fibers very appropriate for such applications, given that they can be used to control the interaction between guided light and fluids located within the holes while simultaneously acting as a tiny sample chamber. Two big advantages can be obtained with these fibers: high overlapping between light and sample which is not possible with OFs or typical spectroscopy measurement techniques and the ability to perform the measurement with a very little volume sample, typically μL or less, that is much lower than in conventional spectroscopy (mL).

Rhodamine Sensors. Rhodamine belongs to the family of fluorone dyes that are often used as a tracer dye. Rhodamine dyes are used extensively in biotechnology applications such as fluorescence microscopy, flow cytometry and for the detection of analytes. This compound has well-known characteristics, and as so is one of the most used for proof-of-concept experiments, especially in molecular and fluorescence experiments. Mainly two types of techniques are used to proof detection efficiency of rhodamine: fluorescence based techniques and surface-enhanced Raman scattering. Fluorescent measurements are an invaluable tool in the study of biological systems and processes. The two most important and widely used applications of fluorescence in biomedical research are fluorescence microscopy and flow cytometry. FCFs can be used in this context for delivery of the excitation light, allowing *in vivo* fluorescence measurements by exciting the desired region, and for detection of fluorescence. A double-clad PCF was used to excite and detect the fluorescence of a rhodamine 6G dye gelatin sample, showing enhanced detection efficiency [177]. A highly sensitive gold-coated side-polished D-shaped PCF was subjected to the excitation of surface plasmon resonance technology. The plasmonic fluorescence emission of Rhodamine B using a PCF was found to be enhanced [178]. There has been significant interest in using SERS and fibers for chemical, biological, and environmental detections. The combination of both offers the advantages of the molecular specificity of Raman scattering, the big enhancement factor of SERS, and flexibility of fibers [179]. Rhodamine B detection through a four-hole SCF with gold nanoparticles serving as substrate was presented, with large interaction volume between the excitation light and the nanoparticles [180]. By filling hollow-core PCFs with aqueous solutions and using SERS, the following molecules, in a solution with the silver nanoparticles, were identified: rhodamine 6G [181]; rhodamine 6G, human insulin and tryptophan with sensitivity of 10^{-4} – 10^{-5} M [182]; rhodamine 6G with the lowest detectable concentration (10^{-10} M) [183]. A study with different PCFs (one solid core PCF and two three hole SCF) for molecular detection using SERS was reported, in which the SCF was found to be the more adequate for the purpose demonstrating a sensitivity of 10^{-10} M to

rhodamine 6 G in an aqueous solution of only $\sim 7.3 \mu\text{L}$ of volume [184].

DNA Sensors. DNA analysis techniques are usually performed by immobilizing a single strand of DNA on a glass chip and checking the hybridization of this strand to its complementary. The glass surface needs a functionalization treatment in order that the binding of biological species takes place, and hybridization is later proved through the measurement of the fluorescence signal produced by the labeled sample. Introducing PCFs instead of glass chips can lead to a significant improvement of the sensitivity, with respect to the present technology. DNA sensors based in HC-PCFs were reported: by using a highly efficient evanescent-wave detection of fluorophore-labeled biomolecule in aqueous solutions positioned in the air holes of the microstructured part of the PCF [185] or by using 16 mm long piece of functionalized HC-PCF incorporated into an optic-fluidic coupler chip towards the capture of a specific single-stranded DNA string by immobilizing a sensing layer on the microstructured internal surfaces of the fiber [186]. Using solid core PCF Bragg grating the detection of selected single-stranded DNA molecules was reported, being hybridized to a biofilm in the air holes of the PCF, measuring their interaction with the fiber modes [187]. By using LPGs in an LMA PCF and immobilizing a layer of biomolecules on the sides of the holes of the PCF, the thickness of double-stranded DNA was measured [188]. A biosensor for DNA detection based in a three-hole SCF was demonstrated, by functionalization and selective detection of DNA through hybridization of immobilized peptide nucleic acid probes [189].

Protein Sensors. Detection of specific protein entails the immobilization of antibodies for selective binding of antigens to antibodies and/or fluorescent labeling such proteins. Detection of quantum-dot-labeled proteins was reported using a soft-glass three-hole SCF and near-infrared light. The protein concentration was measured using this fluorescence capture approach, with a detection limit of 1 nM and extremely small sample volume (of order of 10 pl) [190]. The rendering of biologically active three-hole glass SCF via immobilization of antibodies within the holes of the fiber cross-section was demonstrated for detection of proteins [191]. The recognition of the proteins that bind to the antibodies is made through fluorescence labeling, opening up the possibility for measurement of multiple biomolecules via immobilization of multiple antibodies.

Other Molecular Sensors. Water molecules can be detected through their stretching vibrations-related Raman resonance. This detection was verified in the spectrum of an FWM signal of a, HC-PCF filled with water, suggesting phase-matched coherent anti-Stokes Raman scattering in inner fiber walls [192, 193]. Using Raman spectroscopy, different synthesis stages of ZnO nanoparticles inside a HC-PCF can be observed using very low pump powers [194]. Different synthesis stages can be differentiated through the Raman modes obtained using concentrations lower than

1% due to the high light/sample overlap. The detection of thiocyanate anions, with a sensitivity of $1.7 \times 10^{-7} \text{ M}$, as well as water and ethanol was demonstrated by filling the hollow-core of a PCF and measuring the trace volume using SERS and a small volume of $\sim 0.1 \mu\text{L}$ [195]. Using SERS in a solid core PCF with silver nanoparticles cluster the detection of 4-mercaptobenzoic acid was reported [196]. Evanescent-field sensing is a very used technique in molecular detection: inserting Methylene Blue in the cladding holes of a solid core PCF its absorption spectrum was measured [197] and its catalytic reactions monitored the a hollow core of a kagome PCF [198]; by filling the three-holes of a SCF, an aqueous NiCl₂ solution absorption was measured [199]; by filling the cladding holes of a solid core PCF with cobalt chloride, its concentration variations were detected through absorption spectroscopy with a sensitivity of 1.6 M^{-1} [200]. A salinity sensor was also developed using a polyimide-coated Hi-Bi PCF Sagnac interferometer based on coating-induced radial swelling [201]. This sensor achieved a salinity sensitivity of $0.742 \text{ nm}/(\text{mol/L})$, which implies 45 times more sensitivity than that of a polyimide-coated FBG.

3.2.3. Humidity and pH Sensors. Humidity measurement is required for several applications, including meteorological services, chemical and food processing industry, civil engineering, air-conditioning, horticulture and electronic processing. OFs humidity sensors offer unique advantages, such as small size and weight, immunity to electromagnetic interference, corrosion resistance and remote operation, when compared with their electronic counterparts. Most of fiber optics humidity sensors work on the basis of a hygroscopic material coated over it to modulate the light propagating through the fiber. A humidity sensor was developed through the use of an LMA PCF-based interferometer operating in reflection, without the use of any hygroscopic material, with a sensitivity of 5.6–24 pm/% RH [202].

Another parameter that is important to monitor is pH. For application fields such as medicine, environmental sciences, agriculture, food science, or biotechnology the screen of pH is an important concern. PCF as a pH-sensing probe is endowed with the advantages of being flexible, the air-hole microstructure greatly enhances the specific surface area for sensing, and given that the sensing process is carried out in the air holes microanalysis is possible. A pH sensor was demonstrated based on a pH-sensitive fluorescence dye-doped cellulose acetate thin-film modified polymer PCF [203], showing the possibility to tailor the pH response range through doping a surfactant in the sensing film.

4. Technology Development Opportunities

Photonic crystal fiber-based sensing technology is still at its youth when compared to fields such as supercontinuum generation. The first sensor developed based in a photonic crystal fiber appeared in 2000, and since then an exponential growth on the number of publications in this field was observed. The interest of the scientific community in using photonic crystal fibers as sensing elements took this research field to flare up, but not yet enough as to lead it to

commercialization. Nevertheless, the perspectives to achieve commercial availability of sensing solutions based in these fibers are optimistic. Several authors have obtained patents for sensors based in photonic crystal fibers. The area of bio chemical sensing is the one with more patents using PCFs: for the detection of adsorbates on the interior surfaces of the PCF air holes [204]; by the functionalization of the air holes in the cladding of the PCF for detection of chemical and biological agents through SERS [205]; by using half HC-PCF adjacent to a surface of an optical waveguide layer of a substrate, an analyte can be inserted in the half-core of the PCF in order to be identified by a spectroscopy interaction [206]; via taking advantage of a hollow core photonic crystal fiber as a Raman biosensor [207]; by filling the hollow core of a PCF with SERS substrate and analyte for chemical and biological detection [208, 209]; or even by producing a resonator using a solid core photonic crystal fiber coil to quantify an analyte [210, 211]. Temperature sensing with PCFs also has some patents: temperature measurement was developed by filling the fiber with a temperature-sensitive fluid [212] or accordingly with its fluorescent characteristic [213] and, even more, by using Hi-Bi PCF Sagnac loop mirrors with a partial perfusion [214] or with a PCF long-period grating differential demodulation [215]. Humidity sensors patents based on tapered and perfuse PCFs [216] and on injection-type PCFs [217] were also developed. Patents were completed for a PCF refractive index sensor based on polarization interference [218], as well as for a real-time measurement of fluid flow concentration based in a PCF [219]. An all-fiber liquid level sensor patented based in a PCF was also obtained [220], as it was a stress sensor based on a Hi-Bi PCF Sagnac loop mirror [221] and a current sensor through a photonic crystal fiber Bragg grating [222]. A hollow-core PCF was used for a Fabry-Perot interferometer in order to obtain a displacement sensor patent [223]; and a multiparameter sensor patent was completed based in a PCF [224]. In addition, patents using PCFs to construct gyroscopes were also attained: using different PCFs [225] or using a hollow-core PCF [226]. The number and content of patents based on PCFs is growing through the years, showing an open possibility for future commercial exploitation.

5. Conclusions and Final Remarks

The diversity of unusual features of photonic crystal fibers, beyond what conventional fibers can offer, leads to an increase of possibilities for new and improved sensors. There is a huge interest of the scientific community in this original technology for applications in a variety of fields. Physical sensing is the more developed area of application so far, with a vast field of published fiber sensors. There are not so many developed sensors in the bio chemical field, but progress is shown in that direction. Several more sensors are expected to be developed for applications in this area due to the noteworthy characteristics photonic crystal fibers can offer. The amount and quality of photonic crystal fiber sensors developed nowadays, and presented in this paper, show that photonic crystal fiber is a technology with an outstanding potential for sensing applications. This potential

can be further seen in the amount of existent patents of photonic crystal fiber sensors, which unlock the path for a commercial scenario.

The photonic crystal fibers sensing is a field that is growing by the day, and as so, it was not possible to mention every publication or patent or every detail of each sensor. Nevertheless, the overall assessment of photonic crystal fiber-based sensing and the possibilities offered by these fibers were presented, showing their valuable contribution to optical sensing technology.

List of Acronyms

ESM:	Endlessly single mode
FBG:	Fiber bragg grating
FP:	Fabry-Perot
FWM:	Four wave mixing
Hi-Bi:	Highly birefringent
HC:	Hollow-core
LC:	Liquid crystal
LMA:	Large-mode area
LPG:	Long-period grating
MZI:	Mach-Zehnder interferometer
MMF:	Multimode fiber
OF:	Optical fiber
PBG:	Photonic bandgap
PBF:	Photonic bandgap fiber
PCF:	Photonic crystal fiber
RIU:	Refractive index units
SCF:	Suspended-core fiber
SERS:	Surface-enhanced raman scattering
SMF:	Single mode fiber
SPR:	Surface plasmon resonance
TIR:	Total internal reflection.

Acknowledgment

The authors are grateful to the Spanish Government project TEC2010-20224-C02-01.

References

- [1] K. T. V. Grattan and T. Sun, "Fiber optic sensor technology: an overview," *Sensors and Actuators A*, vol. 82, no. 1, pp. 40–61, 2000.
- [2] P. Russell, "Applied physics: photonic crystal fibers," *Science*, vol. 299, no. 5605, pp. 358–362, 2003.
- [3] P. R. Laurent Bigot and P. Roy, "Fibres à cristal photonique: 10 ans d'existence et un vaste champ d'applications," *Images de la physique*, pp. 71–80, 2007.
- [4] S. Arismar Cerqueira, "Recent progress and novel applications of photonic crystal fibers," *Reports on Progress in Physics*, vol. 73, no. 2, Article ID 024401, 2010.
- [5] J. C. Knight, T. A. Birks, P. S. J. Russell, and D. M. Atkin, "All-silica single-mode optical fiber with photonic crystal cladding," *Optics Letters*, vol. 21, no. 19, pp. 1547–1549, 1996.
- [6] J. C. Knight, T. A. Birks, R. F. Cregan, P. S. J. Russell, and J. P. De Sandro, "Large mode area photonic crystal fibre," *Electronics Letters*, vol. 34, no. 13, pp. 1347–1348, 1998.

- [7] C. Lecaplain, B. Ortaç, G. MacHinet et al., “High-energy femtosecond photonic crystal fiber laser,” *Optics Letters*, vol. 35, no. 19, pp. 3156–3158, 2010.
- [8] D. Chen and L. Shen, “Switchable and tunable erbium-doped fiber ring laser incorporating a birefringent and highly nonlinear photonic crystal fiber,” *Laser Physics Letters*, vol. 4, no. 5, pp. 368–370, 2007.
- [9] A. M. R. Pinto, O. Frazão, J. L. Santos, and M. López-Amo, “Multiwavelength Raman fiber lasers using Hi-Bi photonic crystal fiber loop mirrors combined with random cavities,” *Journal of Lightwave Technology*, vol. 29, no. 10, Article ID 5740550, pp. 1482–1488, 2011.
- [10] G. Kakarantzas, T. A. Birks, and P. S. J. Russell, “Structural long-period gratings in photonic crystal fibers,” *Optics Letters*, vol. 27, no. 12, pp. 1013–1015, 2002.
- [11] J. M. Dudley, G. Genty, and S. Coen, “Supercontinuum generation in photonic crystal fiber,” *Reviews of Modern Physics*, vol. 78, no. 4, pp. 1135–1184, 2006.
- [12] G. Humbert, W. J. Wadsworth, S. G. Leon-Saval et al., “Supercontinuum generation system for optical coherence tomography based on tapered photonic crystal fibre,” *Optics Express*, vol. 14, no. 4, pp. 1596–1603, 2006.
- [13] R. Holzwarth, T. Udem, T. W. Hänsch, J. C. Knight, W. J. Wadsworth, and P. S. J. Russell, “Optical frequency synthesizer for precision spectroscopy,” *Physical Review Letters*, vol. 85, no. 11, pp. 2264–2267, 2000.
- [14] O. Frazão, J. L. Santos, F. M. Araújo, and L. A. Ferreira, “Optical sensing with photonic crystal fibers,” *Laser and Photonics Reviews*, vol. 2, no. 6, pp. 449–459, 2008.
- [15] P. S. J. Russell, “Photonic-crystal fibers,” *Journal of Lightwave Technology*, vol. 24, no. 12, pp. 4729–4749, 2006.
- [16] R. F. Cregan, B. J. Mangan, J. C. Knight et al., “Single-mode photonic band gap guidance of light in air,” *Science*, vol. 285, no. 5433, pp. 1537–1539, 1999.
- [17] D. G. Ouzounov, F. R. Ahmad, D. Müller et al., “Generation of megawatt optical solitons in hollow-core photonic band-gap fibers,” *Science*, vol. 301, no. 5640, pp. 1702–1704, 2003.
- [18] F. Benabid, J. C. Knight, G. Antonopoulos, and P. S. J. Russell, “Stimulated Raman scattering in hydrogen-filled hollow-core photonic crystal fiber,” *Science*, vol. 298, no. 5592, pp. 399–402, 2002.
- [19] S. Ghosh, J. E. Sharping, D. G. Ouzounov, and A. L. Gaeta, “Resonant optical interactions with molecules confined in photonic band-gap fibers,” *Physical Review Letters*, vol. 94, no. 9, Article ID 093902, 2005.
- [20] F. Benabid, J. C. Knight, and P. S. J. Russell, “Particle levitation and guidance in hollow-core photonic crystal fiber,” *Optics Express*, vol. 10, no. 21, pp. 1195–1203, 2002.
- [21] T. G. Euser, M. K. Garbos, J. S. Y. Chen, and P. S. J. Russell, “Precise balancing of viscous and radiation forces on a particle in liquid-filled photonic bandgap fiber,” *Optics Letters*, vol. 34, no. 23, pp. 3674–3676, 2009.
- [22] W. Jin, H. F. Xuan, and H. L. Ho, “Sensing with hollow-core photonic bandgap fibers,” *Measurement Science and Technology*, vol. 21, no. 9, Article ID 094014, 2010.
- [23] V. V. Tuchin, Y. S. Skibina, V. I. Beloglazov et al., “Sensor properties of hollow-core photonic crystal fibers,” *Technical Physics Letters*, vol. 34, no. 8, pp. 663–665, 2008.
- [24] J. M. Lopez-Higuera, L. Rodriguez Cobo, A. Quintela Incera, and A. Cobo, “Fiber optic sensors in structural health monitoring,” *IEEE Journal of Lightwave Technology*, vol. 29, no. 4, pp. 587–608, 2011.
- [25] H. N. Li, D. S. Li, and G. B. Song, “Recent applications of fiber optic sensors to health monitoring in civil engineering,” *Engineering Structures*, vol. 26, no. 11, pp. 1647–1657, 2004.
- [26] C. Sonnenfeld, S. Sulejmani, T. Geernaert et al., “Microstructured optical fiber sensors embedded in a laminate composite for smart material applications,” *Sensors*, vol. 11, no. 3, pp. 2566–2579, 2011.
- [27] B. Culshaw, “Fiber optics in sensing and measurement,” *IEEE Journal on Selected Topics in Quantum Electronics*, vol. 6, no. 6, pp. 1014–1021, 2000.
- [28] P. M. Blanchard, J. G. Burnett, G. R. G. Erry et al., “Two-dimensional bend sensing with a single, multi-core optical fibre,” *Smart Materials and Structures*, vol. 9, no. 2, pp. 132–140, 2000.
- [29] W. N. MacPherson, M. J. Gander, R. McBride et al., “Remotely addressed optical fibre curvature sensor using multi-core photonic crystal fibre,” *Optics Communications*, vol. 193, no. 1–6, pp. 97–104, 2001.
- [30] J. Villatoro, V. Finazzi, G. Badenes, and V. Pruneri, “Highly sensitive sensors based on photonic crystal fiber modal interferometers,” *Journal of Sensors*, vol. 2009, Article ID 747803, 2009.
- [31] O. Frazão, J. Baptista, J. L. Santos, and P. Roy, “Curvature sensor using a highly birefringent photonic crystal fiber with two asymmetric hole regions in a Sagnac interferometer,” *Applied Optics*, vol. 47, no. 13, pp. 2520–2523, 2008.
- [32] H. P. Gong, C. C. Chan, P. Zu, L. H. Chen, and X. Y. Dong, “Curvature measurement by using low-birefringence photonic crystal fiber based Sagnac loop,” *Optics Communications*, vol. 283, no. 16, pp. 3142–3144, 2010.
- [33] W. C. Wong, C. C. Chan, H. Gong, and K. C. Leong, “Mach-Zehnder photonic crystal interferometer in cavity ring-down loop for curvature measurement,” *IEEE Photonics Technology Letters*, vol. 23, no. 12, pp. 795–797, 2011.
- [34] M. Deng, C. P. Tang, T. Zhu, and Y. J. Rao, “Highly sensitive bend sensor based on Mach-Zehnder interferometer using photonic crystal fiber,” *Optics Communications*, vol. 284, no. 12, pp. 2849–2853, 2011.
- [35] B. Dong, J. Hao, and Z. Xu, “Temperature insensitive curvature measurement with a core-offset polarization maintaining photonic crystal fiber based interferometer,” *Optical Fiber Technology*, vol. 17, no. 3, pp. 233–235, 2011.
- [36] H. Dobb, K. Kalli, and D. J. Webb, “Temperature-insensitive long period grating sensors in photonic crystal fibre,” *Electronics Letters*, vol. 40, no. 11, pp. 657–658, 2004.
- [37] Z. He, Y. Zhu, and H. Du, “Effect of macro-bending on resonant wavelength and intensity of long-period gratings in photonic crystal fiber,” *Optics Express*, vol. 15, no. 4, pp. 1804–1810, 2007.
- [38] T. Allsop, K. Kalli, K. Zhou et al., “Long period gratings written into a photonic crystal fibre by a femtosecond laser as directional bend sensors,” *Optics Communications*, vol. 281, no. 20, pp. 5092–5096, 2008.
- [39] L. Jin, W. Jin, and J. Ju, “Directional bend sensing with a CO_2 long period grating in a photonic crystal fiber,” *Journal of Lightwave Technology*, vol. 27, no. 21, pp. 4884–4891, 2009.
- [40] Y. G. Han, “Temperature-insensitive strain measurement using a birefringent interferometer based on a polarization-maintaining photonic crystal fiber,” *Applied Physics B*, vol. 95, no. 2, pp. 383–387, 2009.
- [41] J. Villatoro, V. P. Minkovich, and D. Monzón-Hernández, “Temperature-independent strain sensor made from tapered holey optical fiber,” *Optics Letters*, vol. 31, no. 3, pp. 305–307, 2006.
- [42] J. Villatoro, V. P. Minkovich, and D. Monzón-Hernández, “Compact modal interferometer built with tapered microstructured optical fiber,” *IEEE Photonics Technology Letters*, vol. 18, no. 11, pp. 1258–1260, 2006.

- [43] J. Villatoro, V. Finazzi, V. P. Minkovich, V. Pruneri, and G. Badenes, "Temperature-insensitive photonic crystal fiber interferometer for absolute strain sensing," *Applied Physics Letters*, vol. 91, no. 9, Article ID 091109, 2007.
- [44] B. Dong and E. J. Hao, "Temperature-insensitive and intensity-modulated embedded photonic-crystal-fiber modal-interferometer-based microdisplacement sensor," *Journal of the Optical Society of America B*, vol. 28, no. 10, pp. 2332–2336, 2011.
- [45] Q. Shi, F. Y. Lv, Z. Wang et al., "Environmentally stable Fabry-Perot-type strain sensor based on hollow-core photonic bandgap fiber," *IEEE Photonics Technology Letters*, vol. 20, no. 4, pp. 237–239, 2008.
- [46] Q. Shi, Z. Wang, L. Jin et al., "A hollow-core photonic crystal fiber cavity based multiplexed Fabry-Perot interferometric strain sensor system," *IEEE Photonics Technology Letters*, vol. 20, no. 15, pp. 1329–1331, 2008.
- [47] O. Frazao, J. M. Baptista, and J. L. Santos, "Temperature-independent strain sensor based on a Hi-Bi photonic crystal fiber loop mirror," *IEEE Sensors Journal*, vol. 7, no. 10, pp. 1453–1455, 2007.
- [48] W. Qian, C. L. Zhao, X. Dong, and W. Jin, "Intensity measurement based temperature-independent strain sensor using a highly birefringent photonic crystal fiber loop mirror," *Optics Communications*, vol. 283, no. 24, pp. 5250–5254, 2010.
- [49] H. Zhang, B. Liu, Z. Wang et al., "Temperature-insensitive displacement sensor based on high-birefringence photonic crystal fiber loop mirror," *Optica Applicata*, vol. 40, no. 1, pp. 209–217, 2010.
- [50] M. Bravo, A. M. R. Pinto, M. Lopez-Amo, J. Kobelke, and K. Schuster, "High precision micro-displacement fiber sensor through a suspended-core Sagnac interferometer," *Optics Letters*, vol. 37, no. 2, pp. 202–204, 2012.
- [51] W. Zhou, W. C. Wong, C. C. Chan, L. Y. Shao, and X. Dong, "Highly sensitive fiber loop ringdown strain sensor using photonic crystal fiber interferometer," *Applied Optics*, vol. 50, no. 19, pp. 3087–3092, 2011.
- [52] S. Mathews, G. Farrell, and Y. Semenova, "All-fiber polarimetric electric field sensing using liquid crystal infiltrated photonic crystal fibers," *Sensors and Actuators A*, vol. 167, no. 1, pp. 54–59, 2011.
- [53] T. R. Wolinski, K. Szaniawska, S. Ertman et al., "Influence of temperature and electrical fields on propagation properties of photonic liquid-crystal fibres," *Measurement Science and Technology*, vol. 17, no. 5, pp. 985–991, 2006.
- [54] T. R. Wolinski, A. Czapla, S. Ertman et al., "Photonic liquid crystal fibers for sensing applications," *IEEE Transactions on Instrumentation and Measurement*, vol. 57, no. 8, pp. 1796–1802, 2008.
- [55] S. Mathews, G. Farrell, and Y. Semenova, "Directional electric field sensitivity of a liquid crystal infiltrated photonic crystal fiber," *IEEE Photonics Technology Letters*, vol. 23, no. 7, pp. 408–410, 2011.
- [56] S. Mathews, G. Farrell, and Y. Semenova, "Liquid crystal infiltrated photonic crystal fibers for electric field intensity measurements," *Applied Optics*, vol. 50, no. 17, pp. 2628–2635, 2011.
- [57] A. Michie, J. Canning, I. Bassett et al., "Spun elliptically birefringent photonic crystal fibre for current sensing," *Measurement Science and Technology*, vol. 18, no. 10, pp. 3070–3074, 2007.
- [58] Y. K. Chamorovskiy, N. I. Starostin, M. V. Ryabko et al., "Miniature microstructured fiber coil with high magneto-optical sensitivity," *Optics Communications*, vol. 282, no. 23, pp. 4618–4621, 2009.
- [59] H. V. Thakur, S. M. Nalawade, S. Gupta, R. Kitture, and S. N. Kale, "Photonic crystal fiber injected with Fe₃O₄ nanofluid for magnetic field detection," *Applied Physics Letters*, vol. 99, Article ID 161101, 3 pages, 2011.
- [60] S. M. M. Quintero, C. Martelli, A. M. B. Braga, L. C. G. Valente, and C. C. Kato, "Magnetic field measurements based on terfenol coated photonic crystal fibers," *Sensors*, vol. 11, no. 12, pp. 11103–11111, 2011.
- [61] Y. Zhao, R. Q. Lv, Y. Ying, and Q. Wang, "Hollow-core photonic crystal fiber Fabry-Perot sensor for magnetic field measurement based on magnetic fluid," *Optics and Laser Technology*, vol. 44, pp. 899–902, 2012.
- [62] W. J. Bock, J. Chen, P. Mikulic, T. Eftimov, and M. Korwin-Pawlowski, "Pressure sensing using periodically tapered long-period gratings written in photonic crystal fibres," *Measurement Science and Technology*, vol. 18, no. 10, pp. 3098–3102, 2007.
- [63] W. J. Bock, J. Chen, T. Eftimov, and W. Urbanczyk, "A photonic crystal fiber sensor for pressure measurements," *IEEE Transactions on Instrumentation and Measurement*, vol. 55, no. 4, pp. 1119–1123, 2006.
- [64] H. K. Gahir and D. Khanna, "Design and development of a temperature-compensated fiber optic polarimetric pressure sensor based on photonic crystal fiber at 1550 nm," *Applied Optics*, vol. 46, no. 8, pp. 1184–1189, 2007.
- [65] F. C. Fávero, S. M. M. Quintero, C. Martelli et al., "Hydrostatic pressure sensing with high birefringence photonic crystal fibers," *Sensors*, vol. 10, no. 11, pp. 9698–9711, 2010.
- [66] Y. S. Shinde and H. K. Gahir, "Dynamic pressure sensing study using photonic crystal fiber: application to tsunami sensing," *IEEE Photonics Technology Letters*, vol. 20, no. 4, pp. 279–281, 2008.
- [67] T. Nasilowski, T. Martynkien, G. Statkiewicz et al., "Temperature and pressure sensitivities of the highly birefringent photonic crystal fiber with core asymmetry," *Applied Physics B*, vol. 81, no. 2-3, pp. 325–331, 2005.
- [68] T. Martynkien, M. Szpulak, G. Statkiewicz et al., "Measurements of sensitivity to hydrostatic pressure and temperature in highly birefringent photonic crystal fibers," *Optical and Quantum Electronics*, vol. 39, no. 4–6, pp. 481–489, 2007.
- [69] T. Martynkien, G. Statkiewicz-Barabach, J. Olszewski et al., "Highly birefringent microstructured fibers with enhanced sensitivity to hydrostatic pressure," *Optics Express*, vol. 18, no. 14, pp. 15113–15121, 2010.
- [70] H. Y. Fu, H. Y. Tam, L. Y. Shao et al., "Pressure sensor realized with polarization-maintaining photonic crystal fiber-based Sagnac interferometer," *Applied Optics*, vol. 47, no. 15, pp. 2835–2839, 2008.
- [71] H. Y. Fu, C. Wu, M. L. V. Tse et al., "High pressure sensor based on photonic crystal fiber for downhole application," *Applied Optics*, vol. 49, no. 14, pp. 2639–2643, 2010.
- [72] S. H. Aref, M. I. Zibaii, M. Kheiri et al., "Pressure and temperature characterization of two interferometric configurations based on suspended-core fibers," *Optics Communications*, vol. 285, no. 3, pp. 269–273, 2012.
- [73] T. Martynkien, M. Szpulak, and W. Urbanczyk, "Modeling and measurement of temperature sensitivity in birefringent photonic crystal holey fibers," *Applied Optics*, vol. 44, no. 36, pp. 7780–7788, 2005.

- [74] J. Ju, Z. Wang, W. Jin, and M. S. Demokan, "Temperature sensitivity of a two-mode photonic crystal fiber interferometric sensor," *IEEE Photonics Technology Letters*, vol. 18, no. 20, pp. 2168–2170, 2006.
- [75] D. Monzon-Hernandez, V. P. Minkovich, and J. Villatoro, "High-temperature sensing with tapers made of microstructured optical fiber," *IEEE Photonics Technology Letters*, vol. 18, no. 3, pp. 511–513, 2006.
- [76] S. S. Li, Z. D. Huang, X. S. Song et al., "Photonic crystal fibre based high temperature sensor with three-beam path interference," *Electronics Letters*, vol. 46, no. 20, pp. 1394–1396, 2010.
- [77] S. M. Nalawade and H. V. Thakur, "Photonic crystal fiber strain-independent temperature sensing based on modal interferometer," *IEEE Photonics Technology Letters*, vol. 23, no. 21, pp. 1600–1602, 2011.
- [78] J. Ju, W. Jin, and H. L. Ho, "Compact in-fiber interferometer formed by long-period gratings in photonic crystal fiber," *IEEE Photonics Technology Letters*, vol. 20, no. 23, pp. 1899–1901, 2008.
- [79] Y. Geng, X. Li, X. Tan, Y. Deng, and Y. Yu, "Sensitivity-enhanced high-temperature sensing using all-solid photonic bandgap fiber modal interference," *Applied Optics*, vol. 50, no. 4, pp. 468–472, 2011.
- [80] H. Y. Choi, K. S. Pack, S. J. Park, U. C. Paek, B. H. Lee, and E. S. Choi, "Miniature fiber-optic high temperature sensor based on a hybrid structured Fabry-Perot interferometer," *Optics Letters*, vol. 33, no. 21, pp. 2455–2457, 2008.
- [81] A. M. R. Pinto, O. Frazão, J. L. Santos, M. Lopez-Amo, J. Kobelke, and K. Schuster, "Interrogation of a suspended-core Fabry-Perot temperature sensor through a dual wavelength Raman fiber laser," *Journal of Lightwave Technology*, vol. 28, no. 21, Article ID 5582123, pp. 3149–3155, 2010.
- [82] A. M. R. Pinto, M. Lopez-Amo, J. Kobelke, and K. Schuster, "Temperature fiber laser sensor based on a hybrid cavity and a random mirror," *IEEE Journal of Lightwave Technology*, no. 99, 2011.
- [83] Y. Zhu, P. Shum, H. W. Bay et al., "Strain-insensitive and high-temperature long-period gratings inscribed in photonic crystal fiber," *Optics Letters*, vol. 30, no. 4, pp. 367–369, 2005.
- [84] B. H. Kim, S. H. Lee, A. Lin, C. L. Lee, J. Lee, and W. T. Han, "Large temperature sensitivity of Sagnac loop interferometer based on the birefringent holey fiber filled with metal indium," *Optics Express*, vol. 17, no. 3, pp. 1789–1794, 2009.
- [85] W. Qian, C. L. Zhao, S. He et al., "High-sensitivity temperature sensor based on an alcohol-filled photonic crystal fiber loop mirror," *Optics Letters*, vol. 36, no. 9, pp. 1548–1550, 2011.
- [86] B. Larrion, M. Hernandez, F. J. Arregui, J. Goicoechea, J. Bravo, and I. R. Matias, "Photonic crystal fiber temperature sensor based on quantum dot nanocoatings," *Journal of Sensors*, vol. 2009, Article ID 932471, 6 pages, 2009.
- [87] A. Bozolan, R. M. Gerosa, C. J. S. de Matos, and M. A. Romero, "Temperature sensing using colloidal-core photonic crystal fiber," *IEEE Sensors Journal*, vol. 12, no. 1, pp. 195–200, 2012.
- [88] Y. Miao, B. Liu, K. Zhang, Y. Liu, and H. Zhang, "Temperature tunability of photonic crystal fiber filled with Fe_3O_4 nanoparticle fluid," *Applied Physics Letters*, vol. 98, no. 2, Article ID 021103, 2011.
- [89] Y. Yu, X. Li, X. Hong et al., "Some features of the photonic crystal fiber temperature sensor with liquid ethanol filling," *Optics Express*, vol. 18, no. 15, pp. 15383–15388, 2010.
- [90] W. Ying, Y. Minwei, D. N. Wang, and C. R. Liao, "Selectively infiltrated photonic crystal fiber with ultrahigh temperature sensitivity," *IEEE Photonics Technology Letters*, vol. 23, no. 20, pp. 1520–1522, 2011.
- [91] L. Zou, X. Bao, and L. Chen, "Distributed Brillouin temperature sensing in photonic crystal fiber," *Smart Materials and Structures*, vol. 14, no. 3, pp. S8–S11, 2005.
- [92] Y. Dong, X. Bao, and L. Chen, "Distributed temperature sensing based on birefringence effect on transient Brillouin grating in a polarization-maintaining photonic crystal fiber," *Optics Letters*, vol. 34, no. 17, pp. 2590–2592, 2009.
- [93] H. Y. Fu, S. K. Khijwania, H. Y. Tam, P. K. A. Wai, and C. Lu, "Polarization-maintaining photonic-crystal-fiber-based all-optical polarimetric torsion sensor," *Applied Optics*, vol. 49, no. 31, pp. 5954–5958, 2010.
- [94] O. Frazao, C. Jesus, J. M. Baptista, J. L. Santos, and P. Roy, "Fiber-optic interferometric torsion sensor based on a two-lp-mode operation in birefringent fiber," *IEEE Photonics Technology Letters*, vol. 21, no. 17, pp. 1277–1279, 2009.
- [95] H. M. Kim, T. H. Kim, B. Kim, and Y. Chung, "Temperature-insensitive torsion sensor with enhanced sensitivity by use of a highly birefringent photonic crystal fiber," *IEEE Photonics Technology Letters*, vol. 22, no. 20, pp. 1539–1541, 2010.
- [96] W. G. Chen, S. Q. Lou, L. W. Wang, H. Zou, W. L. Lu, and S. S. Jian, "Highly sensitive torsion sensor based on Sagnac interferometer using side-leakage photonic crystal fiber," *IEEE Photonics Technology Letters*, vol. 23, no. 21, pp. 1639–1641, 2011.
- [97] P. Zu, C. C. Chan, Y. Jin et al., "A temperature-insensitive twist sensor by using low-birefringence photonic-crystal-fiber-based Sagnac interferometer," *IEEE Photonics Technology Letters*, vol. 23, no. 13, pp. 920–922, 2011.
- [98] X. Yu, P. Shum, S. Fu, and L. Deng, "Torsion-sensitivity of mechanical long-period grating in photonic crystal fiber," *Journal of Optoelectronics and Advanced Materials*, vol. 8, no. 3, pp. 1247–1249, 2006.
- [99] D. E. Ceballos-Herrera, I. Torres-Gomez, A. Martinez-Rios, L. Garcia, and J. J. Sanchez-Mondragon, "Torsion sensing characteristics of mechanically induced long-period holey fiber gratings," *IEEE Sensors Journal*, vol. 10, no. 7, pp. 1200–1205, 2010.
- [100] H. M. Kim, T. H. Kim, B. Kim, and Y. Chung, "Enhanced transverse load sensitivity by using a highly birefringent photonic crystal fiber with larger air holes on one axis," *Applied Optics*, vol. 49, no. 20, pp. 3841–3845, 2010.
- [101] C. Jewart, K. P. Chen, B. McMillen et al., "Sensitivity enhancement of fiber bragg gratings to transverse stress by using microstructural fibers," *Optics Letters*, vol. 31, no. 15, pp. 2260–2262, 2006.
- [102] T. Geernaert, G. Luyckx, E. Voet et al., "Transversal load sensing with fiber bragg gratings in microstructured optical fibers," *IEEE Photonics Technology Letters*, vol. 21, no. 1, pp. 6–8, 2009.
- [103] Y. Wang, H. Bartelt, W. Ecke et al., "Investigating transverse loading characteristics of microstructured fiber bragg gratings with an active fiber depolarizer," *IEEE Photonics Technology Letters*, vol. 21, no. 19, pp. 1450–1452, 2009.
- [104] C. M. Jewart, T. Chen, E. Lindner et al., "Suspended-core fiber bragg grating sensor for directional-dependent transverse stress monitoring," *Optics Letters*, vol. 36, no. 12, pp. 2360–2362, 2011.
- [105] C. F. Fan, C. L. Chiang, and C. P. Yu, "Birefringent photonic crystal fiber coils and their application to transverse

- displacement sensing,” *Optics Express*, vol. 19, no. 21, pp. 19948–19954, 2011.
- [106] P. Zu, C. C. Chan, Y. Jin, Y. Zhang, and X. Dong, “Fabrication of a temperature-insensitive transverse mechanical load sensor by using a photonic crystal fiber-based Sagnac loop,” *Measurement Science and Technology*, vol. 22, no. 2, Article ID 025204, 2011.
- [107] M. C. P. Huy, G. Laffont, V. Dewynter et al., “Three-hole microstructured optical fiber for efficient fiber bragg grating refractometer,” *Optics Letters*, vol. 32, no. 16, pp. 2390–2392, 2007.
- [108] C. Martelli, J. Canning, M. Kristensen, and N. Grothoff, “Refractive index measurement within a photonic crystal fibre based on short wavelength diffraction,” *Sensors*, vol. 7, no. 11, pp. 2492–2498, 2007.
- [109] Y. Zhu, Z. He, and H. Du, “Detection of external refractive index change with high sensitivity using long-period gratings in photonic crystal fiber,” *Sensors and Actuators B*, vol. 131, no. 1, pp. 265–269, 2008.
- [110] Z. He, F. Tian, Y. Zhu, N. Lavlinskaia, and H. Du, “Long-period gratings in photonic crystal fiber as an optofluidic label-free biosensor,” *Biosensors and Bioelectronics*, vol. 26, no. 12, pp. 4774–4778, 2011.
- [111] Z. He, Y. Zhu, and H. Du, “Long-period gratings inscribed in air- and water-filled photonic crystal fiber for refractometric sensing of aqueous solution,” *Applied Physics Letters*, vol. 92, no. 4, Article ID 044105, 2008.
- [112] L. Rindorf and O. Bang, “Highly sensitive refractometer with a photonic-crystal-fiber long-period grating,” *Optics Letters*, vol. 33, no. 6, pp. 563–565, 2008.
- [113] V. P. Minkovich, J. Villatoro, D. Monzón-Hernández, S. Calixto, A. B. Sotsky, and L. I. Sotskaya, “Holey fiber tapers with resonance transmission for high-resolution refractive index sensing,” *Optics Express*, vol. 13, no. 19, pp. 7609–7614, 2005.
- [114] D. Monzon-Hernandez, V. P. Minkovich, J. Villatoro, M. P. Kreuzer, and G. Badenes, “Photonic crystal fiber microtaper supporting two selective higher-order modes with high sensitivity to gas molecules,” *Applied Physics Letters*, vol. 93, Article ID 081106, 3 pages, 2008.
- [115] R. Jha, J. Villatoro, and G. Badenes, “Ultrastable in reflection photonic crystal fiber modal interferometer for accurate refractive index sensing,” *Applied Physics Letters*, vol. 93, no. 19, Article ID 191106, 2008.
- [116] D. K. C. Wu, B. T. Kuhlmeier, and B. J. Eggleton, “Ultrasensitive photonic crystal fiber refractive index sensor,” *Optics Letters*, vol. 34, no. 3, pp. 322–324, 2009.
- [117] R. Jha, J. Villatoro, G. Badenes, and V. Pruneri, “Refractometry based on a photonic crystal fiber interferometer,” *Optics Letters*, vol. 34, no. 5, pp. 617–619, 2009.
- [118] S. Silva, J. L. Santos, F. X. Malcata, J. Kobelke, K. Schuster, and O. Frazao, “Optical refractometer based on large-core air-clad photonic crystal fibers,” *Optics Letters*, vol. 36, no. 6, pp. 852–854, 2011.
- [119] M. Smietana, D. Brabant, W. Bock, P. Mikulic, and T. Eftimov, “Refractive-index sensing with Inline core-cladding intermodal interferometer based on silicon nitride nano-coated photonic crystal fiber,” *IEEE Journal of Lightwave Technology*, vol. 99, 2011.
- [120] W. C. Wong, W. Zhou, C. C. Chan, X. Dong, and K. C. Leong, “Cavity ringdown refractive index sensor using photonic crystal fiber interferometer,” *Sensors and Actuators B*, vol. 161, no. 1, pp. 108–113, 2011.
- [121] M. H. Frosz, A. Stefani, and O. Bang, “Highly sensitive and simple method for refractive index sensing of liquids in microstructured optical fibers using four-wave mixing,” *Optics Express*, vol. 19, no. 11, pp. 10471–10484, 2011.
- [122] J. Sun and C. C. Chan, “Photonic bandgap fiber for refractive index measurement,” *Sensors and Actuators B*, vol. 128, no. 1, pp. 46–50, 2007.
- [123] X. Yu, P. Shum, G. B. Ren, and N. Q. Ngo, “Photonic crystal fibers with high index infiltrations for refractive index sensing,” *Optics Communications*, vol. 281, no. 18, pp. 4555–4559, 2008.
- [124] H. V. Thakur, S. M. Nalawade, Y. Saxena, and K. T. V. Grattan, “All-fiber embedded pm-pcf vibration sensor for structural health monitoring of composite,” *Sensors and Actuators A*, vol. 167, no. 2, pp. 204–212, 2011.
- [125] G. Rajan, M. Ramakrishnan, Y. Semenova et al., “Analysis of Vibration Measurements in a Composite Material Using an Embedded PM-PCF Polarimetric Sensor and an FBG Sensor,” *IEEE Sensors Journal*, vol. 99, 2011.
- [126] L. Zou, X. Bao, V. Shahraam Afshar, and L. Chen, “Dependence of the Brillouin frequency shift on strain and temperature in a photonic crystal fiber,” *Optics Letters*, vol. 29, no. 13, pp. 1485–1487, 2004.
- [127] Y. G. Han, Y. Chung, S. B. Lee, C. S. Kim, M. Y. Jeong, and M. K. Kim, “Temperature and strain discrimination based on a temperature-insensitive birefringent interferometer incorporating an erbium-doped fiber,” *Applied Optics*, vol. 48, no. 12, pp. 2303–2307, 2009.
- [128] C. Martelli, J. Canning, N. Grothoff, and K. Lyytikainen, “Strain and temperature characterization of photonic crystal fiber bragg gratings,” *Optics Letters*, vol. 30, no. 14, pp. 1785–1787, 2005.
- [129] O. Frazao, S. H. Aref, J. M. Baptista et al., “Fabry-Perot cavity based on a suspended-core fiber for strain and temperature measurement,” *IEEE Photonics Technology Letters*, vol. 21, no. 17, pp. 1229–1231, 2009.
- [130] Y. J. Rao, M. Deng, T. Zhu, and H. Li, “In-line Fabry-Perot etalons based on hollow-core photonic bandgap fibers for high-temperature applications,” *Journal of Lightwave Technology*, vol. 27, no. 19, pp. 4360–4365, 2009.
- [131] O. Frazão, J. M. Baptista, J. L. Santos, J. Kobelke, and K. Schuster, “Strain and temperature characterisation of sensing head based on suspended-core fibre in Sagnac interferometer,” *Electronics Letters*, vol. 44, no. 25, pp. 1455–1456, 2008.
- [132] Y. G. Han, Y. Chung, and S. B. Lee, “Discrimination of strain and temperature based on a polarization-maintaining photonic crystal fiber incorporating an erbium-doped fiber,” *Optics Communications*, vol. 282, no. 11, pp. 2161–2164, 2009.
- [133] R. M. Andre, M. B. Marques, P. Roy, and O. Frazao, “Fiber loop mirror using a small core microstructured fiber for strain and temperature discrimination,” *IEEE Photonics Technology Letters*, vol. 22, no. 15, pp. 1120–1122, 2010.
- [134] G. Kim, T. Cho, K. Hwang et al., “Strain and temperature sensitivities of an elliptical hollow-core photonic bandgap fiber based on Sagnac interferometer,” *Optics Express*, vol. 17, no. 4, pp. 2481–2486, 2009.
- [135] O. Frazao, J. L. Santos, and J. M. Baptista, “Strain and temperature discrimination using IF concatenated high-birefringence fiber loop mirrors,” *IEEE Photonics Technology Letters*, vol. 19, pp. 1260–1262, 2007.
- [136] B. Gu, W. Yuan, S. He, and O. Bang, “Temperature compensated strain sensor based on cascaded Sagnac interferometers

- and all-solid birefringent hybrid photonic crystal fibers," *IEEE Sensors Journal*, no. 99, 2011.
- [137] S. H. Aref, R. Amezcua-Correa, J. P. Carvalho et al., "Modal interferometer based on hollow-core photonic crystal fiber for strain and temperature measurement," *Optics Express*, vol. 17, no. 21, pp. 18669–18675, 2009.
- [138] G. Statkiewicz-Barabach, J. P. Carvalho, O. Frazão et al., "Intermodal interferometer for strain and temperature sensing fabricated in birefringent boron doped microstructured fiber," *Applied Optics*, vol. 50, no. 21, pp. 3742–3749, 2011.
- [139] G. A. Cardenas-Sevilla, V. Finazzi, J. Villatoro, and V. Pruneri, "Photonic crystal fiber sensor array based on modes overlapping," *Optics Express*, vol. 19, no. 8, pp. 7596–7602, 2011.
- [140] R. M. Silva, M. S. Ferreira, J. Kobelke, K. Schuster, and O. Frazao, "Simultaneous measurement of curvature and strain using a suspended multicore fiber," *Optics Letters*, vol. 36, no. 19, pp. 3939–3941, 2011.
- [141] W. Shin, Y. L. Lee, B. A. Yu, Y. C. Noh, and T. J. Ahn, "Highly sensitive strain and bending sensor based on in-line fiber Mach-Zehnder interferometer in solid core large mode area photonic crystal fiber," *Optics Communications*, vol. 283, no. 10, pp. 2097–2101, 2010.
- [142] G. Statkiewicz, T. Martynkien, and W. Urbanczyk, "Measurements of modal birefringence and polarimetric sensitivity of the birefringent holey fiber to hydrostatic pressure and strain," *Optics Communications*, vol. 241, no. 4–6, pp. 339–348, 2004.
- [143] C. M. Jewart, Q. Wang, J. Canning, D. Grobncic, S. J. Mihailov, and K. P. Chen, "Ultrafast femtosecond-laser-induced fiber bragg gratings in air-hole microstructured fibers for high-temperature pressure sensing," *Optics Letters*, vol. 35, no. 9, pp. 1443–1445, 2010.
- [144] T. Chen, R. Z. Chen, C. Jewart et al., "Regenerated gratings in air-hole microstructured fibers for high-temperature pressure sensing," *Optics Letters*, vol. 36, no. 18, pp. 3542–3544, 2011.
- [145] J. Xu, Y. G. Liu, Z. Wang, and B. Tai, "Simultaneous force and temperature measurement using long-period grating written on the joint of a microstructured optical fiber and a single mode fiber," *Applied Optics*, vol. 49, no. 3, pp. 492–496, 2010.
- [146] Y. J. Rao, M. Deng, D. W. Duan, and T. Zhu, "In-line fiber Fabry-Perot refractive-index tip sensor based on endlessly photonic crystal fiber," *Sensors and Actuators A*, vol. 148, no. 1, pp. 33–38, 2008.
- [147] W. J. Bock, W. Urbanczyk, and J. Wojcik, "Measurements of sensitivity of the single-mode photonic crystal holey fibre to temperature, elongation and hydrostatic pressure," *Measurement Science and Technology*, vol. 15, no. 8, pp. 1496–1500, 2004.
- [148] H. Dobb, K. Kalli, and D. J. Webb, "Measured sensitivity of arc-induced long-period grating sensors in photonic crystal fibre," *Optics Communications*, vol. 260, no. 1, pp. 184–191, 2006.
- [149] O. Frazão, S. O. Silva, J. M. Baptista et al., "Simultaneous measurement of multiparameters using a Sagnac interferometer with polarization maintaining side-hole fiber," *Applied Optics*, vol. 47, no. 27, pp. 4841–4848, 2008.
- [150] S. F. O. Silva, J. L. Santos, J. Kobelke, K. Schuster, and O. Frazao, "Simultaneous measurement of three parameters using an all-fiber Mach-Zehnder interferometer based on suspended twin-core fibers," *Optical Engineering*, vol. 50, Article ID 030501, 2011.
- [151] O. S. Wolfbeis, "Fibre-optic sensors in biomedical sciences," *Pure and Applied Chemistry*, vol. 59, no. 5, pp. 663–672, 1987.
- [152] M. Skorobogatiy, "Microstructured and photonic bandgap fibers for applications in the resonant bio- and chemical sensors," *Journal of Sensors*, vol. 2009, Article ID 524237, 2009.
- [153] T. M. Monro, S. Warren-Smith, E. P. Schartner et al., "Sensing with suspended-core optical fibers," *Optical Fiber Technology*, vol. 16, no. 6, pp. 343–356, 2010.
- [154] Y. L. Hoo, W. Jin, H. L. Ho, D. N. Wang, and R. S. Windeler, "Evanescent-wave gas sensing using microstructure fiber," *Optical Engineering*, vol. 41, no. 1, pp. 8–9, 2002.
- [155] G. Pickrell, W. Peng, and A. Wang, "Random-hole optical fiber evanescent-wave gas sensing," *Optics Letters*, vol. 29, no. 13, pp. 1476–1478, 2004.
- [156] A. S. Webb, F. Poletti, D. J. Richardson, and J. K. Sahu, "Suspended-core holey fiber for evanescent-field sensing," *Optical Engineering*, vol. 46, no. 1, Article ID 010503, 2007.
- [157] G. F. Yan, A. P. Zhang, G. Y. Ma et al., "Fiber-optic acetylene gas sensor based on microstructured optical fiber bragg gratings," *IEEE Photonics Technology Letters*, vol. 23, no. 21, pp. 1588–1590, 2011.
- [158] Y. L. Hoo, W. Jin, H. L. Ho, J. Ju, and D. N. Wang, "Gas diffusion measurement using hollow-core photonic bandgap fiber," *Sensors and Actuators B*, vol. 105, no. 2, pp. 183–186, 2005.
- [159] R. Thapa, K. Knabe, M. Faheem, A. Naweed, O. L. Weaver, and K. L. Corwin, "Saturated absorption spectroscopy of acetylene gas inside large-core photonic bandgap fiber," *Optics Letters*, vol. 31, no. 16, pp. 2489–2491, 2006.
- [160] E. Austin, A. van Brakel, M. N. Petrovich, and D. J. Richardson, "Fibre optical sensor for c_2h_2 gas using gas-filled photonic bandgap fibre reference cell," *Sensors and Actuators B*, vol. 139, no. 1, pp. 30–34, 2009.
- [161] L. Kornaszewski, N. Gayraud, J. M. Stone et al., "Mid-infrared methane detection in a photonic bandgap fiber using a broadband optical parametric oscillator," *Optics Express*, vol. 15, no. 18, pp. 11219–11224, 2007.
- [162] A. M. Cubillas, M. Silva-Lopez, J. M. Lazaro, O. M. Conde, M. N. Petrovich, and J. M. Lopez-Higuera, "Methane detection at 1670-nm band using a hollow-core photonic bandgap fiber and a multiline algorithm," *Optics Express*, vol. 15, no. 26, pp. 17570–17576, 2007.
- [163] A. M. Cubillas, J. M. Lazaro, M. Silva-Lopez, O. M. Conde, M. N. Petrovich, and J. M. Lopez-Higuera, "Methane sensing at 1300 nm band with hollow-core photonic bandgap fibre as gas cell," *Electronics Letters*, vol. 44, no. 6, pp. 403–405, 2008.
- [164] A. M. Cubillas, J. M. Lazaro, O. M. Conde, M. N. Petrovich, and J. M. Lopez-Higuera, "Gas sensor based on photonic crystal fibres in the $2\nu_3$ and $\nu_2 + \nu_3$ vibrational bands of methane," *Sensors*, vol. 9, no. 8, pp. 6261–6272, 2009.
- [165] Y. L. Hoo, S. Liu, H. L. Ho, and W. Jin, "Fast response microstructured optical fiber methane sensor with multiple side-openings," *IEEE Photonics Technology Letters*, vol. 22, no. 5, pp. 296–298, 2010.
- [166] V. P. Minkovich, D. Monzón-Hernández, J. Villatoro, and G. Badenes, "Microstructured optical fiber coated with thin films for gas and chemical sensing," *Optics Express*, vol. 14, no. 18, pp. 8413–8418, 2006.
- [167] J. Villatoro, M. P. Kreuzer, R. Jha et al., "Photonic crystal fiber interferometer for chemical vapor detection with high sensitivity," *Optics Express*, vol. 17, no. 3, pp. 1447–1453, 2009.
- [168] Y. L. Hoo, W. Jin, H. L. Ho, and D. N. Wang, "Measurement of gas diffusion coefficient using photonic crystal fiber," *IEEE Photonics Technology Letters*, vol. 15, no. 10, pp. 1434–1436, 2003.

- [169] H. Ding, X. Li, J. Cui, S. Dong, and L. Yang, "An all-fiber gas sensing system using hollow-core photonic bandgap fiber as gas cell," *Instrumentation Science and Technology*, vol. 39, no. 1, pp. 78–87, 2011.
- [170] T. Ritari, J. Tuominen, H. Ludvigsen et al., "Gas sensing using air-guiding photonic bandgap fibers," *Optics Express*, vol. 12, no. 17, pp. 4080–4087, 2004.
- [171] J. Henningsen, J. Hald, and J. C. Petersen, "Saturated absorption in acetylene and hydrogen cyanide in hollow-core photonic bandgap fibers," *Optics Express*, vol. 13, no. 26, pp. 10475–10482, 2005.
- [172] M. P. Buric, K. P. Chen, J. Falk, and S. D. Woodruff, "Enhanced spontaneous Raman scattering and gas composition analysis using a photonic crystal fiber," *Applied Optics*, vol. 47, no. 23, pp. 4255–4261, 2008.
- [173] M. P. Buric, K. P. Chen, J. Falk, and S. D. Woodruff, "Improved sensitivity gas detection by spontaneous Raman scattering," *Applied Optics*, vol. 48, no. 22, pp. 4424–4429, 2009.
- [174] J. P. Parry, B. C. Griffiths, N. Gayraud et al., "Towards practical gas sensing with micro-structured fibres," *Measurement Science and Technology*, vol. 20, no. 7, Article ID 075301, 2009.
- [175] H. Lehmann, H. Bartelt, R. Willsch, R. Amezcua-Correa, and J. C. Knight, "In-line gas sensor based on a photonic bandgap fiber with laser-drilled lateral microchannels," *IEEE Sensors Journal*, vol. 11, no. 11, pp. 2926–2931, 2011.
- [176] X. Yang, L. Peng, L. Yuan et al., "Oxygen gas optrode based on microstructured polymer optical fiber segment," *Optics Communications*, vol. 284, no. 13, pp. 3462–3466, 2011.
- [177] M. T. Myaing, J. Y. Ye, T. B. Norris et al., "Enhanced two-photon biosensing with double-clad photonic crystal fibers," *Optics Letters*, vol. 28, no. 14, pp. 1224–1226, 2003.
- [178] X. Yu, D. Yong, H. Zhang et al., "Plasmonic enhanced fluorescence spectroscopy using side-polished microstructured optical fiber," *Sensors and Actuators B*, vol. 160, no. 1, pp. 196–201, 2011.
- [179] H. Yan, C. Gu, C. Yang et al., "Hollow core photonic crystal fiber surface-enhanced Raman probe," *Applied Physics Letters*, vol. 89, no. 20, Article ID 204101, 2006.
- [180] H. Yan, J. Liu, C. Yang, G. Jin, C. Gu, and L. Hou, "Novel index-guided photonic crystal fiber surface-enhanced Raman scattering probe," *Optics Express*, vol. 16, no. 11, pp. 8300–8305, 2008.
- [181] F. M. Cox, A. Argyros, M. C. J. Large, and S. Kalluri, "Surface enhanced Raman scattering in a hollow core microstructured optical fiber," *Optics Express*, vol. 15, no. 21, pp. 13675–13681, 2007.
- [182] Y. Zhang, C. Shi, C. Gu, L. Seballos, and J. Z. Zhang, "Liquid core photonic crystal fiber sensor based on surface enhanced Raman scattering," *Applied Physics Letters*, vol. 90, no. 19, Article ID 193504, 2007.
- [183] X. Yang, C. Shi, D. Wheeler et al., "High-sensitivity molecular sensing using hollow-core photonic crystal fiber and surface-enhanced Raman scattering," *Journal of the Optical Society of America A*, vol. 27, no. 5, pp. 977–984, 2010.
- [184] M. K. Khaing Oo, Y. Han, J. Kanka, S. Sukhishvili, and H. Du, "Structure fits the purpose: photonic crystal fibers for evanescent-field surface-enhanced Raman spectroscopy," *Optics Letters*, vol. 35, no. 4, pp. 466–468, 2010.
- [185] J. B. Jensen, L. H. Pedersen, P. E. Hoiby et al., "Photonic crystal fiber based evanescent-wave sensor for detection of biomolecules in aqueous solutions," *Optics Letters*, vol. 29, no. 17, pp. 1974–1976, 2004.
- [186] L. Rindorf, P. E. Høiby, J. B. Jensen, L. H. Pedersen, O. Bang, and O. Geschke, "Towards biochips using microstructured optical fiber sensors," *Analytical and Bioanalytical Chemistry*, vol. 385, no. 8, pp. 1370–1375, 2006.
- [187] N. Burani and J. Lægsgaard, "Perturbative modeling of bragg-grating-based biosensors in photonic-crystal fibers," *Journal of the Optical Society of America B*, vol. 22, no. 11, pp. 2487–2493, 2005.
- [188] L. Rindorf, J. B. Jensen, M. Dufva, L. H. Pedersen, P. E. Høiby, and O. Bang, "Photonic crystal fiber long-period gratings for biochemical sensing," *Optics Express*, vol. 14, no. 18, pp. 8224–8231, 2006.
- [189] E. Coscelli, M. Sozzi, F. Poli et al., "Toward a highly specific dna biosensor: PNA-modified suspended-core photonic crystal fibers," *IEEE Journal on Selected Topics in Quantum Electronics*, vol. 16, no. 4, pp. 967–972, 2010.
- [190] Y. Ruan, E. P. Schartner, H. Ebendorff-Heidepriem, P. Hoffmann, and T. M. Monro, "Detection of quantum-dot labeled proteins using soft glass microstructured optical fibers," *Optics Express*, vol. 15, no. 26, pp. 17819–17826, 2007.
- [191] Y. Ruan, T. C. Foo, S. Warren-Smith et al., "Antibody immobilization within glass microstructured fibers: a route to sensitive and selective biosensors," *Optics Express*, vol. 16, no. 22, pp. 18514–18523, 2008.
- [192] S. O. Konorov, A. B. Fedotov, A. M. Zheltikov, and R. B. Miles, "Phase-matched four-wave mixing and sensing of water molecules by coherent anti-stokes Raman scattering in large-core-area hollow photonic-crystal fibers," *Journal of the Optical Society of America B*, vol. 22, no. 9, pp. 2049–2053, 2005.
- [193] S. O. Konorov, A. B. Fedotov, L. A. Mel'nikov, A. V. Shcherbakov, R. B. Miles, and A. M. Zheltikov, "Coherent Raman protocol of biosensing with a hollow photonic-crystal fiber," *Journal of X-ray Science and Technology*, vol. 13, no. 4, pp. 163–169, 2005.
- [194] J. Irizar, J. Dinglasan, J. B. Goh et al., "Raman spectroscopy of nanoparticles using hollow-core photonic crystal fibers," *IEEE Journal on Selected Topics in Quantum Electronics*, vol. 14, no. 4, pp. 1214–1222, 2008.
- [195] Y. Han, M. K. K. Oo, Y. N. Zhu et al., "Index-guiding liquid-core photonic crystal fiber for solution measurement using normal and surface-enhanced Raman scattering," *Optical Engineering*, vol. 47, no. 4, Article ID 040502, 2008.
- [196] Z. Xie, Y. Lu, H. Wei, J. Yan, P. Wang, and H. Ming, "Broad spectral photonic crystal fiber surface enhanced Raman scattering probe," *Applied Physics B*, vol. 95, no. 4, pp. 751–755, 2009.
- [197] C. M. B. Cordeiro, M. A. R. Franco, G. Chesini et al., "Microstructured-core optical fibre for evanescent sensing applications," *Optics Express*, vol. 14, no. 26, pp. 13056–13066, 2006.
- [198] A. M. Cubillas, M. Schmidt, M. Scharrer et al., "Ultra-low concentration monitoring of catalytic reactions in photonic crystal fiber," *Chemistry*, vol. 18, no. 6, pp. 1586–1590, 2012.
- [199] T. G. Euser, J. S. Y. Chen, M. Scharrer, P. S. J. Russell, N. J. Farrer, and P. J. Sadler, "Quantitative broadband chemical sensing in air-suspended solid-core fibers," *Journal of Applied Physics*, vol. 103, no. 10, Article ID 103108, 2008.
- [200] X. Yu, Y. Sun, G. B. Ren, P. Shum, N. Q. Ngo, and Y. C. Kwok, "Evanescent field absorption sensor using a pure-silica defected-core photonic crystal fiber," *IEEE Photonics Technology Letters*, vol. 20, no. 5, pp. 336–338, 2008.
- [201] C. Wu, B. O. Guan, C. Lu, and H. Y. Tam, "Salinity sensor based on polyimide-coated photonic crystal fiber," *Optics Express*, vol. 19, no. 21, pp. 20003–20008, 2011.

- [202] J. Mathew, Y. Semenova, G. Rajan, and G. Farrell, "Humidity sensor based on photonic crystal fibre interferometer," *Electronics Letters*, vol. 46, no. 19, pp. 1341–1343, 2010.
- [203] X. H. Yang and L. L. Wang, "Fluorescence ph probe based on microstructured polymer optical fiber," *Optics Express*, vol. 15, no. 25, pp. 16478–16483, 2007.
- [204] M. D. Levenson, "Detection of adsorbates on interior surfaces of holey fibers," United States Patent, 2005.
- [205] H. Du and S. A. Sukhishvili, "Functionalization of air hole array of phonic crystal fibers," WIPO and United States Patent, 2006.
- [206] Z. Li, M. Tan, S.-Y. Wang, W. Wu, and J. Tang, "Optical sensor and method employing half-core hollow optical waveguide," Unites States Patent, 2010.
- [207] A. Khetani, M. Naji, N. Lagali, H. Anis, and R. Munger, "Method for using a photonic crystal fiber as a Raman biosensor," United States Patent, 2010.
- [208] C. Gu, Y. Zhang, C. Shi, J. Z. Zhang, and L. Seballos, "Liquid core photonic crystal fiber biosensors using surface enhanced Raman scattering and methods for their use," United States Patent, 2011.
- [209] D. U. K. S. Amma, C. Y. Fu, M. Olivo, and K. S. J. Soh, "A photonic crystal fiber sensor," WIPO Patent, 2011.
- [210] G. A. S. Sanders, "Photonic crystal fiber sensor," United States Patent, 2010, (Scottsdale, AZ, US).
- [211] G. A. Sanders, R. W. Johnson, and S. Yates, "Photonic crystal fiber sensor," Japan, United States and European Patent, 2011.
- [212] X. Li, "Photon crystal optical fibre refractivity temperature sensor and measuring systems," China Patent, 2008.
- [213] X. Li, "Photon crystal optical fibre fluorescent temperature sensor and measuring systems," China Patent, 2008.
- [214] C. Zhao, S. He, X. Dong, and K. Ni, "High-sensitivity temperature sensor based on partial perfusion type HiBi-PCF-FLM (high birefringent photonic crystal fiber loop mirror)," China Patent, 2011.
- [215] C. Zhao, Y. Wang, Y. Jin, J. Kang, X. Dong, and S. Jin, "High-birefringence fiber loop mirror (HiBi-FLM) temperature sensor based on photonic crystal fiber-long period grating (PCF-LPG) differential modulation," China Patent, 2011.
- [216] C. Zhao, T. Li, X. Dong, W. Qian, and Y. Jin, "Humidity sensor based on tapered and perfused photonic crystal fibers," China Patent, 2011.
- [217] C. Zhao, T. Li, X. Dong, W. Qian, and Y. Jin, "Humidity sensor and device based on tapered and injection photonic crystal fiber," China Patent, 2011.
- [218] L. An, X. Zhao, and Z. Zheng, "Photonic crystal fiber sensor based on polarization interference," China Patent, 2011.
- [219] Z. Weigang, K. Guiyun, J. Long et al., "Photonic crystal fiber fluid sensing device," China Patent, 2005.
- [220] T. Wang, W. Ke, and J. Zhao, "Photonic crystal fiber optic liquid level sensor and sensing system formed by same," China Patent, 2011.
- [221] C. Zhao, Y. Wang, W. Qian, Y. Qiu, and S. Jin, "HiBi-PCF-FLM (fiber loop mirrors made of highly birefringent photonic crystal fiber) stress sensor based on strength detection differential demodulation and device," China Patent, 2011.
- [222] Y. Li, Y. Li, H. Long, and P. Lu, "Current sensor based on photonic crystal fiber grating," China Patent, 2010.
- [223] Z. T. Rao, "Hollow photon crystal optical fiber based Fabry-Perot interferometer sensor and its production method," China Patent, 2007.
- [224] J. Chen, R. Du, J. Hou et al., "Multi-parameter sensor and measurement system based on photonic crystal fiber," China Patent, 2010.
- [225] R. L. Willing, W. P. Kelleher, and S. P. Smith, "Photonic crystal interferometric fiber optical gyroscope system," United States Patent, 2004.
- [226] M. J. F. Digonnet, H. K. Kim, S. Blin, V. Dangui, and G. S. Kino, "Optical Sensor utilizing hollow-core photonic band-gap fiber with low phase thermal constant," United States Patent, 2008.

Research Article

Plastic Optical Fibre Sensing of Fuel Leakage in Soil

Masayuki Morisawa and Shinzo Muto

Department of Information and Communication System, Graduate School of Medicine and Engineering, University of Yamanashi, 4-3-11 Takeda, Kofu 400-8511, Japan

Correspondence should be addressed to Masayuki Morisawa, morisawa@yamanashi.ac.jp

Received 1 December 2011; Accepted 13 February 2012

Academic Editor: Kevin Chen

Copyright © 2012 M. Morisawa and S. Muto. This is an open access article distributed under the Creative Commons Attribution License, which permits unrestricted use, distribution, and reproduction in any medium, provided the original work is properly cited.

A basic operation of the very simple optical sensing system of fuel leakage in uniform sandy and clayey soils, which is consisting of a plastic optical fibre (POF) transmission line, the POF-type sensor heads, and a single LED photodiode pair, has been studied theoretically and experimentally. Its sensing principle is based on the POF structure change in the sensor head caused by fuels such as petrol. A scale-downed model prepared in the experimental room showed a possibility of optical detection of fuel leakage points in uniform soil. As this system operates without receiving the influence of water containing in fuels and soils, its application to fuel leak monitor around a filling station and oil tank can be expected.

1. Introduction

At present, various fuels such as petrol, kerosene, and light oil are used in many fields to make our life comfortable. However, leakage of fuels produces many serious problems such as pollution in soil or underwater, explosion, and combustion in a filling station or oil tank. To prevent such serious problems, quick and safety detection of fuel leakage point is strongly required. Of course, it goes without saying that an optical sensing is the safest method [1, 2], and, hitherto, several optical sensing systems such as an optical time domain reflectometry (OTDR) and a multipoint sensor system have been studied [3, 4]. However, considering the practical application around a filling station and oil tank, more simple and low-cost ones are desired. From this background, we made an attempt to develop a very simple and low-cost optical sensing system to detect leakage of fuel in soil. Therefore, we mainly used the POF because it has many advantages such as low cost, easiness in handling, and immunity to electromagnetic interference [5]. Its system consists of the POF transmission line, several POF-type sensor heads, and a single LED photodiode pair. According to the preliminary study, certain kinds of polymer such as polyisoprene (PIP) cause swelling by attachment of fuel molecules and then change its refractive index remarkably

[6]. Based on this phenomenon, the POF-type sensor head to detect petrol was fabricated and tested. Specially, a scale-downed model of the sensing system for detecting fuel leakage in uniform sandy and clayey soils has been studied theoretically and experimentally. This paper reports on its basic property towards development of the practical system.

2. Application Model and Its Operation Principle

The model considered here is shown schematically in Figure 1. As can be seen from this figure, the proposed optical sensing system consists of the POF transmission line, several POF-type sensor heads, and a single LED photodiode pair. In addition, its system assumes that the POF is buried underground but is not subjected to such a large pressure that would deform it considerably by breaking and crushing it to the extent that its original shape and state cannot be restored. This model seems to be suitable for the practical case around a filling station or oil tank. The sensing principle in the POF-type sensor head is based on the swell phenomenon in its cladding layer. When is exposed to vapour phase alkane or petrol, the refractive index of the PIP film with a thickness of about $5\ \mu\text{m}$ decreases from 1.52 to 1.48 as shown in Figure 2. The solid line in Figure 2 shows

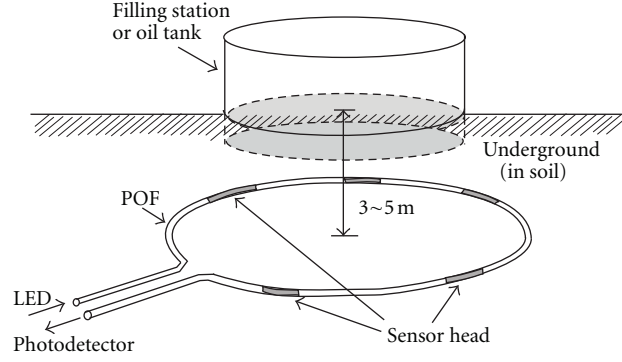


FIGURE 1: Application model of the POF-type sensing system.

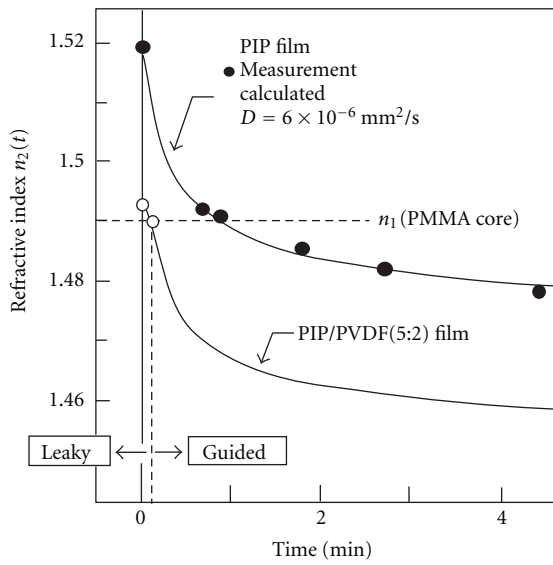


FIGURE 2: Refractive index changes in PIP and PIP/PVDF (5:2) films after exposing to hexane vapour.

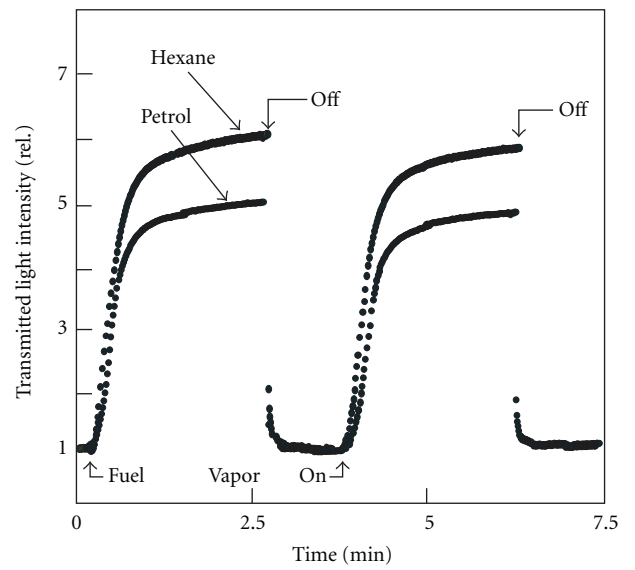


FIGURE 3: Response of POF-type sensor head with the PIP/PVDF (5:2) cladding layer to hexane and petrol vapours.

the theoretical change in the refractive index $n(t)$, which is calculated using a following one-dimensional diffusion equation for hexane concentration $N(t)$ in the PIP film with a diffusion coefficient of $D = 6 \times 10^{-6}$ mm/s and a relation between $N(t)$ and $n(t)$ [7, 8]:

$$\frac{\partial N(x, t)}{\partial t} = D \frac{\partial^2 N(x, t)}{\partial x^2}. \quad (1)$$

Assuming the initial condition of $N(x, 0) = 0$ and $N(0, t) = N_0$, the solution of above one dimensional diffusion equation is easily obtained as follows:

$$N(x, t) = N_0 \left(1 - \frac{2}{\sqrt{\pi}} \int_0^{x/(2\sqrt{Dt})} e^{-\alpha^2} d\alpha \right). \quad (2)$$

And then, as the density in the swelling film decreases with increasing $N(x, t)$, $n(x, t)$ can be expressed by the following equation:

$$n(x, t) = \frac{n_0 n_\infty(N_0)}{(n_0 - n_\infty(N_0))N(x, t)/N_0 + n_\infty(N_0)}, \quad (3)$$

where n_0 is the refractive index at $N(x, 0)$ and $n(N_0)$ is the final one at $N(x, \infty) = N_0$.

Considering the POF structure change in the sensor head consisting of the swell polymer clad and polymethylmethacrylate (PMMA) core with a refractive index of $n_1 = 1.490$, the initial refractive index (n_2) in the cladding layer must be set at a slightly larger value than n_1 in the fibre core [8]. Therefore, the mixture of the PIP and polyvinylidene fluoride (PVDF) with a ratio of 5 to 2 was considered as a sensitive cladding layer. The bare PMMA core was obtained by removing the cladding layer from the commercialized POF without a jacket (Mitsubishi-Rayon, ESKA), by mean of organic solvent such as 1,4-dioxane. About 15 minutes immersion at 20°C and wiping off the dissolved cladding polymer using a soft tissue made us easily obtain the bare PMMA core with a smooth surface. The PIP/PVDF (5:2) cladding polymer was dissolved in dimethylsulfoxide (DMSO) and was dip-coated on the bare PMMA core with a diameter of about 1 mm. Its thickness is about 5 μm. According to these conditions, the repeatability of the sensor

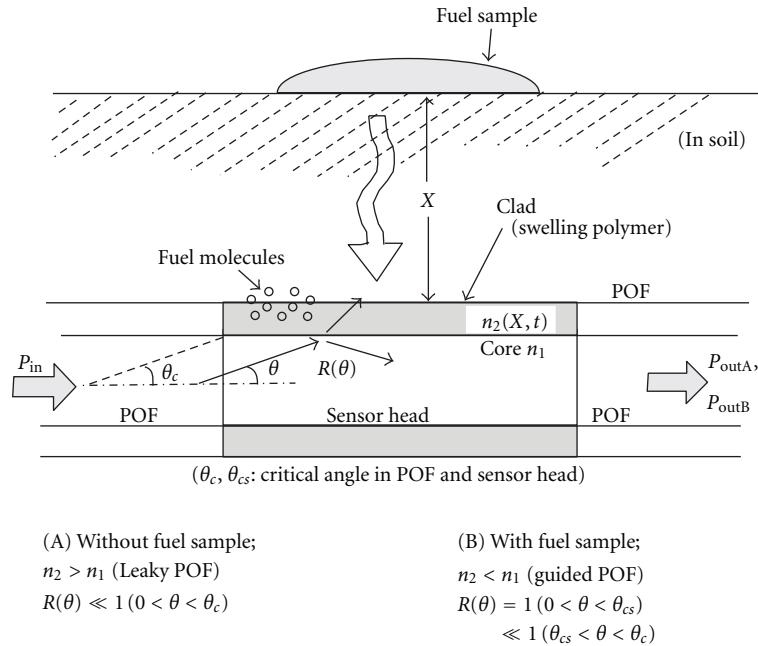


FIGURE 4: POF sensing model to detect fuel leakage in uniform soil. P_{outA} is the output light intensity, and P_{outB} is that one with fuel sample.

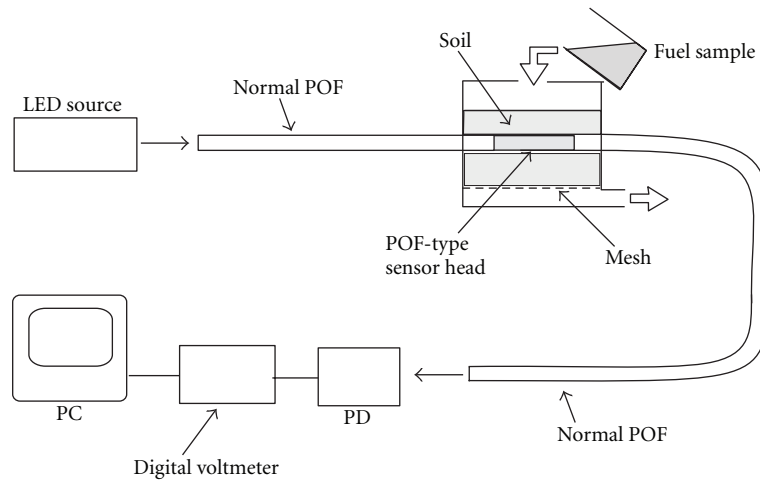


FIGURE 5: Experimental setup.

fabrication becomes very high. When was exposed to hexane vapour, its refractive index in cladding layer changed from 1.492 to 1.455, as also shown in Figure 2. From this result, it is clear that the POF-type sensor head changes quickly its structure from a leaky type to a guided one.

First, the sensor head with a length of 50 mm was tested to confirm its operation even in the wavelength region with a large propagation loss. So a blue LED was used as a light source. Figure 3 shows the results for vapour phase hexane and petrol. As can be seen from this figure, a large change in transmitted light intensity based on the POF structure change from leaky type to guided one was observed experimentally. In addition, the proposed sensor structure gave high sensitivity and good reproducibility for

both petrol and hexane. Referring to these results, the sensor head with a length of 10 mm was connected to the normal POFs at the input and output edges and was set at the position $x = 55$ mm in uniform sandy soil or clayey soil as shown in Figure 4. Here, the light reflection at the clad-soil boundary was neglected to simplify the analysis. In this figure, for the case of (a) without fuel sample, the output light intensity P_{outA} is small because the power reflection coefficient $R(\theta)$ at the core-clad boundary becomes a very small value [8]. On the other hand, for the case of (b) with fuel sample, the output light intensity P_{outB} increases remarkably because of its change to the guided structure. Then, the value of P_{outB}/P_{outA} gives the change in transmitted light intensity, that is, the sensitivity. Its property

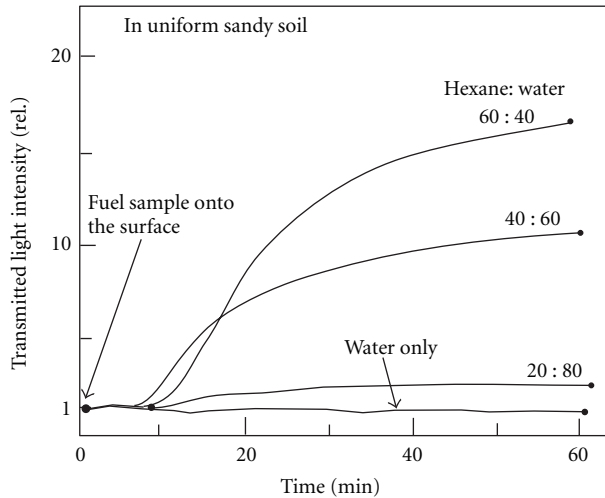


FIGURE 6: Sensor response observed in uniform sandy soil.

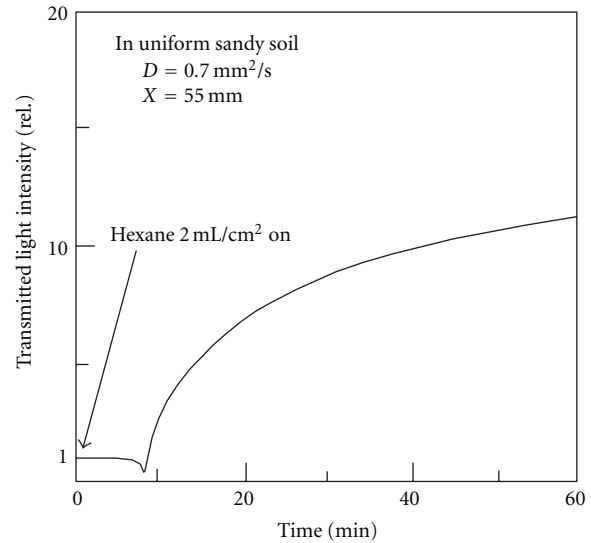


FIGURE 8: Calculated sensor response in uniform sandy soil.

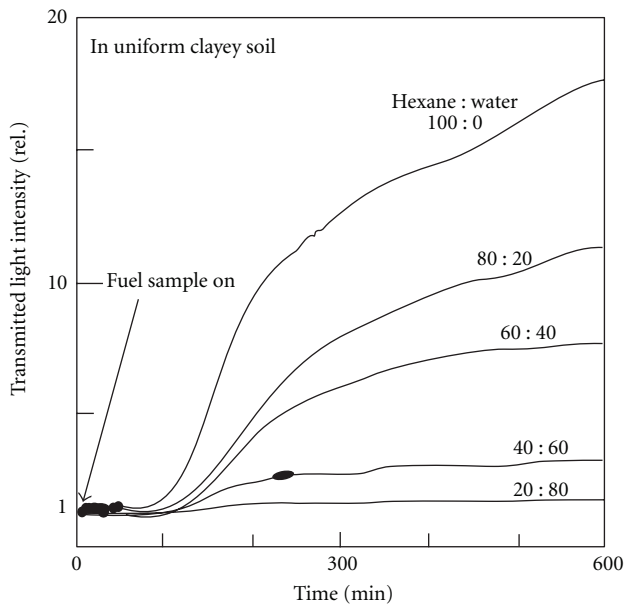


FIGURE 7: Sensor response observed in uniform clayey soil.

was measured using a photodetector, and its electrical signal was fed to a digital voltmeter connected to a computer for real-time data processing, as shown in Figure 5. In this experiment, to check an influence of water, the mixture of hexane and water was used as the fuel sample [7]. The obtained sensor responses are shown in Figures 6 and 7, respectively. From these figures, it is clear that the change in transmitted light intensity increases depending on the fuel concentration without receiving the influence of water and that diffusion of the fuel sample in clayey soil takes a much longer time. Furthermore, the diffusion coefficient of fuel sample in uniform soil was estimated from the start time of increase in the transmitted light intensity. For example, its value in uniform sandy soil used here was decided to be $0.7 \text{ mm}^2/\text{s}$. Using this value and a ray tracing method

[8], the change in transmitted light intensity through the sensor head can also be calculated theoretically. Its result is shown in Figure 8. As is clear from the figure, excepting the small dip at the critical point caused by the neglect of light reflection at the clad-soil boundary, the calculated sensor response coincided qualitatively with the experimental ones shown in Figure 6. In addition, as the similar operation was confirmed in the case with a long sensor head of 120 mm, a series connection of several sensor heads with a total length below 120 mm seems to be possible.

3. Detection Method of Fuel Leakage Point

Considering a practical application of the above sensor, detection of the leakage point is needed. Therefore, the POF sensing system with multisensor heads was considered. Its system is shown schematically in Figure 9, in which, the upper configuration is type (a) with equal sensor head lengths of 10 mm and the lower one is type (b) with different sensor head lengths of 30 mm, 20 mm, and 10 mm, respectively. This model also means a scale-downed sensor model of the fuel leakage point around a filling station or oil tank shown in Figure 1. However, to shorten the experiment time, these sensor heads were buried in uniform light sandy soil with a diffusion coefficient of $D_1 = 80 \text{ mm}^2/\text{s}$ and at 120 mm in depth. The value of D_1 was estimated experimentally using the same method described in Section 2. Furthermore, considering the directional diffusion of petrol in uniform light sandy soil, these values of D_2 and D_3 were also estimated from the value of D_1 to be $30 \text{ mm}^2/\text{s}$ and $10 \text{ mm}^2/\text{s}$, respectively. Under these conditions, a certain amount of petrol was poured onto the surface points marked with the closed circles of A, B, and C, respectively. To simplify the analysis, we assumed that fuel leakages from each point do not occur at the same time. Then, we can consider the above system as a cascade connection of three sensor heads. The calculated transmitted light intensity changes for each

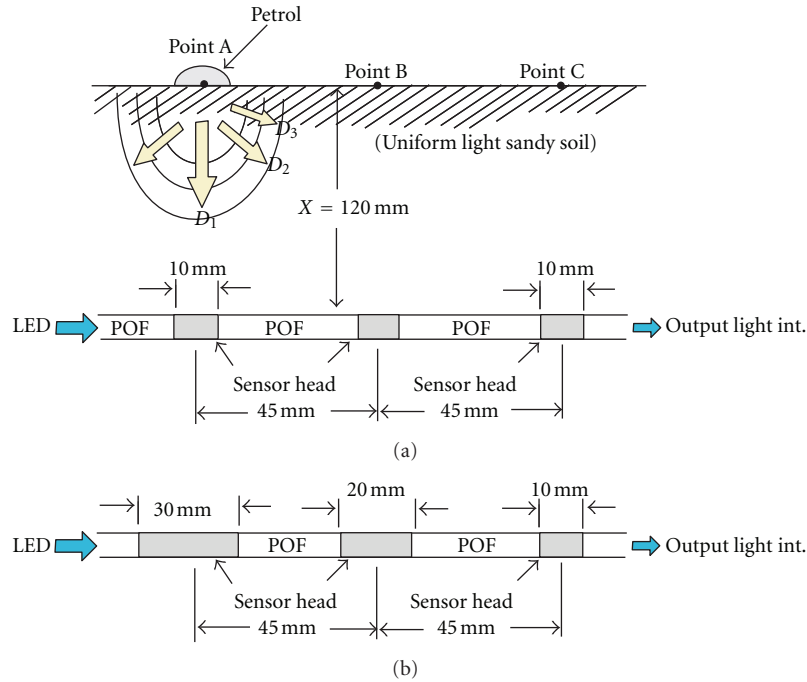


FIGURE 9: Three sensor heads system to detect petrol leakage point in uniform light sandy soil. (a) With equal sensor head lengths of 10 mm and (b) with sensor head lengths of 30 mm, 20 mm, and 10 mm.

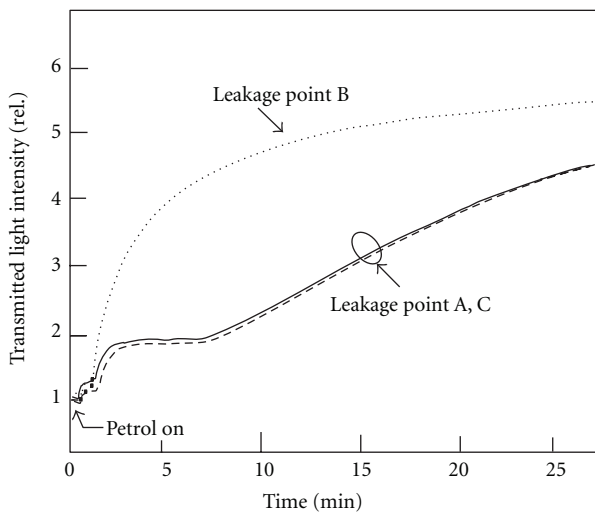


FIGURE 10: Calculated output light intensity change in type (a) for each leakage point.

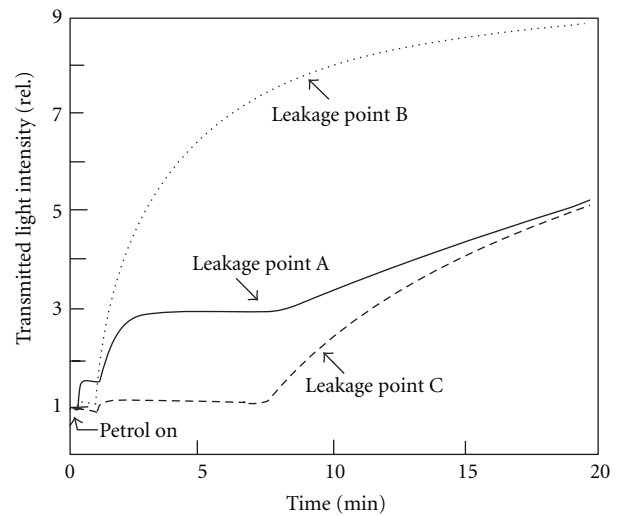


FIGURE 11: Calculated output light intensity change in type (b) for each leakage point.

leakage point A, B, and C are shown in Figures 10 and 11, respectively. From these figures, it is found that the change in light intensity for the leakage point A or C becomes small in the early stage but that one for the fuel leakage point B increases remarkably. The later property is due to that, a few minute after the petrol reaching to the second sensor head, the first and the third sensor heads operate as a guided POF at almost same time. In addition, the difference of the sensor head length between the first sensor head and third one made clear the change in the light intensity level in the early stage.

Judging from these results, the system of type (b) showed a useful property to detect fuel leakage point.

To confirm the above characteristics experimentally, the same configuration of the three sensor heads and measurement setup were used. In this experiment, the transmitted light intensity changes in only early stage were measured because the continuous supply of petrol was difficult. The results obtained are shown in Figures 12 and 13, respectively. As is clear from these figures, the experimental properties in

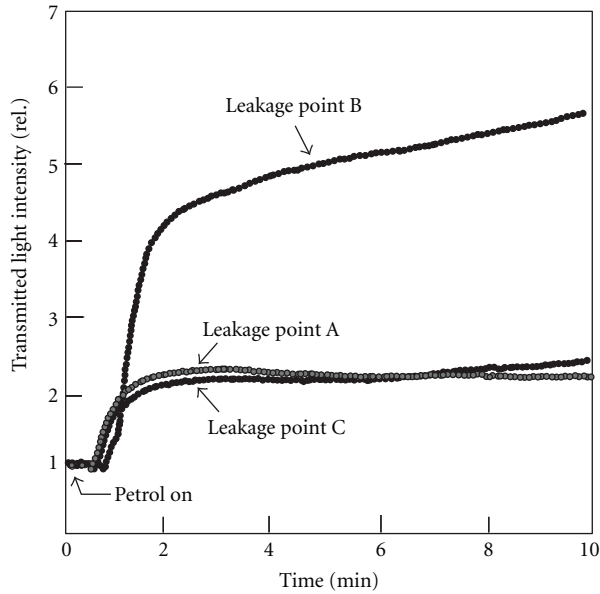


FIGURE 12: Observed light intensity change in early stage for type (a).

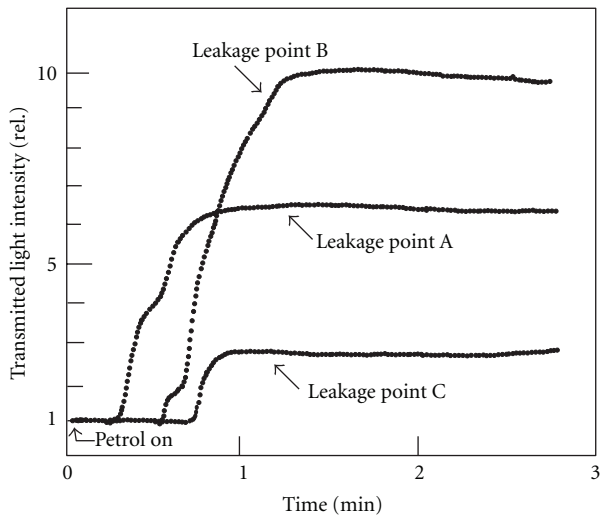


FIGURE 13: Observed light intensity change in early stage for type (b).

early stage of fuel leakage coincided qualitatively with the calculated ones. Thus, a very simple system consisting of the POF transmission line and the POF-type sensor head showed a possibility on optical detection of the fuel leakage point in uniform soil around a filling station and/or oil tank. In addition, this system will be used over whole visible region because it operated even in the blue wavelength. If the fuel leakages from some points occur simultaneously, a complicated change in the transmitted light intensity will be observed. Such a response also gives an important information showing the simultaneous fuel leakage from some points. Furthermore, when considering the practical uses of this sensor, it should be noted that this sensor

system depends significantly on the diffusion coefficient of soil into gasoline. Therefore, for practical uses of this sensor, calibration should be performed by collecting a soil sample from the site where this system is set up and measuring the diffusion coefficient of the soil sample. However, when the diffusion coefficient is not uniform, the sensor response may become complicated. Therefore, we wish to treat them theoretically and experimentally in the near future.

4. Conclusions

The very simple POF-type optical sensing system of fuel leakage in uniform soils, which is based on the POF structure change in the sensor head produced by a swell phenomenon in the cladding layer, has been studied using a scale-downed model. Its theoretical and experimental results showed that a quick and safety detection of petrol leakage in uniform soil becomes possible without receiving an influence of water included in fuel and soil. Although this system is not suitable for the distributed leakage detection over a long distance, it seems to be used for a few point detection around a filling station and/or oil tank. Referring to these results, we are now studying the improved system which will be able to use for detecting fuel leakage from many points. Its result we will be reported in the near future.

References

- [1] J. Darkin and B. Calshaw, *Optical Fiber Sensors*, vol. 4, ch 17, Artech, Boston, Mass, USA, 1997.
- [2] M. Archenault, H. Gagnaire, J. P. Goure, and N. Jaffrezic-Renault, "A simple intrinsic optical-fibre chemical sensor," *Sensors and Actuators B*, vol. 8, no. 2, pp. 161–166, 1992.
- [3] K. I. Aoyama, K. Nakagawa, and T. Itoh, "Optical time domain reflectometry in a single-mode fiber," *IEEE Journal of Quantum Electronics*, vol. 17, no. 6, pp. 862–868, 1981.
- [4] P. A. Wallace, N. Elliott, M. Uttamlal, A. S. Holmes-Smith, and M. Campbell, "Development of a quasi-distributed optical fibre pH sensor," in *Proceedings of the 14th International Conference on Optical Fiber Sensors (OFS '00)*, pp. 456–459, October 2000.
- [5] A. Weinert, *Plastic Optical Fibers*, ch 2, Publics MCD, Munich, Germany, 1999.
- [6] S. Muto, K. Uchiyama, G. Vishnoi et al., "Plastic optical fiber sensors for detecting leakage of alkane gases and gasoline vapors," in *Photopolymer Device Physics, Chemistry, and Applications IV*, vol. 3417 of *Proceedings of SPIE*, pp. 61–69, July 1998.
- [7] D. Matsuyama, M. Morisawa, C. X. Liang, and S. Muto, "Plastic Optical Fiber Sensing of Leakage of Fuel in Soil," in *Technical Digest of 16th International Conference on Optical Fiber Sensors (OFS-16)*, Proceedings of SPIE, p. 618, 2003.
- [8] M. Morisawa, Y. Amemiya, H. Kohzu, C. X. Liang, and S. Muto, "Plastic optical fibre sensor for detecting vapour phase alcohol," *Measurement Science and Technology*, vol. 12, no. 7, pp. 877–881, 2001.

Research Article

Plastic Optical Fiber Sensing of Alcohol Concentration in Liquors

Masayuki Morisawa and Shinzo Muto

Graduate School of Medicine and Engineering, University of Yamanashi 4-3-11 Takeda, Kofu, 400-8511, Japan

Correspondence should be addressed to Masayuki Morisawa, morisawa@yamanashi.ac.jp

Received 1 December 2011; Revised 30 January 2012; Accepted 2 February 2012

Academic Editor: Wolfgang Ecke

Copyright © 2012 M. Morisawa and S. Muto. This is an open access article distributed under the Creative Commons Attribution License, which permits unrestricted use, distribution, and reproduction in any medium, provided the original work is properly cited.

A simple optical fiber sensing system of alcohol concentration in liquors has been studied. In this sensor head, a mixture polymer of novolac resin and polyvinylidene fluoride (PVDF) with a ratio of 9 : 1 was coated as a sensitive cladding layer on the plastic fiber core made of polystyrene-(PS-)coated polycarbonate (PC). Using this sensor head and a green LED light source, it was confirmed that alcohol concentration in several kinds of liquors from beer to whisky can easily be measured with a fast response time less than 1 minute.

1. Introduction

In every-day life, brewers supply several liquors (alcoholic drinks) such as beer, brandy, wine, and whisky, and people are fond of them. However, in brewery, it takes many times to check the alcohol concentration in product liquors, for example, using a distillation method [1] and gas or liquid chromatography [2]. Therefore, development of a simple and quick detection system of alcohol concentration in liquors is strongly required.

From the above view point, we have studied an optical measurement system of alcohol concentration in liquors using a plastic optical fiber (POF) because the POF has many advantages such as low cost, easiness in handling, and immunity from electrical interface [3–6]. This paper reports on its configuration and basic sensing properties of alcohol concentration in some alcoholic drinks.

2. Sensor Head Structure and Its Sensing Principle

A certain kind of polymers such as novolac swells when it is exposed to vapor-phase alcohol [7] or alcohol solutions. This effect produces a change in refractive index of that film. Figure 1 shows a change in the refractive index of novolac resin when exposed to ethanol, determined using an Abbe

refractometer. As can be seen from this figure, after being exposed to the ethanol (EtOH), the refractive index in the novolac film decreased remarkably from $n_D = 1.61$ to 1.46. In opposition, when is ethanol exhausted from the film, its refractive index returned to the initial value. This reversible property is more suitable to construct an optical sensor.

Using this property in the novolac film, we fabricated the POF-type sensor head. Figure 2 shows schematics of the sensor head structure and operation models with and without alcohol, respectively. In this POF sensor, the marketed polycarbonate (PC) fiber with a refractive index of $n_D = 1.58$ was used after removing the cladding layer. The polystyrene (PS) layer with a refractive index of $n_D = 1.60$ was coated on the PC fiber surface because the PC surface was broken by the solvent for novolac solution. Referring to the preliminary experiment [7], the novolac/iron complex (novolac/Fe : SO) was found to be superior to novolac resin only. Therefore, we used it as an alcohol sensitive material.

In Figure 2(a), the sensor head operates as a leaky POF (i.e., $n_1 < n_2$), and the intensity of output light passing through it is very weak. In this case, by using a ray tracing method, the calculated total output light intensity P_{out1} is given by

$$P_{out1} = \sum_{\theta=0}^{\theta_c} P(\theta)r(\theta)^m, \quad (1)$$

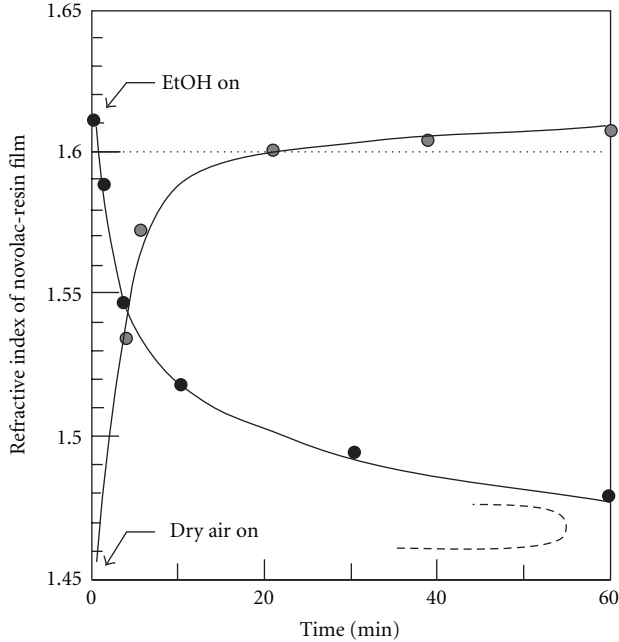


FIGURE 1: Refractive index change in novolac film with thickness of about $5 \mu\text{m}$.

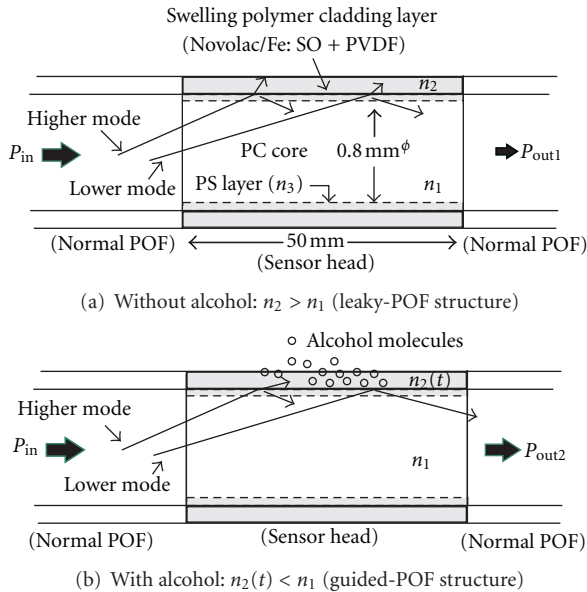


FIGURE 2: Sensor head structure.

where $P(\theta)$ is the optical power for a ray with an angle θ , θ_c is the critical angle at the input side of the POF, $r(\theta)$ is the power reflection coefficient, and m is the reflection number in the sensor head.

On the other hand, when exposed to alcohol, the cladding layer swells, and its refractive index begins to decrease, becoming lower than that of the fiber core (i.e., $n_1 > n_2$). Then, as shown in Figure 2 (b), the sensor head changes to a guided POF, and the output light intensity increases

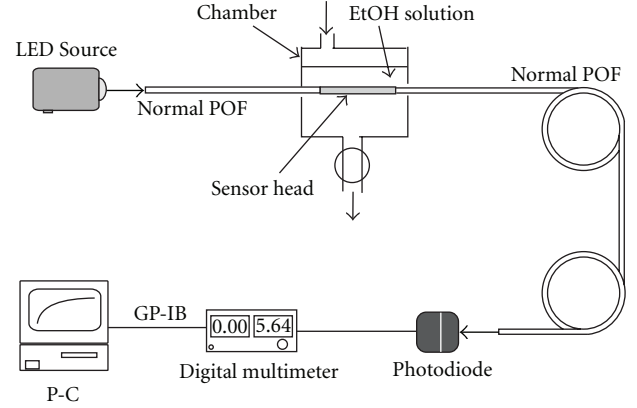


FIGURE 3: Experimental setup.

remarkably. In this case, the total output light intensity $P_{\text{out}2}$ of the sensor head is given by

$$P_{\text{out}2} = \sum_{\theta=0}^{\theta_{cs}} P(\theta) + \sum_{\theta=\theta_{cs}}^{\theta_c} P(\theta)r^m, \quad (2)$$

where θ_{cs} is the critical angle of the sensor head. The value of $P_{\text{out}2}/P_{\text{out}1}$ describes the relative change in the output light intensity depending on the alcohol.

As is evident from (1) and (2), for enabling this sensor to respond to alcohol at a low concentration, the difference between the initial refractive index of the cladding and that of core is required to be decreased so that switching from the leaky to the waveguide modes becomes easy. Hence, we have mixed low-refractive-index polyvinylidene fluoride (PVDF; $n_D = 1.42$) with novolac resin so that the refractive index of the cladding polymer approaches that of the PC (polycarbonate) core. The mixed film of novolac/Fe:SO and PVDF with a ratio of 3 to 1 was coated on the above PS-coated-PC fiber (PS/PC) with a core diameter of 0.8 mm, by means of a dip coating.

Next, we consider the effect of the intermediate protective PS layer. In terms of a ray-tracing technique based on the Snell's law

$$n_1 \sin \theta_1 = n_3 \sin \theta_3 = n_2 \sin \theta_2, \quad (3)$$

where n_3 is the refractive index of PS. If the refractive index of the PC core layer, n_1 , is smaller than that of the intermediate PS layer, n_3 (i.e., $n_1 < n_3$), the total reflection of light from the core at the cladding interface (on the core side) is determined from the refractive index of the PC core layer, n_1 , and that of the cladding layer, n_2 , regardless of the presence or absence of the intermediate PS layer. Therefore, the intermediate PS layer does not affect the total reflection.

3. Experimental Setup

Figure 3 shows the experimental setup. The POF-type sensor head was set in the small chamber and was connected to the normal POFs on its input and output side. A green LED

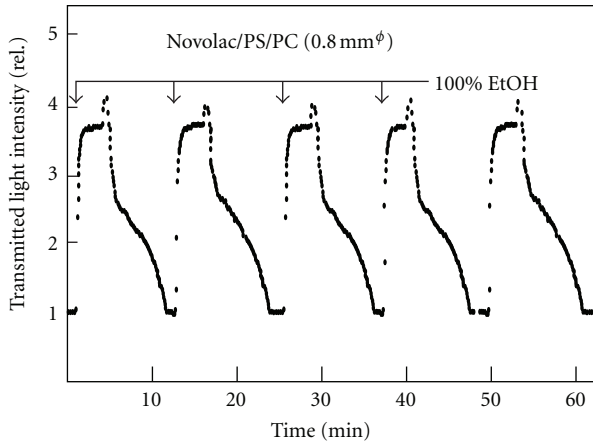


FIGURE 4: Sensor response to 100% ethanol solution.

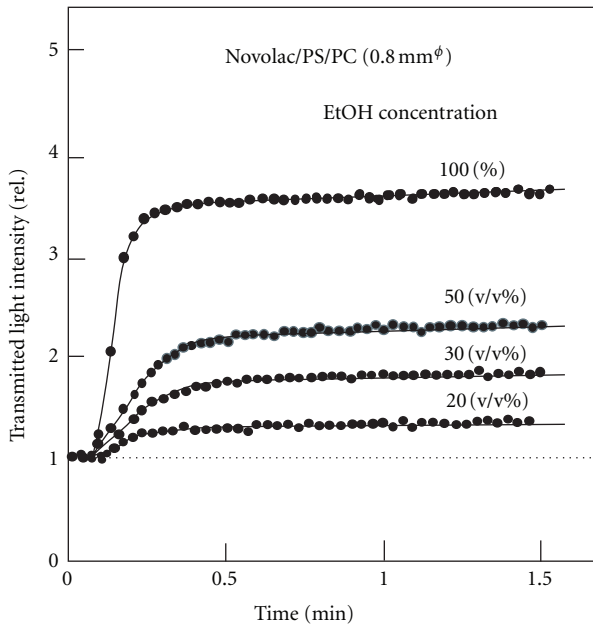


FIGURE 5: Output light intensity change for various concentrations of ethanol.

light with a wavelength of about 530 nm was guided through the input-side POF, and the transmitted light intensity was measured at the end of output-side POF using a photodiode. The output electrical signal was fed to a digital voltmeter and a computer for data processing. As sensing samples, ethanol solutions diluted by water and several kinds of marketed liquor were used.

4. Experimental Results

First, the sensor response for 100% ethanol was checked. Its result is shown in Figure 4. From this figure, it is found that the transmitted light intensity passing through the sensor head (output light intensity) increased remarkably as soon as ethanol was injected and then reached a stable value after about 1 min. In addition, this system showed

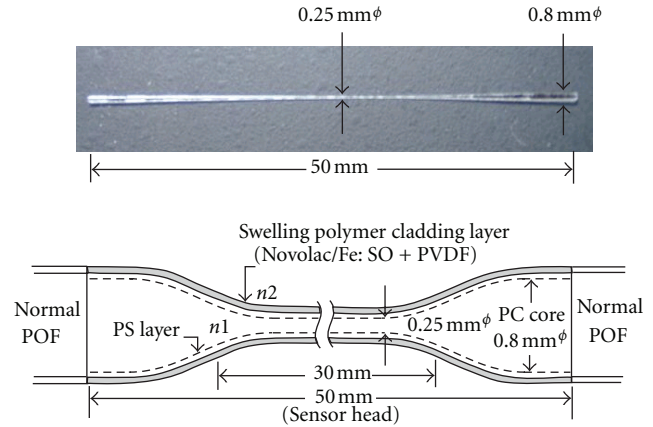


FIGURE 6: Photograph and illustrated structure of taper-type POF sensor head.

good reproducibility. On the other hand, when the ethanol solution was ejected, the spiky signal suddenly appeared and then the output intensity began to decrease slowly. These phenomena are due to residual alcohol droplets attached on the sensor head surface. In fact, after sending dry air to the sensor head by using a blower, the output intensity returned to the initial value. So, next, the change in output light intensity against various ethanol solutions was measured. The result is shown in Figure 5.

From this figure, it is found that the output light intensity increases with fast response time less than 0.5 min. Thus, the presented POF sensor operated as a quick and good ethanol-concentration sensor over the range of about 20 v/v% to 100 v/v%. However, it did not operate for the low-ethanol-concentration region below 10 v/v%. So, further improvement was needed to obtain higher sensitivity.

5. Fabrication of Taper-Type POF Sensor Head

As shown in Figure 2, lower modes in this POF-type sensor head mainly contribute to the sensitivity. Therefore, to improve sensitivity, it is better to use a sensor head with a small core diameter. So we tried to fabricate a taper-type POF sensor head by means of a solution etching. The PC fiber with a core diameter of 0.8 mm and a length of 50 mm was etched by immersing in 1,4-dioxane for about 1 hour at room temperature and then the PS layer and the novolac/Fe:SO + PVDF sensitive cladding layer were dip-coated on it in turn, as shown in the illustrated sensor head structure in Figure 6.

6. Measurement of Alcohol Concentration in Liquors

The change in output light intensity against a various ethanol concentration was measured using the new taper-type POF sensor head. Its result is shown in Figure 7. As is clear from this figure, it became possible to measure a low concentration of ethanol solution below 5 v/v%. In addition, if we compare these data with the results obtained using

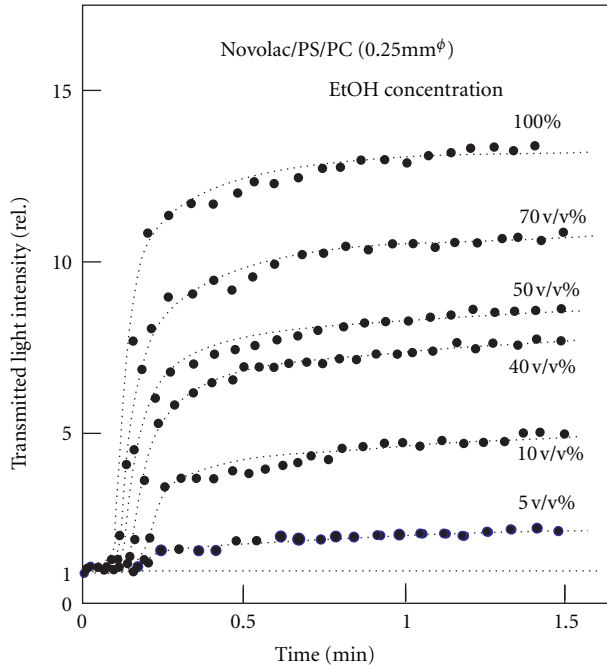


FIGURE 7: Response of the taper-type sensor head for various concentrations of ethanol.

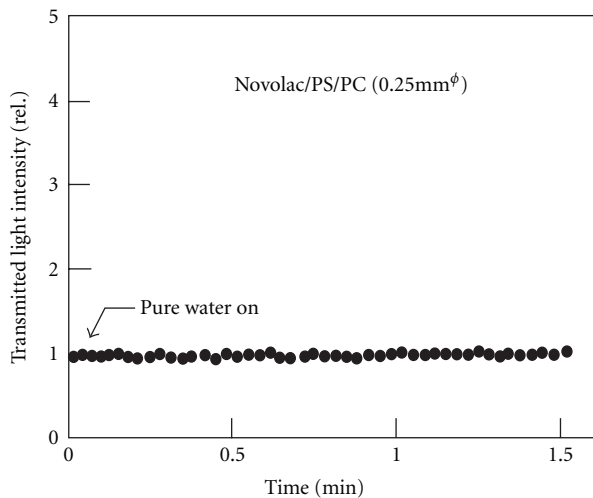


FIGURE 8: Sensor response to water only.

non tapered sensors as shown in Figure 5, we can observe that the change in the intensity of the transmitted light with the concentration of each component becomes so large that the sensitivity is improved by at least a factor of three. This result shows that this sensor can be used for detecting alcohol concentration of several real liquors.

In addition, the result in Figure 8 shows that this sensor does not receive any influence from water. The change in the light intensity with temperature is shown in Figure 9. The light intensity has a negligible dependence on temperature. These properties are also very suitable for a real application. Through these experiments, a calibration curve

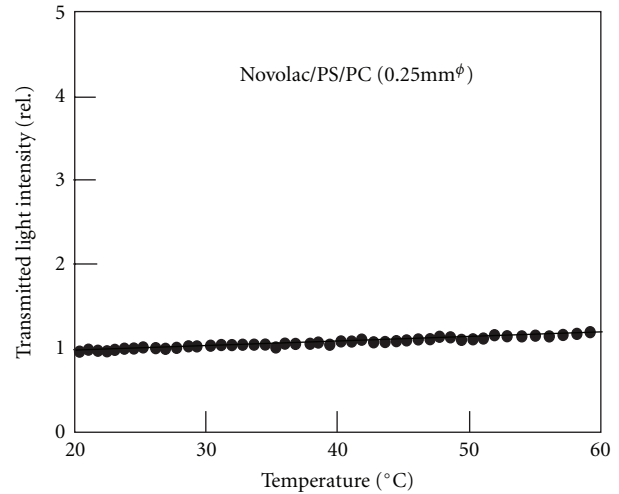


FIGURE 9: The temperature dependence of the POF sensor.

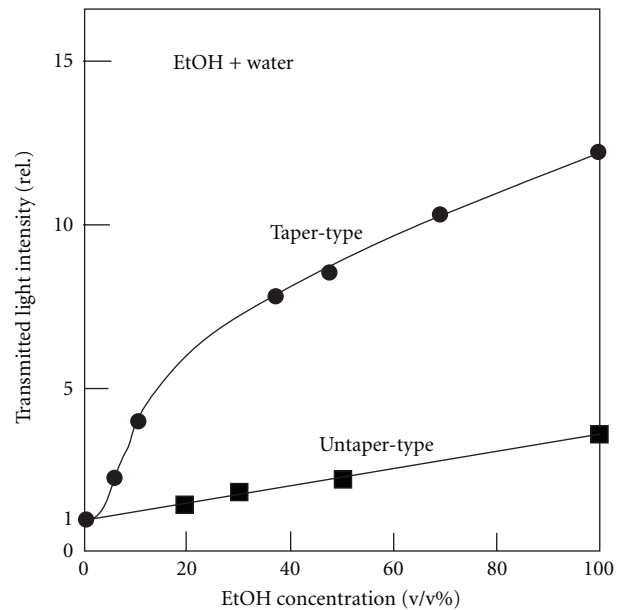


FIGURE 10: Calibration curve against ethanol concentration.

against ethanol concentration could be obtained as shown in Figure 10. In addition, the response does not depend on the concentrations of sugar and salt or acid and alkali, which are potentially contained in alcoholic beverages. This is because novolac resin in the cladding polymer does not exhibit swelling due to these components.

So, next, we tried to measure the alcohol concentration in real liquors such as beer, “Ume” brandy, red wine, white wine, and whisky, which were on the market. The result is shown in Figure 11. The data for white wine is not shown in Figure 11 because it almost overlapped the one of red wine. As can be seen from this figure, alcohol concentration in real liquors can be measured without receiving any influence of color substance and bubble in liquors.

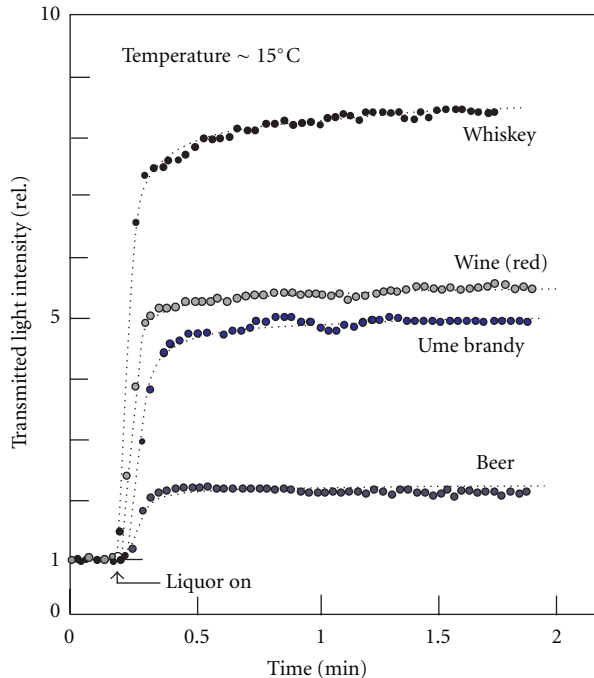


FIGURE 11: Transmitted light intensity change for several kinds of marketed liquor.

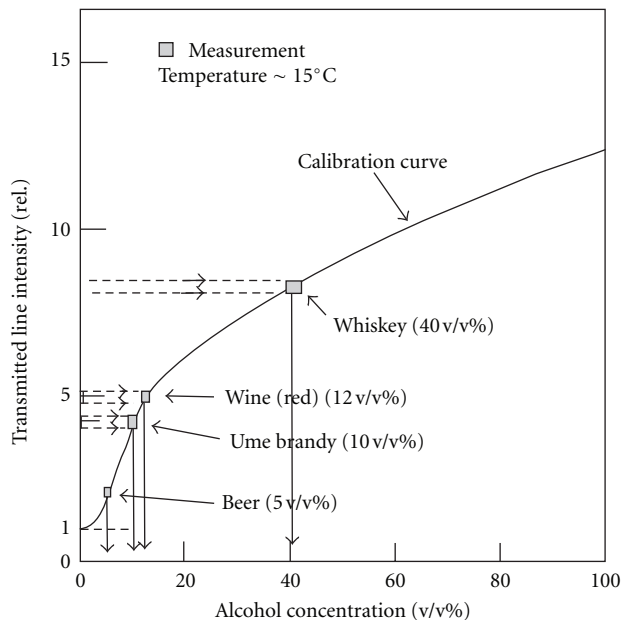


FIGURE 12: Measured alcohol concentration properties. The value of alcohol concentration on the label of liquor bottles are also shown in brackets.

Using the value of the output light intensity at about 1 minute after and the obtained calibration curve in Figure 10, the main result in this paper could easily be obtained as shown in Figure 12. This figure shows that the measured alcohol concentration fitted well to the one described on the label of real liquor bottle with an accuracy of ± 0.5 v/v%.

Namely, usefulness of the presented POF-type alcohol concentration sensor was demonstrated.

7. Conclusions

A novel and very simple POF-type sensor for detecting alcohol concentration in liquors, which is based on the POF structure change in sensor head from leaky-type to guided-one, has been studied experimentally. Using this sensor head with a small core diameter of about 0.25 mm, optical detection of the alcohol concentration in real liquors, for example, from beer (5 v/v%) to whiskey (40 v/v%) could easily be obtained with a fast response time less than 1 min. Therefore, this sensor will be available for use in any brewery. In addition, the sensitive cladding polymer used here also responds to methanol in vapor phase and solution. Therefore, the presented POF-type alcohol sensor may be used for monitoring leakage of methanol in methanol battery system. Such a study is underway in our laboratory and its result will be reported in the near future.

References

- [1] L. Nykanen and H. Suomalainen, *Aroma of Beer, Wine and Distilled Alcoholic Beverages*, Akademie, Berlin, Germany, 1983.
- [2] E. Peynaud, *Knowing and Making Wine*, John Wiley & Sons, New York, NY, USA, 1984.
- [3] A. Weinert, *Plastic Optical Fibers*, Publics MCD, Munich, Germany, 1999.
- [4] POF Consortium in Japan, Ed., *Plastic Optical Fiber*, Kyoritsu, Tokyo, Japan, 1997.
- [5] J. Dakin and B. Culshaw, *Optical Fiber Sensors*, vol. 4, Artech House, Boston, Mass, USA, 1997.
- [6] S. Muto, O. Suzuki, T. Amano, and M. Morisawa, "A plastic optical fibre sensor for real-time humidity monitoring," *Measurement Science and Technology*, vol. 14, no. 6, pp. 746–750, 2003.
- [7] M. Morisawa, Y. Amemiya, H. Kohzu, C. X. Liang, and S. Muto, "Plastic optical fibre sensor for detecting vapour phase alcohol," *Measurement Science and Technology*, vol. 12, no. 7, pp. 877–881, 2001.